9-23-2014 12:00 AM

# Digital Generation and Radiation in Spherical-Void-Phase Porous Media

Nolan J. Dyck
*The University of Western Ontario*

Supervisor
Dr. Anthony Straatman
*The University of Western Ontario*

Graduate Program in Mechanical and Materials Engineering
A thesis submitted in partial fulfillment of the requirements for the degree in Master of Engineering Science

# DIGITAL GENERATION AND RADIATION IN SPHERICAL-VOID-PHASE POROUS MEDIA

Integrated Article Thesis

by

Nolan James Dyck

Graduate Program in Mechanical and Materials Engineering

A thesis submitted in partial fulfillment
of the requirements for the degree of
Masters of Engineering Science

The School of Graduate and Postdoctoral Studies
The University of Western Ontario
London, Ontario, Canada

# Abstract

This thesis documents a novel method for method to generate digital samples of spherical void phase foams to predict effective hydraulic, thermal and radiative properties with the intention of assessing the viability of carbon foam as a volumetric solar receiver. The method employs discrete element modeling software to simulate the compression of spherical bubbles into a fully periodic, cubic domain. These domains were subsequently used to determine a variety of effective transport properties to be used in porous media design problems. The predicted properties agreed well with those obtained through experimental and other numerical methods, notably predicting more accurate hydraulic properties than those obtained using idealized, or unit-cell models. It is concluded that the digital generation technique is a cheap, fast, and effective method for obtaining bulk material properties. It is further concluded that the carbon foams studied will absorb almost all incident radiation for most design cases.



## Keywords

Porous Media, Digital Generation, Radiation, Carbon Foam, Volume Averaging, Property Characterization

# Co-Authorship Statement

All papers are drafted by Nolan Dyck and modified under the supervision of Prof. Anthony Straatman.

# Acknowledgments

I thank my parents for their continuous support and encouragement while conducting my research and writing this thesis.

I would also like to thank my supervisor, Dr. Anthony Straatman, for encouraging me to pursue my research interests, and for his patience when I have failed.

# Table of Contents

Abstract ..... ii

Co-Authorship Statement ..... iii

Acknowledgments ..... iv

Table of Contents ..... v

List of Tables ..... viii

List of Figures ..... ix

Chapter 1 ..... 1

1 General Introduction ..... 1

1.1 Literature Review ..... 2

1.1.1 Volumetric Solar Receivers ..... 2

1.1.2 Microstructure Modeling ..... 3

1.1.3 Modeling Thermal Radiation in Porous Media ..... 6

1.2 Governing Equations ..... 10

1.2.1 Conservation of Mass ..... 10

1.2.2 Conservation of Momentum ..... 10

1.2.3 Conservation of Energy ..... 11

1.2.4 Radiative Transfer Equation ..... 11

1.3 Volume Averaging the Governing Equations ..... 14

1.3.1 Volume Averaging Theorems ..... 17

1.3.2 Conservation of Mass ..... 18

1.3.3 Conservation of Momentum ..... 18

1.3.4 Conservation of Energy ..... 26

1.3.5 Radiative Transfer Equation ..... 32

1.4 Outline of Upcoming Chapters ..... 41

1.5 References ....41
Chapter 2....51
2 A New Approach to Digital Generation of Porous Media....51
2.1 Introduction....51
2.2 Formulation....54
2.3 Contact Law....56
2.4 Validation....60
2.4.1 Digital Sample Generation....60
2.4.2 Setup....63
2.4.3 Results....66
2.5 Property Identification....71
2.6 Summary....72
2.7 Acknowledgements....73
2.8 References....74
Chapter 3....78
3 Radiative Property Characterization of Spherical Void Phase Porous Media....78
3.1 Introduction....78
3.2 The Volume Averaged Radiative Transport Equation....79
3.3 Radiation Property Identification....81
3.3.1 Bouger's Law and the Cumulative Distribution Function....81
3.3.2 Implementation of the MC Ray-tracing Method....82
3.3.3 Sample Generation....83
3.3.4 REV Sizing....85
3.3.5 Property Identification....86
3.4 Conclusion....88
3.5 Acknowledgements....89

3.6 References .....89
Chapter 4.....92
4 Conclusions and Future Work.....92
4.1 Conclusions and Research Contributions.....92
4.2 Future Work.....93
4.3 References .....96

# List of Tables

Table 2.1 Descriptions of terms in Eq. (2.1) ..... 57

Table 2.2 Permeability and Forchheimer Coefficients ..... 69

Table 3.1 Summary of the polynomial coefficients applicable to Eq. (3.15) ..... 88

# List of Figures

Figure 1.1 A single pass volumetric solar collector ..... 2

Figure 1.2: Interface phenomena; rays emanating from the interface element $dA$ into direction $\hat{\mathbf{s}}$ may be reflected from phase $i$, and transmitted from phase $j$ ..... 13

Figure 2.1 Periodic interface implementation showing two original primitives, $A$ and $B$, as well as one wrapped primitive, $A'$. The distance between the two periodic faces is $\varepsilon$ ..... 56

Figure 2.2 Axis-symmetric opposing bubbles affixed to parallel surfaces. The overlapping region is called the interaction zone. ..... 57

Figure 2.3 An infinite linear chain of interacting spherical bubbles with alternating radii. ... 59

Figure 2.4 CAD isometric view of a REV of graphite foam sample ..... 62

Figure 2.5 Electron micrograph images of a graphite foam specimen (a) and (b) [21] in comparison to a CAD model of geometry generated using the current method (c) and (d)... 62

Figure 2.6 Average Force Ratio vs. Number of Primitives. ..... 63

Figure 2.7 ANSYS generated mesh showing (a) broad-view and (b) close-up ..... 65

Figure 2.8 Pressure Drop vs. Reynolds' Number. Markers are computed points; lines are Darcy-Forchheimer correlation ..... 67

Figure 2.9 Close-up of streamline plot inside the current geometry. The global flow direction is into the page. Warmer colors indicate higher velocity. ..... 68

Figure 2.10 Nusselt number vs. Reynold's number. Markers are computed points; lines are curve fits to Eq. (2.12) ..... 70

Figure 2.12 Pressure Drop vs. Reynolds number; markers are simulation data, lines are curve fits ..... 72

Figure 2.13 Interfacial Nusselt number vs. Reynolds number; markers are simulation data, lines are curve fits ..... 72

Figure 3.1 Intensity incident normally on an attenuating slab of thickness $dz$ ..... 81

Figure 3.2 Negative volume of a digitally generated carbon foam sample; $N_s = 300,\ d = 400\ \mu\text{m},\ \sigma_d = 120\ \mu\text{m},\ \varepsilon = 0.80$ ..... 84

Figure 3.3 Extinction Coefficient vs. Number of Primitives. $\beta^+$ is the non-dimensional extinction coefficient. ..... 86

Figure 3.4 Non-dimensional extinction coefficient vs. porosity ..... 87

# Chapter 1

## 1 General Introduction

Porous media are heterogeneous materials comprised of a solid microstructure (or matrix) and a fluid which fills the space unoccupied by the matrix. In heat transfer applications, an important property of porous materials is the connectivity of the void phase; an inter-connected pore structure will allow fluids to pass through the material. This characteristic allows engineers to leverage a key property of porous materials: the surface area-to-volume ratio. Consider a cooling application, wherein a thermally conductive solid matrix will carry heat from a hot boundary into the porous domain (e.g. DeGroot et. al [1]). From there, a cold fluid may be passed through the solid matrix to provide continuous cooling. This mechanism is the same as that employed in traditional heat sinks with active cooling, however the effective surface area in porous materials is often several orders of magnitude greater [2]. In convection applications heat transfer correlates positively with the exposed surface area, so porous materials can be expected to outperform traditional solutions in many heat transfer applications.

Considering their effectiveness in applications involving convection heat transfer, it is desirable to fully characterize the physical behaviour of porous materials so that they might be adequately designed in the presence of other phenomena. The motivation for this thesis was to explore one such phenomenon: radiation in porous materials. Specifically, it was of interest to evaluate the effectiveness of graphitic foam as a volumetric receiver for incident solar radiation for applications in solar collectors.

As an illustrative example, consider the solar collector in Figure 1.1, where a working fluid such as water or air can be forced through the porous medium. The medium volumetrically absorbs the portion of incident solar radiation $q''_{\text{solar}}$ which penetrates the upper glass covering. This heat is then conducted to the working fluid, and advected away. Inevitably some heat will be lost through the upper surface due to re-radiation from the medium, and free convection. The over-arching goal of this thesis is to collect all of the information required to analyze such a device.

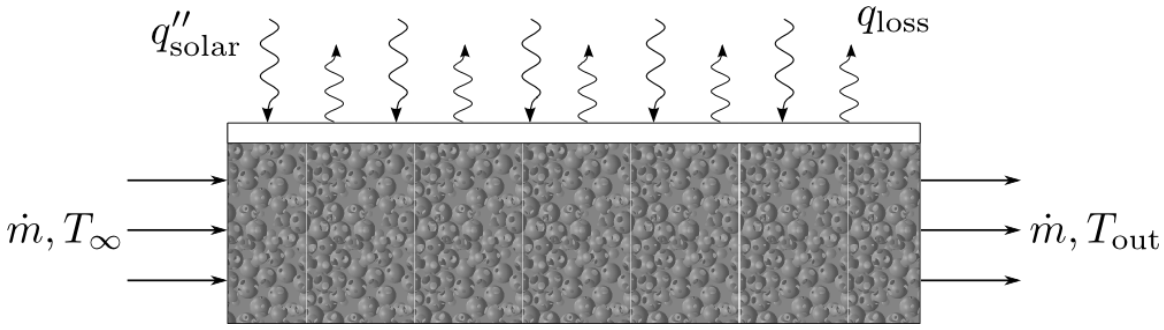


Figure 1.1 A single pass volumetric solar collector

This chapter contains the necessary background information to understand the content in chapters 2 and 3. After a literature review, the volume averaging process will be carried out for the relevant transport equations, the methods used to identify relevant material properties, and an introduction of how the continuum Monte-Carlo (MC) method may be applied to account for radiation transport.

## 1.1 Literature Review

Before detailing the present work regarding radiation in porous media, it is necessary to consider the research efforts to this point. The topics of volume averaging in porous media, pore level modeling, radiation in porous media, and solar collectors will be reviewed.

### 1.1.1 Volumetric Solar Receivers

Volumetric Solar Receivers (VSRs) have been analyzed as early as 1982 [3]. VSRs employ a heterogeneous material to absorb incident solar radiation and transfer heat to a working fluid. The material employed may be a porous matrix (the heat is transferred to the working fluid via convection), or a fluidized bed (the heat is conducted from the interstitial phase to the carrier fluid). This section will review applications where stationary porous matrices are used as the volumetric receiver.

Fend et al. [4, 5] have experimentally tested the performance of foam ceramics, SiC fiber mesh, ceramic catalyst carriers, and metallic catalyst carriers. The ceramic foam and fiber mesh were found to have superior performance because of their large specific surface

areas and favorable pressure losses. Some flow instabilities have been observed and explained by Pitz-Paal et al. [6] and Becker et al. [7]; it was found that the instabilities were caused by the dependence of viscosity on temperature, creating a two-way coupling between the energy and momentum equations. The instability is manifest as a non-monotonic relation between pressure drop across an irradiated foam sample and the air temperature, however the instability vanishes for low irradiation or whenever the ratio between Darcy and Forchheimer coefficients exceeds a critical value.

Wu et al. [8] used CFD software to analyze an axis symmetric porous plug wherein radiation is incident on the front face of the plug. Hischier et al. [9] have performed CFD analyses of a solar receiver wherein a concentrator focuses solar energy into a cylindrical cavity of absorbing material which transfers heat via conduction and convection to an annulus of porous material. Air is forced through the porous annulus to extract the sensible heat. The results indicate this is a very effective design, attaining thermal efficiencies in the range of ~80% while the outlet air temperature can reach 1000˚C!

Dhiman et al. [10] forced air through layers of wire meshes in single- and double-pass configurations. Experimentally determined thermohydraulic efficiencies were found to agree well with predictions from text book heat transfer correlations. More recently, Singh & Dhiman [11] have used a response surface methodology to optimize the design of a forced-air double-pass wire mesh screen solar collector. Optimal values of mass flow rate, channel height, and the fraction of recycled mass flow are reported.

### 1.1.2 Microstructure Modeling

A significant portion of this thesis describes a novel process for generating physically realistic digital representations of carbon foam. The rationale behind this effort and similar attempts by earlier researchers will be described in this section.

In order to identify the coefficients of closure terms and effective material properties that appear in the volume-averaged transport equations, an inverse analysis must be performed on a Representative Elementary Volume (REV) of the porous material of

interest. An example of this process is the identification of Darcy permeability and Forchheimer coefficient. Whitaker [12] has derived the Darcy-Forchheimer equation:

$$\frac{dp}{dx} = \frac{\mu}{K} u_x + \frac{\rho c_f}{\sqrt{K}} |u_x| u_x. \tag{2.1}$$

Equation (2.1) is a simplified 1D form of the momentum equation, where the pressure gradient, $\frac{dp}{dx}$, has been expressed as a quadratic function in terms of the extrinsic, or superficial, velocity $u_x$. The permeability, $K$, and the Forchheimer coefficient, $c_f$, may be found from specific closure problems formulated by Whitaker [12], however that analysis still requires a representation of the pore level microstructure. $K$ and $c_f$ are assumed to be complicated functions of the geometry of the solid matrix. Rather than hypothesize about how they might be calculated, it is much more straightforward to perform a series of experiments or simulations, enforcing a range of extrinsic velocities, and extracting the pressure drop across the domain. $K$ and $c_f$ may be determined via an inverse analysis of the results. In any case, a representation of the microstructure is required, and many researchers have proposed various methods for obtaining adequate REVs.

The first, and probably the most obvious method, is to acquire a physical sample of the porous material of interest, and perform a series of **experiments** on the sample to obtain the relevant data. This approach has been carried out by Gallego & Klett [13] to evaluate heat transfer coefficients for two reticulated carbon foams and two meso-phase pitch carbon foams. Straatman et al. [2] ran experiments on four different graphitic foams to determine hydraulic and heat transfer coefficients.

Alternatively, REVs may be reconstructed from **Computer Tomography (CT) scans** of a physical sample of the microstructure of interest. Once a digital representation of the microstructure is obtained, simulations may be performed (discretizing the digital model if necessary) and post-processed to infer the coefficients of interest. Nakashima et al. [14] reconstructed X-ray tomography scans to obtain digital REVs of packed beds, and

identified porosity, surface-to-volume ratio, and tortuosity. Maruyama et al. [15] and Anghelescu [16] digitally reconstructed samples of carbon foam and performed subsequent analyses to determine thermal and mechanical properties. More recently, the method has been applied by Haussener, in collaboration with other researchers, to determine effective hydraulic, thermal, and radiative transport properties for reticulate porous ceramics [17], reacting packed beds [18, 19], and snow [20].

CT scanning equipment is expensive, and, depending on the porous material one wishes to study, porous media materials may be also be expensive. These costs have motivated researchers to imagine REVs which would render the scanning equipment and material samples unnecessary. A popular substitute REV is a **unit-cell**. A unit-cell is a 3D periodic geometry representing a single pore deep within the porous domain, typically constructed by applying Boolean operations to combine simple geometric shapes. Geometric parameters such as porosity and surface-to-volume ratio of a unit-cell can easily be calculated using geometric relations, and, because of their simple construction, they are often easy to mesh for continuum simulations. A unit-cube model has been proposed by Yu et al. [21] who employed the Boolean subtraction of a sphere from a cube to obtain hydraulic and thermal properties for Spherica-Void-Phase (SVP) porous media. Boomsma & Poulikakos [22] first proposed the use of a tetrakaidecahedron shape, also known as the Kelvin cell, to predict thermal conductivity in metal foams. Dai et al. [23] identified and corrected some mistakes in Boomsma & Poulikakos' formulation and proposed an extension of the method for calculating thermal conductivity. Kumar et al. [24] have used Kelvin cell to evaluate the hydraulic and thermal properties of open-cell metal foams, and Sihn et al. [25] have used the Kelvin cell to predict effective Young's moduli and Poisson's ratios of carbon foams. Leong & Li [26] proposed a unique unit cell, comprised of a cubic shell where spheres have been subtracted from the corners to analyze hydraulic and thermal properties of carbon foam.

While the unit cell models are favourable because of their simplicity, they fail to capture the randomness of porous structures; specifically, pores are aligned along pre-defined channels resulting in an unrealistically anisotropic structure, and all the pores are assumed to be equally sized. This has motivated researchers to develop methods to

produce REVs which contain both variations in pore size and isotropy. These REVs have not been explicitly classified in the literature, so in this thesis they will be referred to as **stochastic REVs**, as there is usually an element of randomness to their generation. Kırca et al. [27] modeled pitch-based carbon foam REVs by placing spherical bubbles randomly within a cubic domain, and choosing the bubble radii to obtain the desired porosity, average bubble radius, and interference between neighbouring bubbles. Finite Element (FE) analyses were performed to determine the effective Young's modulus and Poisson's ratio. Wang & Pan [28] suggested a random-generation growth method, wherein representations of open-cell metal foams are generated by randomly placing points in a 3D domain and stochastically linking neighbouring nodes. Thermal conductivity was predicted from the resulting structure. More recently, Chueh et al. [29] modeled SVP porous media using the 'drop-and-roll' method of Visscher and Bolsterli [30]. Using this method they were the first researchers to obtain cubic, stochastic REVs which were periodic in two directions. The REVs were used in a random walk simulation to predict thermal conductivity.

### 1.1.3 Modeling Thermal Radiation in Porous Media

As mentioned above, the average behavior of radiation in porous media is the same as that of other participating media. Consequently, the methods developed to account for radiation transport in homogenous participating media may be used with few modifications. The present interest is to decide which method is most suitable for implementation within the finite volume conjugate porous/fluid/solid Fortran code developed by Betchen et al. [31] to solve problems involving radiation in porous media.

The traditional Radiative Exchange Method (REM) was developed to analyze radiative heat transfer between surfaces inside enclosures filled with non-participating media. A description of the REM may be found in undergraduate heat transfer textbooks such as Incropera & DeWitt [32] as well as dedicated radiation heat transfer texts [33, 34]. The REM requires the analyst to divide the surfaces in the enclosure of interest into isothermal surface elements, and determine the view factors between each pair of surface elements. Then the heat flux leaving each surface may be determined by finding the difference between the emitted energy from the element and the incoming energy from

all other elements. The **Zonal Method** (ZM) is an extension to the REM developed by Hottel & Cohen [35] to model enclosures with participating media. In the ZM, the volume within the enclosure is broken down into isothermal elemental volumes and the surfaces are divided into surface elements; both are referred to as zones. Exchange factors may be determined between zones as described by Hottel & Cohen [35] or by Larsen & Howell [36]. An energy balance for each zone may be written in terms of the heat fluxes from all other zones. Yuen [37] has developed a computationally efficient and robust implementation of the ZM for problems involving property for in-homogenous non-gray media. The method has not yet been applied to domains involving porous media.

The method of spherical harmonics, known as **the $P_N$ approximation**, was first proposed by Jeans [38] in his study of radiation heat transfer in stars. The method has been thoroughly described by Modest [34]. Intensity at a single point travelling in a single direction is represented as a two-dimensional Fourier series, where each term in the inner sum is the product the average intensity at the point and spherical harmonic function characterized by Legrende polynomials. Substitution into the RTE leads to an infinite set of coupled differential equations for an infinite number of moments. To render the method useful the Fourier series is truncated to $N$ moments.

The **Discrete Ordiantes Method** (DOM) was first introduced by Chandrasekhar [39]. The method requires that the RTE be solved at discrete points in space for a discrete number of directions, without integration over a local solid angle [40]. A weighting factor is then assigned to each direction such that integration of the intensity multiplied by the weighting function over all solid angles yields a known constant when the intensity is uniform. Thus the weighting function is required for two calculations: the in-scattering term, and the radiation source term in the energy equation. This convolution of the local intensity with a weighting function is referred to as quadrature in the literature. The speed and accuracy of various weighting functions have been investigated by Koch et al. [41] and Koch & Becker [42]. Malico & Pereira [43] have employed the DO method to study the importance of radiation and radiative properties to porous media combustion problems by way of analysis of a porous burner. It was found that inclusion of radiation within the model allowed for more accurate prediction of the temperature profile in the

post-flame region while pertubing the extinction coefficient and scattering albedo also influenced the solution. Raithby [44] has critisized the method for its failure to conserve radiant energy exactly for some quadratures.

The **Finite Volume Method** (FVM) applied to the RTE was first introduced by Raithby & Chui [45]. The method is a straightforward extension of the well known FVM [46], and it should not be confused with the common implementation of the DOM, known as DO-FVM. Implementation of the FVM requires that the problem domain be discretized into discrete volumes where the transport properties of interest are assumed to be constant within each control volume during every time-step. To solve for radiation transport, each control volume is subdivided into finite solid angles. Radiation is then conserved within each solid angle for each control volume. Several researchers applied the FVM to study multi-physics problems in porous domains. Slimi et al. [47] have studied buoyant flows within a porous vertical channel exposed to thermal radiation, and found that the heat transferred to the fluid increases with optical thickness and wall emissivity, and surprisingly, decreasing effective thermal conductivity within the solid phase. Kamel et al. [48] have proposed a variation on the method called FT*n*-FVM which addresses some of the shortcomings of the traditional FVM, such as false scattering, and demonstrated the improvements through the analysis of an L-shaped domain.

Coelho et al. [49] have analyzed the performance of three configurations of 2D and 3D enclosures with baffles filled with participating media using the ZM, Radiative Transfer Method (RTM), DOM, and FVM. All methods were found to obtain the correct solutions for the problems, however both the DOM and the FVM required less computation time than the ZM and the RTM in all cases. Little difference was observed between the accuracy of the DOM and the FVM.

The **Monte-Carlo Method** (MCM) differs substantially from the DO and FV methods in that the aim is not aim to solve the RTE directly; instead the progresses of individual rays or ray bundles are tracked throughout the domain [50]. Siegel & Howell [33] and Modest [34] both provide excellent detailed descriptions of the MCM. Rays are stochastically emitted, scattered, or absorbed at solid surfaces, participating volumes or boundaries with

a specified amount of radiant energy. Emitted energy is withdrawn from the source and deposited at the destination where absorption occurs. The primary advantage of the MCM is that it simulates the process of radiation transport rather than modeling it; the emission, reflection, scattering, and absorption of photons is nearly random on the microscopic scale, and the MCM approximates this behavior. Consequently, accurate solutions may nearly always be obtained when enough rays are launched. The method is not free of shortcomings; Howell [51] documents two computational issues during his Monte Carlo simulations of a gray gas between parallel plates: for weakly absorbing media, few ray bundles are absorbed within the media compared to the number absorbed by the walls so a large number of rays must be cast to resolve the temperature field. Conversely, when the solution is optically thick, a large number of rays are exchanged between neighboring volumes causing significant increase in computation time, a process which could more efficiently modeled by a diffusion approximation [33].

Hischier et al. [52] have independently implemented the Rosseland approximation, the $P_1$ method, and the MCM to solve the radiation field within a porous annulus of a volumetric solar receiver. A plot of the radiative source term over the radial direction indicated excellent agreement between $P_1$ and MC methods over the radius, while the Rosseland approximation predicted much higher heat fluxes near the center due to a relatively small optical thickness. Unsurprisingly, the computation time of the $P_1$ solution was much smaller than the MC solution.

Finally, Modest [34], who has described all of the above methods in full detail, presents a succinct comparison of the methods, indicating that the MC, FV, and DO methods are the only methods whose accuracies may be improved to an arbitrary level through casting additional rays or refining computational grids. He also mentions that the $P_1$ approximation is easier to apply than the FV and DO methods, and yields very accurate solutions for optically thick media.

In the end, the MCM was chosen for its ease of implementation and apparent accuracy. The problems to be studied require relatively small grid sizes, and the time to compute radiative heat fluxes in a few preliminary calculations was on the order of a few minutes.

## 1.2 Governing Equations

To predict the performance of an engineering design in the absence physical testing and suitable empirical correlations, the relevant conservation equations must be solved. When analyzing a porous media solar collector with volumetric absorption, the mass, momentum, energy, and radiation conservation equations. The instantaneous forms of these equations are presented in sections 1.2.1 - 1.2.4. Depending on the problem at hand, additional terms may be included in each governing equation to account for various effects, and adequate boundary conditions must be applied to characterize quantities outside the domain.

### 1.2.1 Conservation of Mass

The conservation of mass equation is given as follows:

$$\frac{\partial \rho}{\partial t} + \nabla \cdot \rho \mathbf{u} = 0, \tag{2.2}$$

where $\rho$ is the density, and $\mathbf{u}$ is the velocity vector. In all of the problems discussed in this thesis, the flows analyzed are assumed to be not only incompressible, but constant density. Under this assumption the conservation of mass may be simplified to

$$\nabla \cdot \mathbf{u} = 0, \tag{2.3}$$

which is often referred to as the continuity equation.

### 1.2.2 Conservation of Momentum

The conservation of momentum for a Newtonian fluid is given as:

$$\rho \frac{\partial \mathbf{u}}{\partial t} + \rho \mathbf{u} \cdot \nabla \mathbf{u} = -\nabla p + \rho \mathbf{g} + \mu \nabla^2 \mathbf{u}, \tag{2.4}$$

where $p$ is the pressure within the control volume, $\mathbf{g}$ is the gravity vector, and $\mu$ is the viscosity of the fluid.

### 1.2.3 Conservation of Energy

The conservation of energy may be written as follows [32, 33]:

$$\underbrace{\rho c_p \frac{dT}{dt}}_{\substack{\text{Transient term;}\\ \text{rate of energy}\\ \text{storage}}} + \underbrace{\rho c_p \mathbf{u}\cdot\nabla T}_{\substack{\text{Advective term;}\\ \text{energy transport via}\\ \text{bulk fluid motion}}} = \underbrace{\nabla\cdot k\nabla T}_{\substack{\text{Diffusion term;}\\ \text{energy transport}\\ \text{via conduction}}} - \underbrace{\nabla\cdot\mathbf{q}_{\mathrm{r}}}_{\substack{\text{Source term;}\\ \text{energy loss/gain}\\ \text{by radiation}\\ \text{emission /absorption}}} - \underbrace{p\nabla\cdot\mathbf{u}}_{\substack{\text{Source term;}\\ \text{energy loss by}\\ \text{volumetric expansion}}} + \underbrace{\Phi}_{\substack{\text{Source term;}\\ \text{energy gain by}\\ \text{viscous dissipation}}}; \tag{2.5}$$

It can immediately be seen that the second source term, characterizing energy loss by volumetric expansion, disappears when the continuity equation (2.3) is inserted. Additionally, the final source term will be neglected in this thesis, as viscous dissipation is small compared to the other terms for all problems discussed in this thesis. With these simplifications, Eq. (2.5) is reduced to:

$$\rho c_p \frac{dT}{dt} + \rho c_p \mathbf{u}\cdot\nabla T = \nabla\cdot k\nabla T - \nabla\cdot\mathbf{q}_{\mathrm{r}}. \tag{2.6}$$

The mathematical form of the radiation source term will be presented in section 1.2.4.

### 1.2.4 Radiative Transfer Equation

On the sub-atomic scale, radiation transfer occurs via the movement of photons within a domain [33]. As with momentum and energy, engineers will desire a continuum approximation which captures the bulk movement of photons without needing to track them individually. The quantity characterizing this movement is called *intensity*. Before presenting the equation of radiation transfer, two fundamental differences between radiation transport and transport of more tangible quantities (e.g. momentum or energy) will be highlighted.

First, consider the fact that momentum and, radiation excepted, energy must be associated with a finite mass. This understanding is manifest by the presence of advective terms in each of the above equations, which represent the notion that quantities can be

*carried* by mass. For all intents and purposes, intensity has no such reservations, which is why it can propagate unimpeded through a vacuum. While this fact precludes the use of a control mass to derive the equation of radiation transfer, a second quality of radiation provides a suitable starting point.

It is known that, outside of relativistic effects such as diffraction [53], photons travel along straight paths. The inclusion of these relativistic effects is uncommon in the engineering treatment of thermal radiation heat transfer, and will not be considered in this thesis. The linear motion of photons can be exploited by considering the conservation of intensity along a path. This is the approach taken by [33, 34] to derive the Radiative Transfer Equation (RTE):

$$\underbrace{\frac{1}{c}\frac{\partial I_\lambda(\mathbf{r},\hat{\mathbf{s}})}{\partial t}}_{\substack{\text{Unsteady term;}\\ \text{change in intensity}\\ \text{at position } \mathbf{r}\\ \text{per unit time}}} + \underbrace{\hat{\mathbf{s}}\cdot\nabla_{\mathbf{r}} I_\lambda(\mathbf{r},\hat{\mathbf{s}})}_{\substack{\text{Change in intensity at}\\ \text{at position } \mathbf{r} \text{ in}\\ \text{direction } \hat{\mathbf{s}}}} = \underbrace{-\left[\kappa_\lambda + \sigma_{s,\lambda}\right] I_\lambda(\mathbf{r},\hat{\mathbf{s}})}_{\text{Loss by absorption and scattering}} + \underbrace{n^2 \kappa_\lambda I_{\lambda,b}(\mathbf{r})}_{\text{Gain by emission}} \tag{2.7}$$

$$+ \underbrace{\frac{\sigma_{s,\lambda}}{4\pi}\int_{4\pi} I_\lambda(\mathbf{r},\hat{\mathbf{s}}_{\text{in}})\Phi(\lambda,\hat{\mathbf{s}}_{\text{in}},\hat{\mathbf{s}})\,\mathrm{d}\Omega_{\text{in}}}_{\text{Gain by scattering into direction } \hat{\mathbf{s}}},$$

where $\kappa_\lambda$ and $\sigma_{s,\lambda}$ are the wavelength specific absorption and scattering coefficients, respectively, and $c$ is the speed of light. In a great deal of engineering problems, the flight times of the rays are much smaller than all other characteristic timescales, and the radiation field may be assumed quasi-steady. The unsteady term will be neglected for the remainder of this thesis. Typically, the index of refraction, $n$, appearing in the emission term of Eq. (2.7), is lumped into the blackbody emissive intensity $L_{\lambda,\mathrm{b}}(\mathbf{r})$, the emission *within the medium* ($n = \text{const}$). In preparation for dealing with refractive boundaries between phases, it is more convenient to pull out the $n^2$ term and read $L_{\lambda,\mathrm{b}}(\mathbf{r})$ as the emission *within a vacuum* ($n = 1$) similar to the derivation in chapter 1 of the text by Modest [34].

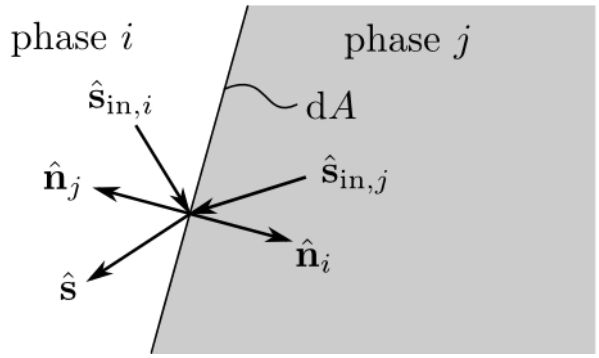


Figure 1.2: Interface phenomena; rays emanating from the interface element $\mathrm{d}A$ into direction $\hat{\mathbf{s}}$ may be reflected from phase $i$, and transmitted from phase $j$.

The interface condition between two semi-transparent boundaries applicable to Eq. (2.7) (shown in Figure 1.2) is defined as the sum of the reflected portion from phase $i$ and the transmitted (refracted) portion from phase $j$:

$$\begin{aligned} I_i\left(\mathbf{r}_{dA},\hat{\mathbf{s}}\right) &= \int_{\Omega_{\text{in}}:\hat{\mathbf{s}}_{\text{in}}\cdot\mathbf{n}_i>0} \rho_{ij}''\left(\hat{\mathbf{s}}_{\text{in}},\hat{\mathbf{s}}\right) I_i\left(\mathbf{r}_{dA},\hat{\mathbf{s}}_{\text{in}}\right)\hat{\mathbf{s}}_{\text{in}}\cdot\hat{\mathbf{n}}_i d\Omega_{\text{in}} \\ &-\int_{\Omega_{\text{in}}:\hat{\mathbf{s}}_{\text{in}}\cdot\mathbf{n}_i<0} \tau_{ji}''\left(\hat{\mathbf{s}}_{\text{in}},\hat{\mathbf{s}}\right) I_j\left(\mathbf{r}_{dA},\hat{\mathbf{s}}_{\text{in}}\right)\hat{\mathbf{s}}_{\text{in}}\cdot\hat{\mathbf{n}}_i d\Omega_{\text{in}}, \end{aligned} \tag{2.8}$$

where the sum of the reflected and transmitted portions must sum to one:

$$\begin{aligned} &-\int_{\Omega_{\text{in}}:\hat{\mathbf{s}}_{\text{in}}\cdot\mathbf{n}_i>0} \rho_{ij}''\left(\hat{\mathbf{s}}_{\text{in}},\hat{\mathbf{s}}\right)\hat{\mathbf{s}}_{\text{in}}\cdot\hat{\mathbf{n}}_i d\Omega_{\text{in}} + \int_{\Omega_{\text{in}}:\hat{\mathbf{s}}_{\text{in}}\cdot\mathbf{n}_i<0} \tau_{ji}''\left(\hat{\mathbf{s}}_{\text{in}},\hat{\mathbf{s}}\right)\hat{\mathbf{s}}_{\text{in}}\cdot\hat{\mathbf{n}}_i d\Omega_{\text{in}} \\ &= \bar{\rho}_{ij}\left(\hat{\mathbf{s}}_{\text{in}}\right) + \bar{\tau}_{ji}\left(\hat{\mathbf{s}}_{\text{in}}\right) = 1. \end{aligned} \tag{2.9}$$

If the $j$ phase is considered opaque, an alternate boundary condition applies:

$$\begin{aligned} I_i\left(\mathbf{r}_{\text{int}},\hat{\mathbf{s}}\right) &= \int_{\Omega_{\text{in}}:\hat{\mathbf{s}}_{\text{in}}\cdot\mathbf{n}_i>0} \rho_{ij}''\left(\hat{\mathbf{s}}_{\text{in}},\hat{\mathbf{s}}\right) I_i\left(\mathbf{r}_{\text{int}},\hat{\mathbf{s}}\right)\hat{\mathbf{s}}_{\text{in}}\cdot\hat{\mathbf{n}}_i d\Omega_{\text{in}} \\ &+n_i^2\varepsilon_{ji}\left(\hat{\mathbf{s}}\right) I_{b,i}\left(\mathbf{r}_{\text{int}}\right), \\ &\hat{\mathbf{s}}\cdot\hat{\mathbf{n}}_i < 0. \end{aligned} \tag{2.10}$$

The radiation source term in the energy equation (2.6) has been derived by Siegel & Howell [33]:

$$\nabla \cdot \mathbf{q}_r = 4\int_0^\infty a_\lambda \left[ e_{\lambda,b}(T) - \pi \bar{i}_\lambda \right] d\lambda. \tag{2.11}$$

where $e_{\lambda,b}(T)$ is the emissive power of a blackbody per unit wavelength. Equation (2.11) represents the contributions of the two terms inside the integrand: it is the difference between the emitted and absorbed power. The mean intensity $\bar{i}_\lambda$ is defined as:

$$\bar{i}_\lambda \equiv \frac{1}{4\pi}\int_0^{4\pi} i'_\lambda(\omega, \kappa_\lambda) d\omega. \tag{2.12}$$

For convenience, the Plank-mean absorption coefficient is introduced, which represents the wavelength-average absorption:

$$\kappa_P \equiv \frac{\int_0^\infty \kappa_\lambda e_{\lambda,b}(T) d\lambda}{\int_0^\infty e_{\lambda,b}(T) d\lambda} = \frac{\int_0^\infty \kappa_\lambda e_{\lambda,b}(T) d\lambda}{\sigma T^4}. \tag{2.13}$$

Additionally, the wavelength-integrated mean intensity may be defined as:

$$\bar{i} \equiv \int_0^\infty \bar{i}_\lambda d\lambda. \tag{2.14}$$

Using Eq. (2.13) and (2.14), (2.11) may be simplified:

$$\nabla \cdot \mathbf{q}_r = 4\kappa_P \left[ \sigma T^4 - \pi \bar{i} \right]. \tag{2.15}$$

For the remainder of this thesis, the wavelength subscripts will be dropped as the present work deals only with wavelength-averaged properties.

## 1.3 Volume Averaging the Governing Equations

The process of volume averaging the governing equations was first presented and carried out by Whitaker [54] and Slattery [55], and has since been the topic of a large number of subsequent publications, many of which address the topic of closure terms.

The closure of the volume-averaged mass-momentum equations has been revisited by Whitaker [12], who derived Darcy's law with the Forchheimer correction term, and identified the closure problems to be solved to obtain the Forchheimer coefficient. Darcy and Forchheimer coefficients have since been determined using this method for a variety of idealized microstructures including a unit-cube model [21], square tubes in a cross-flow [56], and a tetrakaidecahedron shape [24].

The energy equation has also been volume averaged by Whitaker [57]. Treatment of the energy equation depends on whether local thermal equilibrium may be assumed. The thermal equilibrium assumption states that, at each point within the porous domain, the temperature of the solid and fluid phases are equal. Thus, when the thermal equilibrium assumption is invoked, one energy equation is used to calculate the temperature field; otherwise two equations must be solved to obtain temperature fields for the fluid and solid phase. Quintard and Whitaker [58] have derived the volume-averaged forms of the energy equation for both cases and Quintard et al. [59] have proposed closure models for the non-equilibrium case.

Of special interest for this thesis is the volume-averaged radiation transfer equation. The volume-averaged equation was first given by Zeghondy & Iacona [60] for a heterogenous media with one transparent phase and one opaque phase, however the derivation was omitted. The general derivation for two semi-transparent phases was completed only recently by Lipiński et al. [61]. A follow-up article by Lipiński et al. extended the derivation for multi-component media [62]. An interesting consequence of the derivation is that no closure terms appear in the final equation. This indicates that the macroscopic behavior of radiation transfer in porous media is not fundamentally different than that of homogenous participating media, such as gases. It should be noted, however, that the bulk properties present in the final equation must be determined using pore-level simulations.

When analyzing transport phenomena in porous media, the straightforward technique is to apply the governing equations of section 1.1 to the given problem, analyzing a conjugate domain with distinct fluid and solid regions. While this approach is possible,

an absurd amount of computational memory would be required to solve such problems. This results from the fact that all the interconnections of the microstructure must be fully defined to resolve all of the fluid-solid interfaces within the domain. The analyst must also discretize the domain into volumes small enough to resolve the pertinent flow features. While generating the meshes for the pore-level analyses of section 2.4.2 it has been observed that a cubic sample of approximately 5 sphere diameters in edge length requires approximately 4 GB of Random Access Memory (RAM); about half of the memory resources available on the workstation. During the meshing process, up to 6 GB of RAM usage has been observed. From these observations it can be surmised that many design problems would be computationally prohibitive to analyze without the use of High Performance Computing (HPC).

This limitation is analogous to that encountered when simulating turbulent flows; in such problems the imbalance between inertial and viscous forces cause small flow features known as eddies to form, whose characteristic dimensions are minute compared to the global (or integral) length scale of the domain. The naive approach is to create meshes fine enough to resolve those flow features (such computations are known as Direct Numerical Simulations). However, in many problems the required computational memory and / or computation times are prohibitively large. To circumvent these issues, researchers modify the transport equations of interest to account for the effects of the small scale features by the augmentation of material properties, add new terms in the equations, or couple the mass-momentum equations to fictitious transport equations.

When modeling porous media, a similar approach is taken: the governing equations are *volume-averaged*. The term volume-averaging was coined by Whittaker [12], and it is his derivation of the volume-averaged mass-momentum equations that will be followed here. The volume-averaged energy, and radiative transport equations will be derived thereafter.

The reader should keep in mind that, although volume-averaging (or any other averaging technique, for that matter) is a useful procedure, it should not be confused with the *discretization* of transport equations, which is a further transformation to allow solutions to be obtained using numerical methods. When necessary, discretization is always

performed after the averaging process. The Finite Volume Method (FVM) of Patankar [46] is the discretization applied to the volume averaged mass, momentum, and energy equations of the conjugate code used in this thesis, and the Monte-Carlo (MC) method has been applied to the volume averaged Radiative Transfer Equation.

### 1.3.1 Volume Averaging Theorems

Two theorems will be instrumental in developing the volume-averaged transport equations in this work. The first definition is the extrinsic or superficial average which relates a volume-averaged quantity to its local counterpart:

$$\langle \phi_m \rangle \equiv \frac{1}{V} \int_{V_m} \phi_m dV. \tag{2.16}$$

The intrinsic average is defined similarly:

$$\langle \phi_m \rangle^m \equiv \frac{1}{V_m} \int_{V_m} \phi_m dV. \tag{2.17}$$

These definitions are related:

$$\langle \phi_m \rangle = \varepsilon \langle \phi_m \rangle^m, \tag{2.18}$$

where $\varepsilon$ is the volume fraction of phase $m$. The Spatial Averaging Theorem (SAT) is given as:

$$\underbrace{\langle \nabla \phi_m \rangle}_{\substack{\text{Superficial average} \\ \text{of gradient of quantity} \\ \text{within phase } m}} = \underbrace{\nabla \langle \phi_m \rangle}_{\substack{\text{Gradient of superficial} \\ \text{average of quantity} \\ \text{within phase } m}} + \underbrace{\frac{1}{V} \int_{A_{mn}} \hat{\mathbf{n}}_{mn} \phi_m dA}_{\substack{\text{Volume average of } \phi \\ \text{crossing the interface from} \\ n \text{ to } m}}. \tag{2.19}$$

Each of the conservation equations of sections 1.3.2 - 1.3.5 are volume-averaged by applying $\langle\ \rangle$ to each term in the equation, and using equations (2.16) - (2.19) to obtain an expression in terms of the current transport quantity. Terms which cannot be reduced

are called closure terms. Such terms must be appropriately modeled, and their coefficients determined from pore level simulation results.

### 1.3.2 Conservation of Mass

The (incompressible) volume-averaged conservation of mass equation for the fluid phase is given as:

$$\left\langle \nabla \cdot \mathbf{u}_f \right\rangle = 0. \tag{2.20}$$

SAT (Equation (2.19)) may be applied to yield:

$$\left\langle \nabla \cdot \mathbf{u}_f \right\rangle = \nabla \left\langle \mathbf{u}_f \right\rangle + \frac{1}{V} \int_{A_{fs}} \hat{\mathbf{n}}_{fs} \cdot \mathbf{u}_f \, dA. \tag{2.21}$$

The no-slip condition necessitates

$$\mathbf{u}_f \Big|_{A_{fs}} = 0. \tag{2.22}$$

Therefore the second term in Eq. (2.21) drops out, leaving

$$\nabla \cdot \left\langle \mathbf{u}_f \right\rangle = 0. \tag{2.23}$$

The solid matrix is assumed to be stationary rendering the conservation of mass equation for the solid phase unnecessary.

### 1.3.3 Conservation of Momentum

The conservation of momentum equation (2.4) may be volume averaged as follows

$$\left\langle \rho_f \frac{\partial \mathbf{u}_f}{\partial t} \right\rangle + \left\langle \rho_f \mathbf{u}_f \cdot \nabla \mathbf{u}_f \right\rangle = -\left\langle \nabla p_f \right\rangle + \left\langle \rho_f \mathbf{f} \right\rangle + \left\langle \mu_f \nabla^2 \mathbf{u}_f \right\rangle. \tag{2.24}$$

Fluid properties are assumed to be constant, so density and viscosity may be moved outside the averaging brackets:

$$\rho_f \left\langle \frac{\partial \mathbf{u}_f}{\partial t} \right\rangle + \rho_f \left\langle \mathbf{u}_f \cdot \nabla \mathbf{u}_f \right\rangle = -\left\langle \nabla p_f \right\rangle + \rho_f \left\langle \mathbf{f} \right\rangle + \mu_f \left\langle \nabla^2 \mathbf{u}_f \right\rangle. \tag{2.25}$$

Each of the terms in Eq. (2.25) will be examined for potential simplifications beginning with the first term on the LHS. Invoking definition (2.16) yields

$$\left\langle \frac{\partial \mathbf{u}_f}{\partial t} \right\rangle = \frac{1}{V}\int_{V_f} \frac{\partial \mathbf{u}_f}{\partial t} dV = \frac{\partial}{\partial t}\left( \frac{1}{V}\int_{V_f} \mathbf{u}_f dV \right) = \frac{\partial \left\langle \mathbf{u}_f \right\rangle}{\partial t}. \tag{2.26}$$

Note the order of differentiation and integration may be interchanged since the volume of the fluid phase is independent of time. In addition, (2.16) is used in the final step.

The convective term requires use of the SAT:

$$\left\langle \mathbf{u}_f \cdot \nabla \mathbf{u}_f \right\rangle = \left\langle \nabla \cdot \left( \mathbf{u}_f \mathbf{u}_f \right) \right\rangle = \nabla \cdot \left\langle \mathbf{u}_f \mathbf{u}_f \right\rangle + \frac{1}{V}\int_{A_{fs}} \mathbf{n}_{fs} \cdot \mathbf{u}_f \mathbf{u}_f dA = \nabla \cdot \left\langle \mathbf{u}_f \mathbf{u}_f \right\rangle. \tag{2.27}$$

The no-slip condition (Eq. (2.22)) was applied in the final step, causing the integral term to drop out. The $\left\langle \mathbf{u}_f \mathbf{u}_f \right\rangle$ term is the average of a product, and must be reduced to some combination of averages before it can be used in the final volume-averaged equation. The solution proposed by Whitaker [12] is to decompose the transport quantity as follows

$$\phi_m = \left\langle \phi_m \right\rangle^m + \tilde{\phi}_m, \tag{2.28}$$

where $\left\langle \phi_m \right\rangle^m$ is the spatial average as defined above and $\tilde{\phi}_m$ are the deviations from the average. The velocity decomposition is written as:

$$\mathbf{u}_f = \left\langle \mathbf{u}_f \right\rangle^f + \tilde{\mathbf{u}}_f. \tag{2.29}$$

Equation (2.29) may be used to decompose the average-product in Eq. (2.27):

$$\left\langle \mathbf{u}_f \mathbf{u}_f \right\rangle = \left\langle \left\langle \mathbf{u}_f \right\rangle^f \left\langle \mathbf{u}_f \right\rangle^f \right\rangle + \left\langle \left\langle \mathbf{u}_f \right\rangle^f \tilde{\mathbf{u}}_f \right\rangle + \left\langle \tilde{\mathbf{u}}_f \left\langle \mathbf{u}_f \right\rangle^f \right\rangle + \left\langle \tilde{\mathbf{u}}_f \tilde{\mathbf{u}}_f \right\rangle. \tag{2.30}$$

Now Eq. (2.30) must be analyzed term-by-term for simplifications. The first term can be simplified through use of Eq. (2.16)

$$\begin{aligned} \left\langle \left\langle \mathbf{u}_f \right\rangle^f \left\langle \mathbf{u}_f \right\rangle^f \right\rangle &= \frac{1}{V}\int_{V_f} \left\langle \mathbf{u}_f \right\rangle^f \left\langle \mathbf{u}_f \right\rangle^f dV = \left\langle \mathbf{u}_f \right\rangle^f \left\langle \mathbf{u}_f \right\rangle^f \frac{1}{V}\int_{V_f} dV \\ &= \left\langle \mathbf{u}_f \right\rangle^f \left\langle \mathbf{u}_f \right\rangle^f \langle 1 \rangle = \varepsilon \left\langle \mathbf{u}_f \right\rangle^f \left\langle \mathbf{u}_f \right\rangle^f, \end{aligned} \tag{2.31}$$

where the $\left\langle \mathbf{u}_f \right\rangle^f$ is already an averaged quantity, so it is assumed not to vary within the averaging volume.

The extrinsic average definition may also be used to simplify the second and third terms in Eq. (2.30)

$$\left\langle \left\langle \mathbf{u}_f \right\rangle^f \tilde{\mathbf{u}}_f \right\rangle = \frac{1}{V}\int_{V_f} \left\langle \mathbf{u}_f \right\rangle^f \tilde{\mathbf{u}}_f dV = \left\langle \mathbf{u}_f \right\rangle^f \left\langle \tilde{\mathbf{u}}_f \right\rangle, \tag{2.32}$$

$$\left\langle \tilde{\mathbf{u}}_f \left\langle \mathbf{u}_f \right\rangle^f \right\rangle = \frac{1}{V}\int_{V_f} \tilde{\mathbf{u}}_f \left\langle \mathbf{u}_f \right\rangle^f dV = \left\langle \tilde{\mathbf{u}}_f \right\rangle \left\langle \mathbf{u}_f \right\rangle^f. \tag{2.33}$$

The final term in Eq. (2.30) will be dealt with later. Inserting (2.31) - (2.33) yields

$$\left\langle \mathbf{u}_f \mathbf{u}_f \right\rangle = \varepsilon \left\langle \mathbf{u}_f \right\rangle^f \left\langle \mathbf{u}_f \right\rangle^f + \left\langle \mathbf{u}_f \right\rangle^f \left\langle \tilde{\mathbf{u}}_f \right\rangle + \left\langle \tilde{\mathbf{u}}_f \right\rangle \left\langle \mathbf{u}_f \right\rangle^f + \left\langle \tilde{\mathbf{u}}_f \tilde{\mathbf{u}}_f \right\rangle. \tag{2.34}$$

Furthermore, it can be argued that, since the quantity $\tilde{\mathbf{u}}_f$ represents fluctuations about an mean value, the average of the fluctuations must be zero, such that

$$\left\langle \tilde{\mathbf{u}}_f \right\rangle = 0. \tag{2.35}$$

Under this assumption, Eq. (2.34) may be further simplified:

$$\left\langle \mathbf{u}_f \mathbf{u}_f \right\rangle = \varepsilon \left\langle \mathbf{u}_f \right\rangle^f \left\langle \mathbf{u}_f \right\rangle^f + \left\langle \tilde{\mathbf{u}}_f \tilde{\mathbf{u}}_f \right\rangle. \tag{2.36}$$

The divergence of Eq. (2.36) must be evaluated for application in Eq. (2.27); it can be simplified as follows

$$\begin{aligned} \nabla \cdot \left\langle \mathbf{u}_f \mathbf{u}_f \right\rangle &= \nabla \cdot \left( \varepsilon \left\langle \mathbf{u}_f \right\rangle^f \left\langle \mathbf{u}_f \right\rangle^f + \left\langle \tilde{\mathbf{u}}_f \tilde{\mathbf{u}}_f \right\rangle \right) \\ &= \nabla \varepsilon \cdot \left( \left\langle \mathbf{u}_f \right\rangle^f \left\langle \mathbf{u}_f \right\rangle^f \right) + \varepsilon \nabla \cdot \left( \left\langle \mathbf{u}_f \right\rangle^f \left\langle \mathbf{u}_f \right\rangle^f \right) + \nabla \cdot \left\langle \tilde{\mathbf{u}}_f \tilde{\mathbf{u}}_f \right\rangle. \end{aligned} \tag{2.37}$$

The first term in Eq. (2.37) contains the gradient of porosity, $\nabla \varepsilon$. The porosity variation across the averaging volume is assumed to be negligible in the present analysis. The second term on the RHS contains intrinsic quantities. These can be substituted for their extrinsic counterparts using Eq. (2.18),

$$\varepsilon \nabla \cdot \left( \left\langle \mathbf{u}_f \right\rangle^f \left\langle \mathbf{u}_f \right\rangle^f \right) = \varepsilon \nabla \cdot \left( \varepsilon^{-2} \left\langle \mathbf{u}_f \right\rangle \left\langle \mathbf{u}_f \right\rangle \right) = \varepsilon^{-1} \nabla \cdot \left( \left\langle \mathbf{u}_f \right\rangle \left\langle \mathbf{u}_f \right\rangle \right). \tag{2.38}$$

With these simplifications Eq. (2.37) may be written as

$$\nabla \cdot \left\langle \mathbf{u}_f \mathbf{u}_f \right\rangle = \varepsilon^{-1} \nabla \cdot \left( \left\langle \mathbf{u}_f \right\rangle \left\langle \mathbf{u}_f \right\rangle \right) + \nabla \cdot \left\langle \tilde{\mathbf{u}}_f \tilde{\mathbf{u}}_f \right\rangle. \tag{2.39}$$

The pressure term in Eq. (2.25) may be expanded using the SAT (Eq. (2.19)):

$$\left\langle \nabla p_f \right\rangle = \nabla \left\langle p_f \right\rangle + \frac{1}{V} \int_{A_{fs}} \mathbf{n}_{fs} p_f \, dA. \tag{2.40}$$

In preparation for decomposition, $\left\langle p_f \right\rangle$ is exchanged for its intrinsic average using (2.18),

$$\left\langle \nabla p_f \right\rangle = \varepsilon \nabla \left\langle p_f \right\rangle^f + \left\langle p_f \right\rangle^f \nabla \varepsilon + \frac{1}{V} \int_{A_{fs}} \mathbf{n}_{fs} p_f \, dA. \tag{2.41}$$

As before, the porosity gradient may be neglected, and Eq. (2.41) can be reduced to

$$\left\langle \nabla p_f \right\rangle = \varepsilon \nabla \left\langle p_f \right\rangle^f + \frac{1}{V}\int_{A_{fs}} \mathbf{n}_{fs} p_f \, dA. \tag{2.42}$$

To deal with the integral term on the RHS, the pressure is decomposed according to the definition (2.28):

$$p_f = \left\langle p_f \right\rangle^f + \tilde{p}. \tag{2.43}$$

Inserting Eq. (2.43) into (2.42) gives

$$\left\langle \nabla p_f \right\rangle = \varepsilon \nabla \left\langle p_f \right\rangle^f + \frac{1}{V}\int_{A_{fs}} \mathbf{n}_{fs} \left\langle p_f \right\rangle^f dA + \frac{1}{V}\int_{A_{fs}} \mathbf{n}_{fs} \tilde{p} dA. \tag{2.44}$$

Through an analysis of length scales, Whitaker [12] shows that the following approximation is reasonable:

$$\frac{1}{V}\int_{A_{fs}} \mathbf{n}_{fs} \left\langle p_f \right\rangle^f dA \approx \left[ \frac{1}{V}\int_{A_{fs}} \mathbf{n}_{fs} dA \right] \left\langle p_f \right\rangle^f. \tag{2.45}$$

This approximation aligns with the intuition that the average pressure over the averaging volume is not expected to vary across the interfacial surface area.

To reduce the integral on the RHS of (2.45), the SAT will be applied to 1:

$$\left\langle \nabla 1 \right\rangle = \nabla \left\langle 1 \right\rangle + \frac{1}{V}\int_{A_{fs}} \mathbf{n}_{fs} dA, \tag{2.46}$$

where $\nabla 1 = 0$ and $\left\langle 1 \right\rangle = \varepsilon_f$. With these simplifications, Eq. (2.46) may be reduced to

$$\frac{1}{V}\int_{A_{fs}} \mathbf{n}_{fs} dA = -\nabla \varepsilon \approx 0, \tag{2.47}$$

where the porosity gradient has again been neglected. Inserting (2.47) into (2.45) and (2.45) into (2.44) yields

$$\left\langle \nabla p_f \right\rangle = \varepsilon \nabla \left\langle p_f \right\rangle^f + \frac{1}{V}\int_{A_{fs}} \mathbf{n}_{fs}\tilde{p}\,dA. \tag{2.48}$$

The viscous term in Eq. (2.25) may be broken down using the SAT:

$$\left\langle \nabla^2 \mathbf{u}_f \right\rangle = \left\langle \nabla \cdot \nabla \mathbf{u}_f \right\rangle = \nabla \cdot \left\langle \nabla \mathbf{u}_f \right\rangle + \frac{1}{V}\int_{A_{fs}} \mathbf{n}_{fs} \cdot \nabla \mathbf{u}_f \, dA. \tag{2.49}$$

The first term on the RHS of (2.49) requires a second application of SAT, so the fully expanded viscous term can be written

$$\begin{aligned} \left\langle \nabla^2 \mathbf{u}_f \right\rangle &= \left\langle \nabla \cdot \nabla \mathbf{u}_f \right\rangle = \nabla \cdot \left( \nabla \left\langle \mathbf{u}_f \right\rangle + \frac{1}{V}\int_{A_{fs}} \mathbf{n}_{fs} \cdot \mathbf{u}_f \, dA \right) \\ &+ \frac{1}{V}\int_{A_{fs}} \mathbf{n}_{fs} \cdot \nabla \mathbf{u}_f \, dA. \end{aligned} \tag{2.50}$$

The first integral in Eq. (2.50) drops out because of the no-slip condition (Eq. (2.22)). In order to reduce the last integral on the RHS of Eq. (2.50), the velocity is again decomposed using Eq. (2.29):

$$\frac{1}{V}\int_{A_{fs}} \mathbf{n}_{fs} \cdot \nabla \mathbf{u}_f \, dA = \frac{1}{V}\int_{A_{fs}} \mathbf{n}_{fs} \cdot \nabla \left\langle \mathbf{u}_f \right\rangle dA + \frac{1}{V}\int_{A_{fs}} \mathbf{n}_{fs} \cdot \nabla \tilde{\mathbf{u}}_f \, dA. \tag{2.51}$$

More length scale arguments provided by Whitaker [12] suggest that $\nabla \left\langle \mathbf{u}_f \right\rangle$ can be taken outside the integral. Applying this approximation and further simplifications yield:

$$\frac{1}{V}\int_{A_{fs}} \mathbf{n}_{fs} \cdot \nabla \mathbf{u}_f \, dA = \frac{1}{V}\int_{A_{fs}} \mathbf{n}_{fs} \cdot \nabla \tilde{\mathbf{u}}_f \, dA. \tag{2.52}$$

Thus, Eq. (2.50) may be written as:

$$\left\langle \nabla^2 \mathbf{u}_f \right\rangle = \nabla^2 \left\langle \mathbf{u}_f \right\rangle + \frac{1}{V}\int_{A_{fs}} \mathbf{n}_{fs} \cdot \nabla \tilde{\mathbf{u}}_f \, dA. \tag{2.53}$$

The body force term in Eq. (2.25) may be reduced by application of Eq. (2.16):

$$\left\langle \mathbf{f} \right\rangle = \frac{1}{V}\int_{V_f} \mathbf{f} dV = \mathbf{f}\frac{1}{V}\int_{V_f} dV = \varepsilon \mathbf{f}, \tag{2.54}$$

where the body force, $\mathbf{f}$, is assumed to be constant over the averaging volume.

Inserting equations (2.26), (2.39), (2.48), (2.53), and (2.54) into Eq. (2.25) and simplifying yields

$$\begin{aligned} &\rho_f \frac{\partial \left\langle \mathbf{u}_f \right\rangle}{\partial t} + \frac{\rho_f}{\varepsilon}\nabla\cdot\left(\left\langle \mathbf{u}_f \right\rangle\left\langle \mathbf{u}_f \right\rangle\right) = -\varepsilon\nabla\left\langle p_f \right\rangle^f + \mu_f\nabla^2\left\langle \mathbf{u}_f \right\rangle \\ &+\varepsilon\rho_f\mathbf{f} + \underbrace{\frac{1}{V}\int_{A_{fs}} \mathbf{n}_{fs}\cdot\left(-\mathbf{I}\tilde{p} + \mu_f\nabla\tilde{\mathbf{u}}_f\right)dA}_{\text{volume filter}} - \underbrace{\rho_f\nabla\cdot\left\langle \tilde{\mathbf{u}}_f\tilde{\mathbf{u}}_f \right\rangle}_{\text{surface filter}}. \end{aligned} \tag{2.55}$$

The last two terms in Eq. (2.55) are referred to as the volume filter and surface filter, respectively, because the micro-scale information obtained from the subsequent closure problems is filtered by these integrals. Also note that the second term on the RHS is referred to as the Brinkman correction [63]. The viscous term in the general momentum equation accounts for friction between neighbouring layers of fluid moving at unequal velocities. The Brinkman term still serves this purpose, although it is often negligible compared to the magnitudes of the volume and surface filters. Since the solid phase is assumed to be stationary, its momentum equation is unnecessary.

To obtain a more amiable equation for porous media calculations, Eq. (2.55) must be closed. This is a very lengthy process; rather than regurgitate it here, a brief summary will be provided, and more ambitious readers may refer to Ref. [12] for details. The closed, extrinsic form of the volume averaged momentum equation is given by Vafai & Tien [64]:

$$\rho_f \frac{\partial \langle \mathbf{u}_f \rangle}{\partial t} + \frac{\rho_f}{\varepsilon} \nabla \cdot \left( \langle \mathbf{u}_f \rangle \langle \mathbf{u}_f \rangle \right) = -\varepsilon \nabla \langle p_f \rangle^f + \mu_f \nabla^2 \langle \mathbf{u}_f \rangle$$
$$+\varepsilon \rho_f \mathbf{f} - \frac{\varepsilon \mu_f}{K} \langle \mathbf{u}_f \rangle - \frac{\varepsilon \rho_f c_F}{\sqrt{K}} \left| \langle \mathbf{u}_f \rangle \right| \langle \mathbf{u}_f \rangle. \tag{2.56}$$

The goal of the closure process is to find problems which relate the spatially fluctuating quantities $\tilde{p}$ and $\tilde{\mathbf{u}}_f$ to the coefficients $K$ and $c_F$. The first step is to subtract the volume averaged mass and momentum equations, (2.23) and (2.56), from the general mass and momentum equations, (2.3) and (2.4), which, through application of Eq. (2.29) and (2.43) yield transport equations in terms of the fluctuating quantities. Several length scale arguments permit certain terms in the resulting equations to be neglected. Similar to the way in which the bulk flow drives the local temporal fluctuations in turbulent flows, the bulk flow is identified as the source of local spatial deviations in porous flows. To that end $\tilde{\mathbf{u}}_f$ and $\tilde{p}$ are related to the intrinsic volume-averaged velocity as follows:

$$\tilde{\mathbf{u}}_f = \mathbf{M} \cdot \langle \mathbf{u}_f \rangle^f + \mathbf{v}, \tag{2.57}$$

and

$$\tilde{p} = \mu \mathbf{m} \cdot \langle \mathbf{u}_f \rangle^f + \xi, \tag{2.58}$$

Whitaker [12] demonstrates that $\mathbf{v} = 0$ and $\xi = \text{constant}$ for periodic averaging volumes. Since the constant $\xi$ won't pass the filter integrals, equations (2.57) and (2.58) may be rewritten as

$$\tilde{\mathbf{u}}_f = \mathbf{M} \cdot \langle \mathbf{u}_f \rangle^f, \tag{2.59}$$

and

$$\tilde{p} = \mu \mathbf{m} \cdot \langle \mathbf{u}_f \rangle^f. \tag{2.60}$$

These equations may be back substituted into the transport equations for $\tilde{\mathbf{u}}_f$ and $\tilde{p}$ to yield transport equations in terms of the tensor $\mathbf{M}$ and vector $\mathbf{m}$. A problem may be formulated using the fluid volume in an REV with periodic boundaries to solve for $\mathbf{M}$ and $\mathbf{m}$ fields. This problem is known as a closure model. This closure model could be use to derive relevant coefficients to replace the filters in (2.55), however the form drag is known to vary non-linearly (often quadratically) with velocity, they would acquire an undesirable dependence on the flow velocity. To avoid this, the $\mathbf{M}$ and $\mathbf{m}$ quantities are decomposed into sums of $\mathbf{B}$ and $\mathbf{C}$, and $\mathbf{b}$ and $\mathbf{c}$ quantities respectively and are substituted into the transport equations for the *m* quantities. Thus the initial closure model is split into two; one for the *b* quantities, and one for the *c* quantities. The *b* quantities are defined such that they are purely dependent on the geometry, while the *c* quantities are a function of the geometry and the flow field. The *b* closure problem may be solved, and the results post-processed, to determine the Darcy permeability tensor $\mathbf{K}$ which reduces to a scalar coefficient in the case of isotropic media. Likewise the *c* closure problem may be solved to infer the Forchheimer tensor $\mathbf{F}$, or Forchheimer coefficient in the case of isotropic media.

### 1.3.4 Conservation of Energy

The conservation of energy equation (2.6) must be volume averaged for problems involving energy transport. Unlike the momentum equation, energy transport is assumed to occur in both solid and fluid phases. This derivation will not make the local thermal equilibrium assumption discussed in section 1.1.1, that is, it will *not* be assumed that $\langle T_f \rangle = \langle T_s \rangle = \langle T \rangle$. The solid phase energy equation will be derived first, starting with equation (2.6), where $\langle\ \rangle$ has been applied to each term:

$$\left\langle \rho_s c_{p,s} \frac{dT_s}{dt} \right\rangle + \left\langle \rho_s c_{p,s} \mathbf{u}_s \cdot \nabla T_s \right\rangle = \left\langle \nabla \cdot k_s \nabla T_s \right\rangle - \left\langle \nabla \cdot \mathbf{q}_{\mathrm{r},s} \right\rangle. \tag{2.61}$$

As noted above, the solid matrix is stationary, therefore $\mathbf{u}_s = 0$ , and the second term on the LHS vanishes. Additionally, the density and heat capacity can be assumed constant and can be taken outside the volume averaging brackets; the thermal conductivity will be

dealt with when the diffusion term is analyzed below. Given these simplifications, the solid-phase conservation of energy may be rewritten as

$$\rho_s c_{p,s} \left\langle \frac{dT_s}{dt} \right\rangle = \left\langle \nabla \cdot k_s \nabla T_s \right\rangle - \left\langle \nabla \cdot \mathbf{q}_{\mathrm{r},s} \right\rangle. \tag{2.62}$$

Like the momentum equation, the unsteady term may be reduced by invocation of definition (2.16):

$$\left\langle \frac{\partial T_s}{\partial t} \right\rangle = \frac{1}{V} \int_{V_f} \frac{\partial T_s}{\partial t} dV = \frac{\partial}{\partial t} \left( \frac{1}{V} \int_{V_f} T_s dV \right) = \frac{\partial \left\langle T_s \right\rangle}{\partial t}. \tag{2.63}$$

The diffusion term may be simplified through application of the SAT:

$$\left\langle \nabla \cdot k_s \nabla T_s \right\rangle = \nabla \cdot \left\langle k_s \nabla T_s \right\rangle + \frac{1}{V} \int_{A_{sf}} \mathbf{n}_{sf} \cdot k_s \nabla T_s dA. \tag{2.64}$$

At this point, it is customary to take the solid conductivity, $k_s$, outside the averaging brackets in the first term on the RHS. This is presumably based on the assumption that the solid phase conductivity is constant over the averaging volume (though not necessarily isotropic). For many porous media, such as reticulate foams and fibrous materials this may be a fair approximation, but for the present application, which deals with SVP graphitic foams, this is a terrible approximation; it is now known that graphitic foams exhibit an unusually high bulk thermal conductivity because of highly conductive ligaments. Klett et al. [65] have observed directly that the ligaments in graphitic foam are made up of crystalline graphene sheets, yielding an estimated ligament conductivity of $1300 \ \frac{\mathrm{W}}{\mathrm{m} \cdot \mathrm{K}}$. Considering the fact that the measured bulk thermal conductivity of graphitic foams is in the range of $150 \ \frac{\mathrm{W}}{\mathrm{m} \cdot \mathrm{K}}$ [65, 66], there are very likely large variations in thermal conductivity at the pore level. Lifting the constant-conductivity assumption is outside the scope of this thesis, and is left as an exercise for the reader. Under this assumption, Eq. (2.64) may be simplified to

$$\left\langle \nabla \cdot k_s \nabla T_s \right\rangle = \nabla \cdot k_s \left\langle \nabla T_s \right\rangle + \frac{1}{V} \int_{A_{sf}} \mathbf{n}_{sf} \cdot k_s \nabla T_s dA. \tag{2.65}$$

Furthermore, the SAT may be applied again to yield

$$\left\langle \nabla \cdot k_s \nabla T_s \right\rangle = \nabla \cdot \left( k_s \nabla \left\langle T_s \right\rangle + k_s \frac{1}{V} \int_{A_{sf}} \mathbf{n}_{sf} \cdot T_s dA \right) + \frac{1}{V} \int_{A_{sf}} \mathbf{n}_{sf} \cdot k_s \nabla T_s dA. \tag{2.66}$$

To tackle the first integral the temperature is broken into mean and fluctuating components using Eq. (2.28) and then inserted into Eq. (2.65):

$$T_s = \left\langle T_s \right\rangle^s + \tilde{T}_s, \tag{2.67}$$

$$\frac{1}{V} \int_{A_{sf}} \mathbf{n}_{sf} \cdot T_s dA = \frac{1}{V} \int_{A_{sf}} \mathbf{n}_{sf} \cdot \left\langle T_s \right\rangle dA + \frac{1}{V} \int_{A_{sf}} \mathbf{n}_{sf} \cdot \tilde{T}_s dA. \tag{2.68}$$

Because $\left\langle T_s \right\rangle^s$ is already an average, it can be taken outside the integral term, and the integral reduces to $\frac{1}{V} \int_{A_{sf}} \mathbf{n}_{sf} dA$, which, through application of (2.47), evaluates to 0, and the result may be substituted into (2.66) to give

$$\left\langle \nabla \cdot k_s \nabla T_s \right\rangle = \nabla \cdot \left( k_s \nabla \left\langle T_s \right\rangle + \underbrace{k_s \frac{1}{V} \int_{A_{sf}} \mathbf{n}_{sf} \cdot \tilde{T}_s dA}_{\text{tortuosity}} \right) + \underbrace{\frac{1}{V} \int_{A_{sf}} \mathbf{n}_{sf} \cdot k_s \nabla T_s dA.}_{\text{interfacial heat flux}} \tag{2.69}$$

The volume averaged radiation source term will be analyzed after volume averaging the RTE in section 1.3.5. Presently, equations (2.65) and (2.69) can be combined to write the solid phase volume averaged conservation of energy as follows

$$\rho_s c_{p,s} \frac{\partial \langle T_s \rangle}{\partial t} = \nabla \cdot \left( k_s \nabla \langle T_s \rangle + k_s \frac{1}{V} \int_{A_{sf}} \mathbf{n}_{sf} \cdot \tilde{T}_s dA \right) + \frac{1}{V} \int_{A_{sf}} \mathbf{n}_{sf} \cdot k_s \nabla T_s dA - \langle \nabla \cdot \mathbf{q}_{\mathrm{r},s} \rangle. \tag{2.70}$$

The fluid phase volume averaged energy equation may be written as

$$\left\langle \rho_f c_{p,f} \frac{dT_f}{dt} \right\rangle + \langle \rho_f c_{p,f} \mathbf{u}_f \cdot \nabla T_f \rangle = \langle \nabla \cdot k_f \nabla T_f \rangle - \langle \nabla \cdot \mathbf{q}_{\mathrm{r},f} \rangle. \tag{2.71}$$

Equation (2.71) may be simplified in a similar manner as the solid phase equation; however there are two key differences. First, the present work assumes the fluid phase is optically thin, meaning that it absorbs and emits an insignificant amount of radiation. Consequently the radiation heat flux term may be neglected. Second, the fluid is in motion, so the advection term cannot be ignored. The advection term may be simplified through use of the SAT:

$$\langle \mathbf{u}_f \cdot \nabla T_f \rangle = \langle \nabla \cdot \mathbf{u}_f T_f \rangle = \nabla \cdot \langle \mathbf{u}_f T_f \rangle + \frac{1}{V} \int_{A_{fs}} \mathbf{n}_{fs} \cdot \mathbf{u}_f T_f dA. \tag{2.72}$$

The no-slip condition causes the second term on the RHS to vanish, leaving

$$\langle \mathbf{u}_f \cdot \nabla T_f \rangle = \nabla \cdot \langle \mathbf{u}_f T_f \rangle. \tag{2.73}$$

The velocity and temperature must be decomposed into their spatial averages and deviations to further simplify Eq. (2.73):

$$\begin{aligned} \langle \mathbf{u}_f \cdot \nabla T_f \rangle &= \nabla \cdot \left\langle \langle \mathbf{u}_f \rangle^f \langle T_f \rangle^f + \tilde{\mathbf{u}}_f \langle T_f \rangle^f + \tilde{T}_f \langle \mathbf{u}_f \rangle^f + \tilde{\mathbf{u}}_f \tilde{T}_f \right\rangle \\ &= \nabla \cdot \left( \varepsilon \langle \mathbf{u}_f \rangle^f \langle T_f \rangle^f + \langle \tilde{\mathbf{u}}_f \rangle \langle T_f \rangle^f + \langle \tilde{T}_f \rangle \langle \mathbf{u}_f \rangle^f + \langle \tilde{\mathbf{u}}_f \tilde{T}_f \rangle \right). \end{aligned} \tag{2.74}$$

The second and third terms vanish, as the spatial averages of the deviation terms are zero by definition, leaving

$$\left\langle \mathbf{u}_f \cdot \nabla T_f \right\rangle = \nabla \cdot \left( \varepsilon \left\langle \mathbf{u}_f \right\rangle^f \left\langle T_f \right\rangle^f + \left\langle \tilde{\mathbf{u}}_f \tilde{T}_f \right\rangle \right). \tag{2.75}$$

Substituting Eq. (2.75) and simplifications to the transient and diffusion terms into Eq. (2.71) yields the extrinsic fluid phase volume averaged energy transport equation

$$\begin{aligned} &\rho_f c_{p,f} \frac{d\left\langle T_f \right\rangle}{dt} + \rho_f c_{p,f} \nabla \cdot \left( \varepsilon \left\langle \mathbf{u}_f \right\rangle^f \left\langle T_f \right\rangle^f + \left\langle \tilde{\mathbf{u}}_f \tilde{T}_f \right\rangle \right) = \\ &\nabla \cdot \left( k_f \nabla \left\langle T_f \right\rangle + \underbrace{k_f \frac{1}{V} \int_{A_{fs}} \mathbf{n}_{fs} \cdot \tilde{T}_f dA}_{\text{tortuosity}} \right) + \underbrace{\frac{1}{V} \int_{A_{fs}} \mathbf{n}_{fs} \cdot k_f \nabla T_f dA}_{\text{interfacial heat flux}}. \end{aligned} \tag{2.76}$$

Again, the deviation terms cannot be evaluated directly, and equations (2.70) and (2.76) must be closed.

The interfacial heat flux term appearing in equations (2.70) and (2.76) quantifies the total heat transferred between the solid and fluid phases. These can be modeled heuristically using Newton's law of cooling:

$$\frac{1}{V} \int_{A_{fs}} \mathbf{n}_{fs} \cdot k_s \nabla T_s dA \approx -h_{fs} A_{fs} \left( \left\langle T_s \right\rangle^s - \left\langle T_f \right\rangle^f \right), \tag{2.77}$$

$$\frac{1}{V} \int_{A_{sf}} \mathbf{n}_{sf} \cdot k_f \nabla T_f dA \approx -h_{sf} A_{sf} \left( \left\langle T_f \right\rangle^f - \left\langle T_s \right\rangle^s \right), \tag{2.78}$$

where $h_{fs} = h_{sf}$ and $A_{fs} = A_{sf}$.

The tortuosity term in equations (2.70) and (2.76) contain spatial deviation variables, and must be closed. It is postulated that the source of the temperature deviations is the temperature gradient. The two quantities may be related via the equations

$$\tilde{T}_s = \mathbf{b}_s \cdot \nabla \left\langle T_s \right\rangle^s, \tag{2.79}$$

$$\tilde{T}_f = \mathbf{b}_f \cdot \nabla \left\langle T_f \right\rangle^f , \tag{2.80}$$

where $\mathbf{b}_s$ and $\mathbf{b}_f$ are closure parameters. It should be noted that this merely an extension of the closure model developed for the thermal equilibrium case. A more detailed formulation for the two-equation model is given by Quintard et al. [59].

Within the present model, Eq. (2.79) may be inserted into the tortuosity term in Eq. (2.69) to give

$$k_s \frac{1}{V}\int_{A_{sf}} \mathbf{n}_{sf}\tilde{T}_s dA = k_s \frac{1}{V}\int_{A_{sf}} \mathbf{n}_{sf}\mathbf{b}_s \cdot \nabla \left\langle T_s \right\rangle^s dA = \nabla \left\langle T_s \right\rangle^s \cdot k_s \frac{1}{V}\int_{A_{sf}} \mathbf{n}_{sf}\mathbf{b}_s dA, \tag{2.81}$$

where the gradient of the average temperature is assumed constant over the interfacial area. Inserting equations (2.81) and (2.77) into Eq. (2.70) gives

$$\begin{aligned} &\left(1-\varepsilon\right)\rho_s c_{p,s}\frac{\partial \left\langle T_s \right\rangle^s}{\partial t} = \nabla \cdot \left( \left(1-\varepsilon\right)k_s \mathbf{I} + k_s \frac{1}{V}\int_{A_{sf}} \mathbf{n}_{sf}\mathbf{b}_s dA \right) \cdot \nabla \left\langle T_s \right\rangle^s \\ &-h_{fs}A_{fs}\left( \left\langle T_s \right\rangle^s - \left\langle T_f \right\rangle^f \right) - \left\langle \nabla \cdot \mathbf{q}_{\mathrm{r},s} \right\rangle, \end{aligned} \tag{2.82}$$

where $\mathbf{I}$ is the identity matrix. The terms inside the brackets of the first term on the RHS are often grouped together into a single quantity called the conductivity tensor:

$$\mathbf{K}_{se} = \left(1-\varepsilon\right)k_s \mathbf{I} + k_s \frac{1}{V}\int_{A_{sf}} \mathbf{n}_{sf}\mathbf{b}_s dA. \tag{2.83}$$

In the case of an isotropic medium $\mathbf{K}_{se}$ reduces to a diagonal matrix, which can be represented by a constant coefficient called the *effective thermal conductivity*. In this case Eq. (2.82) reduces to

$$\left(1-\varepsilon\right)\rho_s c_{p,s}\frac{\partial \left\langle T_s \right\rangle^s}{\partial t} = k_{se}\nabla^2 \left\langle T_s \right\rangle^s - h_{fs}A_{fs}\left( \left\langle T_s \right\rangle^s - \left\langle T_f \right\rangle^f \right) - \left\langle \nabla \cdot \mathbf{q}_{\mathrm{r},s} \right\rangle. \tag{2.84}$$

The fluid phase energy equation requires the additional treatment of the product of deviations term, $\left\langle \tilde{\mathbf{u}}_f \tilde{T}_f \right\rangle$. To deal with this, the fluid temperature deviations are modeled using (2.80):

$$\left\langle \tilde{\mathbf{u}}_f \tilde{T}_f \right\rangle = \left\langle \tilde{\mathbf{u}}_f \left( \mathbf{b}_f \cdot \nabla \left\langle T_f \right\rangle^f \right) \right\rangle = \left\langle \tilde{\mathbf{u}}_f \mathbf{b}_f \right\rangle \cdot \nabla \left\langle T_f \right\rangle^f . \tag{2.85}$$

Inserting Eq. (2.85) into (2.76) and making simplifications similar to those of the solid phase equation yields

$$\begin{aligned} &\rho_f c_{p,f} \left[ \varepsilon \frac{d \left\langle T_f \right\rangle^f}{dt} + \left\langle \mathbf{u}_f \right\rangle^f \cdot \nabla \left\langle T_f \right\rangle^f \right] = \nabla \cdot \mathbf{K}_{fe} \cdot \nabla \left\langle T_f \right\rangle^f \\ &- h_{sf} A_{sf} \left( \left\langle T_f \right\rangle^f - \left\langle T_s \right\rangle^s \right), \end{aligned} \tag{2.86}$$

where the conductivity tensor includes the velocity deviation term:

$$\mathbf{K}_{fe} = k_f \varepsilon \mathbf{I} + k_f \frac{1}{V} \int_{A_{fs}} \mathbf{n}_{fs} \mathbf{b}_f \, dA - \rho_f c_{p,f} \left\langle \tilde{\mathbf{u}}_f \mathbf{b}_f \right\rangle. \tag{2.87}$$

When medium is isotropic the conductivity tensor reduces to a diagonal matrix, and Eq. (2.86) may be simplified:

$$\begin{aligned} &\rho_f c_{p,f} \left[ \varepsilon \frac{d \left\langle T_f \right\rangle^f}{dt} + \left\langle \mathbf{u}_f \right\rangle^f \cdot \nabla \left\langle T_f \right\rangle^f \right] = k_{fe} \nabla^2 \left\langle T_f \right\rangle^f \\ &- h_{sf} A_{sf} \left( \left\langle T_f \right\rangle^f - \left\langle T_s \right\rangle^s \right). \end{aligned} \tag{2.88}$$

Thus concludes the volume averaging process of the energy equations.

### 1.3.5 Radiative Transfer Equation

As with the previous transport equations the volume averaging brackets will be applied, this time to Eq. (2.7), and each term will be examined for potential simplifications:

$$\left\langle \hat{\mathbf{s}}\cdot\nabla_{\mathbf{r}} I_i(\mathbf{r},\hat{\mathbf{s}})\right\rangle = -\left\langle \left[\kappa_{d,i}+\sigma_{s,d,i}\right] I_i(\mathbf{r},\hat{\mathbf{s}})\right\rangle + \left\langle n_i^2\kappa_{d,i} I_{b,i}(\mathbf{r})\right\rangle + \left\langle \frac{\sigma_{s,d,i}}{4\pi}\int_{4\pi} I_i(\mathbf{r},\hat{\mathbf{s}}_{\text{in}})\Phi_{d,i}(\hat{\mathbf{s}}_{\text{in}},\hat{\mathbf{s}})\,\mathrm{d}\Omega_{\text{in}}\right\rangle. \tag{2.89}$$

Unlike the previous transport equations, the volume averaged RTE will be derived for the more general case involving a pair of semi-transparent phases, $i$ and $j$. A similar subsequent analysis will be carried out for the case where one phase may be considered opaque. The averaging procedure introduced by Lipiński et. al for two-phase media [61] will be followed here, and the reader is referred to Ref. [62] for an extension to an *n*-component heterogeneous medium. The subscript $d$ has been added to material properties to indicate they are *discrete-scale* properties, and thereby distinguish them from the volume-averaged properties, which will appear upon volume-averaging.

The first term in equation (2.89) may be simplified by way of SAT, where the direction vector $\hat{\mathbf{s}}$ is assumed to be independent of the averaging procedure:

$$\left\langle \hat{\mathbf{s}}\cdot\nabla_{\mathbf{r}} I_i(\mathbf{r},\hat{\mathbf{s}})\right\rangle = \hat{\mathbf{s}}\cdot\left\langle \nabla_{\mathbf{r}} I_i(\mathbf{r},\hat{\mathbf{s}})\right\rangle = \hat{\mathbf{s}}\cdot\left(\nabla_{\mathbf{x}}\left\langle I_i(\mathbf{r},\hat{\mathbf{s}})\right\rangle + \frac{1}{V}\int_{A_{\text{int}}} I_i(\mathbf{r}_{\text{int}},\hat{\mathbf{s}})\hat{\mathbf{n}}_i dA\right). \tag{2.90}$$

The first and second terms on the RHS require little manipulation; the discrete-scale properties are assumed to be constant over the averaging volume, and the volume averaged intensities are recovered:

$$\left\langle \left[\kappa_{d,i}+\sigma_{s,d,i}\right] I_i(\mathbf{r},\hat{\mathbf{s}})\right\rangle = \left[\kappa_{d,i}+\sigma_{s,d,i}\right]\left\langle I_i(\mathbf{r},\hat{\mathbf{s}})\right\rangle, \tag{2.91}$$

$$\left\langle n_i^2\kappa_{d,i} I_{b,i}(\mathbf{r})\right\rangle = n_i^2\kappa_{d,i}\left\langle I_{b,i}(\mathbf{r})\right\rangle. \tag{2.92}$$

The final term on the RHS of Eq. (2.89) (the incoming scattering term) is reduced upon recognizing that the scattering coefficient is constant over the averaging volume. Also, recall that the superficial average definition, Eq. (2.16), necessitates integration over the control volume. Fortunately, the order of integration can be changed, as $\Omega_{\text{in}}$ and $V$ are

independent. If it is further assumed that the phase function, $\Phi_{d,f}(\hat{\mathbf{s}}_{\text{in}},\hat{\mathbf{s}})$, is constant over the volume, Eq. (2.92) may be reduced to:

$$\left\langle \frac{\sigma_{s,d,i}}{4\pi}\int_{4\pi} I_i(\mathbf{r},\hat{\mathbf{s}}_{\text{in}})\Phi_{d,i}(\hat{\mathbf{s}}_{\text{in}},\hat{\mathbf{s}})d\Omega_{\text{in}} \right\rangle = \frac{\sigma_{s,d,i}}{4\pi}\int_{4\pi}\left\langle I_i(\mathbf{r},\hat{\mathbf{s}}_{\text{in}})\right\rangle\Phi_{d,i}(\hat{\mathbf{s}}_{\text{in}},\hat{\mathbf{s}})d\Omega_{\text{in}}. \tag{2.93}$$

Inserting the simplified terms and moving the area integral to the RHS yields

$$\hat{\mathbf{s}}\cdot\nabla_{\mathbf{x}}\left\langle I_i(\mathbf{r},\hat{\mathbf{s}})\right\rangle = -\left[\kappa_{d,i}+\sigma_{s,d,i}\right]\left\langle I_i(\mathbf{r},\hat{\mathbf{s}})\right\rangle + n_i^2\kappa_{d,i}\left\langle I_{b,i}(\mathbf{r})\right\rangle + \frac{\sigma_{s,d,i}}{4\pi}\int_{4\pi}\left\langle I_i(\mathbf{r},\hat{\mathbf{s}}_{\text{in}})\right\rangle\Phi_{d,i}(\hat{\mathbf{s}}_{\text{in}},\hat{\mathbf{s}})\,\mathrm{d}\Omega_{\text{in}} - \frac{1}{V}\int_{A_{\text{int}}} I_i(\mathbf{r}_{\text{int}},\hat{\mathbf{s}})\hat{\mathbf{s}}\cdot\hat{\mathbf{n}}_i dA. \tag{2.94}$$

The final integral on the RHS of Eq. (2.94) is similar to the conduction interface condition in Eq. (2.76). In this case, however, the integral may be obtained through integration of the semi-transparent interface condition, Eq. (2.8):

$$\begin{aligned}&\int_{A_{\text{int}}} I_i(\mathbf{r}_{\text{int}},\hat{\mathbf{s}})\hat{\mathbf{s}}\cdot\hat{\mathbf{n}}_i dA = \\ &\int_{A_{\text{int}}:\hat{\mathbf{s}}\cdot\hat{\mathbf{n}}_i<0}\int_{\Omega_{\text{in}}:\hat{\mathbf{s}}_{\text{in}}\cdot\hat{\mathbf{n}}_i>0}\rho''_{ij}\left(\hat{\mathbf{s}}_{\text{in}},\hat{\mathbf{s}}\right)I_i\left(\mathbf{r}_{\text{int}},\hat{\mathbf{s}}_{\text{in}}\right)\hat{\mathbf{s}}_{\text{in}}\cdot\hat{\mathbf{n}}_i d\Omega_{\text{in}}\hat{\mathbf{s}}\cdot\hat{\mathbf{n}}_i dA \\ &-\int_{A_{\text{int}}:\hat{\mathbf{s}}\cdot\hat{\mathbf{n}}_i<0}\int_{\Omega_{\text{in}}:\hat{\mathbf{s}}_{\text{in}}\cdot\hat{\mathbf{n}}_i<0}\tau''_{ji}\left(\hat{\mathbf{s}}_{\text{in}},\hat{\mathbf{s}}\right)I_j\left(\mathbf{r}_{\text{int}},\hat{\mathbf{s}}_{\text{in}}\right)\hat{\mathbf{s}}_{\text{in}}\cdot\hat{\mathbf{n}}_i d\Omega_{\text{in}}\hat{\mathbf{s}}\cdot\hat{\mathbf{n}}_i dA \\ &+\int_{A_{\text{int}}:\hat{\mathbf{s}}\cdot\hat{\mathbf{n}}_i>0} I_i\left(\mathbf{r}_{\text{int}},\hat{\mathbf{s}}\right)\hat{\mathbf{s}}\cdot\hat{\mathbf{n}}_i dA.\end{aligned} \tag{2.95}$$

To better understand Eq. (2.95) the reader should focus on bounds of the outer integral for each term and refer to Figure 1.2. Also, recall that this term is negated in Eq. (2.94), so positive terms are subtracted from the intensity balance, while negative terms are added. When $\hat{\mathbf{s}}$ is pointing towards phase $i$, $\hat{\mathbf{s}}\cdot\hat{\mathbf{n}}_i<0$, and only the first two integrals are active (non-zero), and Eq. (2.95) represents the sum reflected rays from phase $i$, and the transmitted rays from phase $j$. On the other hand, when $\hat{\mathbf{s}}$ points towards phase $j$,

$\hat{\mathbf{s}}\cdot\hat{\mathbf{n}}_i > 0$, and only the third integral is active. The last integral term has been included to preserve the conservation of energy by subtracting the intensity incident on the interface (had the final integral term not been included, the intensity would be doubled at each boundary element, as the reflected and transmitted portions of rays travelling in the present direction, $\hat{\mathbf{s}}$, are also tallied in other directions).

The integrals in Eq. (2.95) are still difficult to evaluate. It is helpful to recognize that, on the design problem scale, the reflection and transmission phenomena at the phase interfaces serve to scatter radiation. To this end, Eq. (2.95) will be further manipulated to produce effective scattering coefficients and phase functions which can be considered constant over the averaging volume:

$$
\begin{aligned}
&\int_{A_{\text{int}}} I_i(\mathbf{r}_{\text{int}},\hat{\mathbf{s}})\hat{\mathbf{s}}\cdot\hat{\mathbf{n}}_i dA = \\
&-\frac{\sigma_{s,\text{int},ii}}{4\pi}\int_{4\pi}\left\langle I_i(\mathbf{r},\hat{\mathbf{s}}_{\text{in}})\right\rangle \underbrace{\frac{\int_{A_{\text{int}}:\hat{\mathbf{s}}\cdot\hat{\mathbf{n}}_i<0}\rho''_{ij}(\hat{\mathbf{s}}_{\text{in}},\hat{\mathbf{s}})I_i(\mathbf{r}_{\text{int}},\hat{\mathbf{s}}_{\text{in}})\hat{\mathbf{s}}_{\text{in}}\cdot\hat{\mathbf{n}}_i\hat{\mathbf{s}}\cdot\hat{\mathbf{n}}_i dA}{(-4\pi)^{-1}\sigma_{s,\text{int},ii}\left\langle I_i(\mathbf{r},\hat{\mathbf{s}}_{\text{in}})\right\rangle V}}_{\Phi_{\text{int},ii}(\hat{\mathbf{s}}_{\text{in}},\hat{\mathbf{s}})\text{ : evaluate when }\hat{\mathbf{s}}_{\text{in}}\cdot\hat{\mathbf{n}}_i>0\text{; 0 otherwise.}} d\Omega_{\text{in}} \\
&-\frac{\sigma_{s,\text{int},ji}}{4\pi}\int_{4\pi}\left\langle I_j(\mathbf{r},\hat{\mathbf{s}}_{\text{in}})\right\rangle \underbrace{\frac{\int_{A_{\text{int}}:\hat{\mathbf{s}}\cdot\hat{\mathbf{n}}_i<0}\tau''_{ji}(\hat{\mathbf{s}}_{\text{in}},\hat{\mathbf{s}})I_j(\mathbf{r}_{\text{int}},\hat{\mathbf{s}}_{\text{in}})\hat{\mathbf{s}}_{\text{in}}\cdot\hat{\mathbf{n}}_i\hat{\mathbf{s}}\cdot\hat{\mathbf{n}}_i dA}{(4\pi)^{-1}\sigma_{s,\text{int},ji}\left\langle I_j(\mathbf{r},\hat{\mathbf{s}}_{\text{in}})\right\rangle V}}_{\Phi_{\text{int},ji}(\hat{\mathbf{s}}_{\text{in}},\hat{\mathbf{s}})\text{ : evaluate when }\hat{\mathbf{s}}_{\text{in}}\cdot\hat{\mathbf{n}}_i<0\text{; 0 otherwise.}} d\Omega_{\text{in}} \\
&\underbrace{-\frac{\int_{A_{\text{int}}:\hat{\mathbf{s}}\cdot\hat{\mathbf{n}}_i>0}\widehat{\rho}_{ij}(\hat{\mathbf{s}}_{\text{in}})I_i(\mathbf{r}_{\text{int}},\hat{\mathbf{s}}_{\text{in}})\hat{\mathbf{s}}\cdot\hat{\mathbf{n}}_i dA}{\left\langle I_i(\mathbf{x},\hat{\mathbf{s}})\right\rangle V}}_{\sigma_{s,\text{int},ii}} \underbrace{-\frac{\int_{A_{\text{int}}:\hat{\mathbf{s}}\cdot\hat{\mathbf{n}}_i>0}\widehat{\tau}_{ij}(\hat{\mathbf{s}}_{\text{in}})I_i(\mathbf{r}_{\text{int}},\hat{\mathbf{s}}_{\text{in}})\hat{\mathbf{s}}\cdot\hat{\mathbf{n}}_i dA}{\left\langle I_i(\mathbf{x},\hat{\mathbf{s}})\right\rangle V}}_{\sigma_{s,\text{int},ij}}.
\end{aligned}
\tag{2.96}
$$

The labeled terms in Eq. (2.96) are identical to the effective scattering coefficients and phase functions postulated by Lipiński et al. [61]. These definitions are the basis for pore-level analysis, and can be numerically integrated to determine the effective coefficients. Further definitions of summed properties are proposed:

$$\begin{aligned}
&\kappa_i \equiv \kappa_{d,i}, \quad \sigma_{s,ii} \equiv \sigma_{s,d,i} + \sigma_{s,\text{int},ii}, \quad \sigma_{s,ij} \equiv \sigma_{s,\text{int},ij}, \\
&\sigma_{s,i} \equiv \sigma_{s,ii} + \sigma_{s,ij}, \quad \beta_i \equiv \kappa_i + \sigma_{s,i},
\end{aligned} \tag{2.97}$$

$$\begin{aligned}
&\Phi_{ii}\left(\hat{\mathbf{s}}_{\text{in}}, \hat{\mathbf{s}}\right) \equiv \frac{\sigma_{s,d,i}\Phi_{d,i}\left(\hat{\mathbf{s}}_{\text{in}}, \hat{\mathbf{s}}\right) + \sigma_{s,\text{int},ii}\Phi_{d,i}\left(\hat{\mathbf{s}}_{\text{in}}, \hat{\mathbf{s}}\right)}{\sigma_{s,ii}}, \\
&\Phi_{ji}\left(\hat{\mathbf{s}}_{\text{in}}, \hat{\mathbf{s}}\right) \equiv \Phi_{\text{int},ji}\left(\hat{\mathbf{s}}_{\text{in}}, \hat{\mathbf{s}}\right).
\end{aligned} \tag{2.98}$$

Finally, Eqs. (2.96) - (2.98) be inserted into Eq. (2.94) to give the extrinsic, volume averaged RTE, for two semi-transparent phases:

$$\begin{aligned}
&\hat{\mathbf{s}} \cdot \nabla_{\mathbf{x}} \left\langle I_i(\mathbf{x}, \hat{\mathbf{s}}) \right\rangle = -\beta_i \left\langle I_i(\mathbf{x}, \hat{\mathbf{s}}) \right\rangle + n_i^2 \kappa_i \left\langle I_{b,i}(\mathbf{x}) \right\rangle \\
&+ \frac{\sigma_{s,ii}}{4\pi} \int_{4\pi} \left\langle I_i(\mathbf{x}, \hat{\mathbf{s}}_{\text{in}}) \right\rangle \Phi_{ii}(\hat{\mathbf{s}}_{\text{in}}, \hat{\mathbf{s}}) \, \mathrm{d}\Omega_{\text{in}} \\
&+ \frac{\sigma_{s,ij}}{4\pi} \int_{4\pi} \left\langle I_j(\mathbf{x}, \hat{\mathbf{s}}_{\text{in}}) \right\rangle \Phi_{ji}(\hat{\mathbf{s}}_{\text{in}}, \hat{\mathbf{s}}) \, \mathrm{d}\Omega_{\text{in}}.
\end{aligned} \tag{2.99}$$

Behold its majesty. As prescribed, the difficult terms can be restated as effective scattering functions. For this reason, little effort is required to convert an existing radiation heat transfer computer code applicable to homogonous media into a code suitable for volume-averaged radiation calculations.

The design scale boundary conditions of Eq. (2.99) are nearly identical to their discrete-scale counterparts. The intrinsic intensity of a ray emanating from a semi-transparent interface into the $i$ phase is logically identified as the sum of the reflected portion and the transmitted portion. The transmitted portion must be multiplied by the area fraction (equivalent to the volume fraction for a uniform medium) as the remaining portion is transferred to the $j$ phase:

$$\begin{aligned}
&\left\langle I_i\left(\mathbf{x}_w,\hat{\mathbf{s}}\right)\right\rangle^i = \int_{\Omega_{\text{in}}:\hat{\mathbf{s}}_{\text{in}}\cdot\mathbf{n}_i>0} \rho''_{iw}\left(\hat{\mathbf{s}}_{\text{in}},\hat{\mathbf{s}}\right)\left\langle I_i\left(\mathbf{x}_w,\hat{\mathbf{s}}\right)\right\rangle^i \hat{\mathbf{s}}_{\text{in}}\cdot\hat{\mathbf{n}}_i d\Omega_{\text{in}} \\
&-\varepsilon_i \int_{\Omega_{\text{in}}:\hat{\mathbf{s}}_{\text{in}}\cdot\mathbf{n}_i<0} \tau''_{wi}\left(\hat{\mathbf{s}}_{\text{in}},\hat{\mathbf{s}}\right)\left\langle I_w\left(\mathbf{x}_w,\hat{\mathbf{s}}\right)\right\rangle \hat{\mathbf{s}}_{\text{in}}\cdot\hat{\mathbf{n}}_i d\Omega_{\text{in}}, \\
&\hat{\mathbf{s}}\cdot\hat{\mathbf{n}}_i < 0.
\end{aligned} \tag{2.100}$$

Equation (2.18) is readily applied to obtain an expression in terms of extrinsic quantities. Opaque boundaries require a different treatment; the reflection term is the same as in Eq. (2.100), but the second term is replaced by the intensity emitted from a surface:

$$\begin{aligned}
&\left\langle I_i\left(\mathbf{x}_w,\hat{\mathbf{s}}\right)\right\rangle^i = \int_{\Omega_{\text{in}}:\hat{\mathbf{s}}_{\text{in}}\cdot\mathbf{n}_i>0} \rho''_{iw}\left(\hat{\mathbf{s}}_{\text{in}},\hat{\mathbf{s}}\right)\left\langle I_i\left(\mathbf{x}_w,\hat{\mathbf{s}}\right)\right\rangle^i \hat{\mathbf{s}}_{\text{in}}\cdot\hat{\mathbf{n}}_i d\Omega_{\text{in}} \\
&+\varepsilon_i n_i^2 \varepsilon_{wi}\left(\hat{\mathbf{s}}\right) I_{b,w}\left(\mathbf{x}_w\right), \\
&\hat{\mathbf{s}}\cdot\hat{\mathbf{n}}_i < 0.
\end{aligned} \tag{2.101}$$

If one medium can be considered opaque, e.g. in the case of carbon foam submerged in water, Eq. (2.99) must be adjusted, starting from the discrete phase interface condition for a semi-transparent and opaque medium, where the subscripts $i$ and $j$ have been exchanged for the more familiar $f$ and $s$ subscripts to explicitly indicate the fluid and solid phases.

$$\begin{aligned}
&I_f\left(\mathbf{r}_{\text{int}},\hat{\mathbf{s}}\right) = \int_{\Omega_{\text{in}}:\hat{\mathbf{s}}_{\text{in}}\cdot\mathbf{n}_f>0} \rho''_{fs}\left(\hat{\mathbf{s}}_{\text{in}},\hat{\mathbf{s}}\right) I_f\left(\mathbf{r}_{\text{int}},\hat{\mathbf{s}}\right)\hat{\mathbf{s}}_{\text{in}}\cdot\hat{\mathbf{n}}_f d\Omega_{\text{in}} \\
&+n_f^2 \varepsilon_{sf}\left(\hat{\mathbf{s}}\right) I_{b,i}\left(\mathbf{r}_{\text{int}}\right), \\
&\hat{\mathbf{s}}\cdot\hat{\mathbf{n}}_f < 0.
\end{aligned} \tag{2.102}$$

The RTE for the fluid phase is identical to Eq. (2.7) and will not be restated here. The volume averaging procedure is identical to that for two semi-transparent media up until Eq. (2.94). At this point Eq. (2.102) must be integrated over the interfacial surface area, and similar arguments to those above yield effective coefficients and phase function:

$$\sigma_{s,\text{int}} \equiv \frac{\int_{A_{\text{int}}:\hat{\mathbf{s}}\cdot\hat{\mathbf{n}}_i>0} \widehat{\rho}_{fs}\left(\hat{\mathbf{s}}_{\text{in}}\right) I_f\left(\mathbf{r}_{\text{int}},\hat{\mathbf{s}}\right)\hat{\mathbf{s}}\cdot\hat{\mathbf{n}}_f\, dA}{\left\langle I_f\left(\mathbf{x},\hat{\mathbf{s}}\right)\right\rangle V}, \tag{2.103}$$

$$\kappa_{\text{int}} \equiv -\frac{\int_{A_{\text{int}}:\hat{\mathbf{s}}\cdot\hat{\mathbf{n}}_f<0} \varepsilon_{sf}\left(\hat{\mathbf{s}}\right) I_{b,s}\left(\mathbf{r}_{\text{int}}\right)\hat{\mathbf{s}}\cdot\hat{\mathbf{n}}_f\, dA}{\left\langle I_{b,s}\left(\mathbf{x},\hat{\mathbf{s}}\right)\right\rangle V}, \tag{2.104}$$

$$\Phi_{\text{int}}\left(\hat{\mathbf{s}}_{\text{in}},\hat{\mathbf{s}}\right) \equiv \frac{\int_{A_{\text{int}}:\hat{\mathbf{s}}\cdot\hat{\mathbf{n}}_f<0} \rho''_{fs}\left(\hat{\mathbf{s}}_{\text{in}},\hat{\mathbf{s}}\right) I_f\left(\mathbf{r}_{\text{int}},\hat{\mathbf{s}}_{\text{in}}\right)\hat{\mathbf{s}}_{\text{in}}\cdot\hat{\mathbf{n}}_f\hat{\mathbf{s}}\cdot\hat{\mathbf{n}}_f\, dA}{\left(-4\pi\right)^{-1}\sigma_{s,\text{int}}\left\langle I_f(\mathbf{r},\hat{\mathbf{s}}_{\text{in}})\right\rangle V}, \tag{2.105}$$

where the solid matrix is assumed to have gray walls. Aggregate properties may be defined as before:

$$\kappa_f \equiv \kappa_{d,f} + \kappa_{\text{int}}, \quad \sigma_{s,f} \equiv \sigma_{s,d,f} + \sigma_{s,\text{int}}, \quad \beta_f \equiv \kappa_f + \sigma_{s,f}, \tag{2.106}$$

$$\Phi_f\left(\hat{\mathbf{s}}_{\text{in}},\hat{\mathbf{s}}\right) \equiv \frac{\sigma_{s,d,f}\Phi_{d,f}\left(\hat{\mathbf{s}}_{\text{in}},\hat{\mathbf{s}}\right) + \sigma_{s,\text{int}}\Phi_{\text{int}}\left(\hat{\mathbf{s}}_{\text{in}},\hat{\mathbf{s}}\right)}{\sigma_{s,f}}, \tag{2.107}$$

and the extrinsic, volume averaged RTE for the semitransparent phase of a porous media composed of one semitransparent and one opaque phase is given as

$$\begin{aligned}\hat{\mathbf{s}}\cdot\nabla_{\mathbf{x}}\left\langle I_f(\mathbf{x},\hat{\mathbf{s}})\right\rangle &= -\beta_f\left\langle I_f(\mathbf{x},\hat{\mathbf{s}})\right\rangle + n_f^2\kappa_{d,f}\left\langle I_{b,f}(\mathbf{x})\right\rangle + n_f^2\kappa_{\text{int}}\left\langle I_{b,s}(\mathbf{x})\right\rangle \\ &+ \frac{\sigma_{s,f}}{4\pi}\int_{4\pi}\left\langle I_f(\mathbf{x},\hat{\mathbf{s}}_{\text{in}})\right\rangle\Phi_f(\hat{\mathbf{s}}_{\text{in}},\hat{\mathbf{s}})\,\mathrm{d}\Omega_{\text{in}},\end{aligned} \tag{2.108}$$

where the applicable boundary conditions are identical to those given in equations (2.100), and (2.101).

If the $f$ phase can be considered optically thin, e.g. for the case of carbon foam immersed in air, several simplifications to Eq. (2.108) can be made; specifically, terms involving the properties $\kappa_{d,f}$ and $\sigma_{d,f}$ can be neglected:

$$\hat{\mathbf{s}}\cdot\nabla_{\mathbf{x}}\left\langle I_f(\mathbf{x},\hat{\mathbf{s}})\right\rangle = -\beta_{\text{int}}\left\langle I_f(\mathbf{x},\hat{\mathbf{s}})\right\rangle + n_f^2\kappa_{\text{int}}\left\langle I_{b,s}(\mathbf{x})\right\rangle + \frac{\sigma_{s,\text{int}}}{4\pi}\int_{4\pi}\left\langle I_f(\mathbf{x},\hat{\mathbf{s}}_{\text{in}})\right\rangle\Phi_{\text{int}}(\hat{\mathbf{s}}_{\text{in}},\hat{\mathbf{s}})\,\mathrm{d}\Omega_{\text{in}}, \tag{2.109}$$

where the extinction coefficient, $\beta_{\text{int}}$, has been defined as:

$$\beta_{\text{int}} = \kappa_{\text{int}} + \sigma_{s,\text{int}}. \tag{2.110}$$

Also notice that Eq. (2.109) has the same form as the general RTE, Eq. (2.7) when the transient term is neglected; this makes the adaption of existing discretization methods for homogonous media even easier to apply to relevant problems.

Before multi-physics problems involving coupled, radiation-heat transfer can be tackled, the source term in the energy equation must be volume averaged. Modest [34] has derived the radiative heat flux vector from the definition of intensity:

$$\mathbf{q} = \int_{4\pi} I\left(\hat{\mathbf{s}}\right)\hat{\mathbf{s}}d\Omega. \tag{2.111}$$

The next step is to integrate the RTE over all solid angles. For convenience, a modified form of Eq. (2.94) will be used as the starting point, where the gradient term on the LHS has not been expanded, and thus, the area integral on the RHS does not appear:

$$\int_{4\pi}\left\langle\nabla_{\mathbf{r}}\cdot\hat{\mathbf{s}}I_i(\mathbf{r},\hat{\mathbf{s}})\right\rangle d\Omega = -\int_{4\pi}\left[\kappa_{d,i}+\sigma_{s,d,i}\right]\left\langle I_i(\mathbf{r},\hat{\mathbf{s}})\right\rangle d\Omega + \int_{4\pi} n_i^2\kappa_{d,i}\left\langle I_{b,i}(\mathbf{r})\right\rangle d\Omega + \int_{4\pi}\frac{\sigma_{s,d,i}}{4\pi}\int_{4\pi}\left\langle I_i(\mathbf{r},\hat{\mathbf{s}}_{\text{in}})\right\rangle\Phi_{d,i}(\hat{\mathbf{s}}_{\text{in}},\hat{\mathbf{s}})d\Omega_{\text{in}}d\Omega. \tag{2.112}$$

Constant properties and effective properties can immediately be taken outside the integral terms, and the order of integration may be changed in the first term, as $\Omega$ and $V$ are independent. Also, in the third term on the RHS, the in-scattered intensity, $\left\langle I_i(\mathbf{r},\hat{\mathbf{s}}_{\text{in}})\right\rangle$,

is independent of $\Omega$, so it may taken outside the $\Omega$ integral. In addition, $\left\langle I_{b,i}(\mathbf{r})\right\rangle$ is independent of $\Omega$, and may be taken outside the integral, and its definition inserted. These simplifications yield

$$\begin{aligned}\left\langle \nabla\cdot\int_{4\pi}\hat{\mathbf{s}}I_i(\mathbf{r},\hat{\mathbf{s}})d\Omega\right\rangle &= -\left[\kappa_{d,i}+\sigma_{s,d,i}\right]\int_{4\pi}\left\langle I_i(\mathbf{r},\hat{\mathbf{s}})\right\rangle d\Omega \\ &+4n_i^2\kappa_{d,i}\sigma\left\langle T_i\right\rangle^4+\frac{\sigma_{s,d,i}}{4\pi}\int_{4\pi}\left\langle I_i(\mathbf{r},\hat{\mathbf{s}}_{\text{in}})\right\rangle\left[\int_{4\pi}\Phi_{d,i}(\hat{\mathbf{s}}_{\text{in}},\hat{\mathbf{s}})d\Omega\right]d\Omega_{\text{in}}.\end{aligned} \tag{2.113}$$

The first term on the RHS can now be identified as the volume averaged divergence of the radiative heat flux using Eq. (2.111). Furthermore, the definition of the phase function requires [34]:

$$\frac{1}{4\pi}\int_{4\pi}\Phi\left(\hat{\mathbf{s}}_{\text{in}},\hat{\mathbf{s}}\right)d\Omega\equiv 1; \tag{2.114}$$

therefore, the integral in the third term on the RHS may be evaluated directly and Eq. (2.113) simplifies to

$$\begin{aligned}\left\langle \nabla\cdot\mathbf{q}_{\text{r}}\right\rangle &= -\left[\kappa_{d,i}+\sigma_{s,d,i}\right]\int_{4\pi}\left\langle I_i(\mathbf{r},\hat{\mathbf{s}})\right\rangle d\Omega \\ &+4n_i^2\kappa_{d,i}\sigma\left\langle T_i\right\rangle^4+\sigma_{s,d,i}\int_{4\pi}\left\langle I_i(\mathbf{r},\hat{\mathbf{s}}_{\text{in}})\right\rangle d\Omega_{\text{in}}.\end{aligned} \tag{2.115}$$

Finally, the because $\Omega_{\text{in}}$ and $\Omega$ are both dummy variables, the in- and out-scattering terms cancel, and the discrete-phase absorption coefficient may be factored out to yield

$$\left\langle \nabla\cdot\mathbf{q}_{\text{r},i}\right\rangle = \kappa_{d,i}\left[4n_i^2\sigma\left\langle T_i\right\rangle^4-\int_{4\pi}\left\langle I_i(\mathbf{r},\hat{\mathbf{s}})\right\rangle d\Omega\right], \tag{2.116}$$

which is the same as Eq. (2.15), except that the dependency has been shifted from continuous quantities to volume-averaged ones. Another derivation shows that an opaque phase (often the solid phase) energy equation requires a similar radiation term, where the

discrete phase absorption coefficient is replaced by the effective absorption coefficient, $\kappa_{\text{int}}$:

$$\left\langle \nabla \cdot \mathbf{q}_{\text{r},s}\left(\mathbf{r}\right)\right\rangle = \kappa_{\text{int}}\left[4\pi n_f^2 I_{\text{b},s}\left(\mathbf{x}\right) - \int_0^{4\pi} I_f\left(\mathbf{x},\hat{\mathbf{s}}\right)\mathrm{d}\Omega\right]. \tag{2.117}$$

## 1.4 Outline of Upcoming Chapters

The pertinent transport equations have now been volume averaged, and, in the process, equations relating the relevant effective material properties to similar continuous properties have come to light. The rest of this thesis describes how several of these effective properties may be practically identified for the case of SVP carbon foam.

The remainder of this thesis is outlined as follows:

- Chapter 2 is the publication entitled *A New Approach to Digital Generation of Spherical Void Phase Porous Media Microstructures*. It details the approach developed to construct digital samples of porous foam; although the approach is general, the samples of Spherical-Void-Phase (SVP) carbon foam are of particular interest for this thesis.

- Chapter 3 is the publication entitled *Radiative Property Identification of Spherical Void Phase Porous Media*. It describes the identification of the radiation properties using a MC ray-tracing approach and presents the results for a range of mean pore diameters and porosities.

- Chapter 4 summarizes the research contributions, outlines potential future work, and provides some final thoughts on the topic.

## 1.5 References

[1] C. T. DeGroot, A. G. Straatman and L. J. Betchen. Modeling forced convection in finned metal foam heat sinks. *Journal of Electronic Packaging 131(2),* pp. 021001-021001. 2009. . DOI: 10.1115/1.3103934.

[2] A. G. Straatman, N. C. Gallego, Q. Yu, L. Betchen and B. E. Thompson. Forced convection heat transfer and hydraulic losses in graphitic foam. *Journal of Heat Transfer 129(9),* pp. 1237-1245. 2006. . DOI: 10.1115/1.2739621.

[3] G. Flamant. Theoretical and experimental study of radiant heat transfer in a solar fluidized-bed receiver. *AICHE J. 28(4),* pp. 529-535. 1982. Available: http://dx.doi.org/10.1002/aic.690280402. DOI: 10.1002/aic.690280402.

[4] T. Fend, B. Hoffschmidt, R. Pitz-Paal, O. Reutter and P. Rietbrock. Porous materials as open volumetric solar receivers: Experimental determination of thermophysical and heat transfer properties. *Energy 29(5-6),* pp. 823-833. 2004. Available: http://resolver.scholarsportal.info/resolve/03605442/v29i5-6/823_pmaovsotahtp. DOI: 10.1016/S0360-5442(03)00188-9.

[5] T. Fend, R. Pitz-Paal, O. Reutter, J. Bauer and B. Hoffschmidt. Two novel high-porosity materials as volumetric receivers for concentrated solar radiation. *Solar Energy Mater. Solar Cells 84(1–4),* pp. 291-304. 2004. . DOI: http://dx.doi.org/10.1016/j.solmat.2004.01.039.

[6] R. Pitz-Paal, B. Hoffschmidt, M. Böhmer and M. Becker. Experimental and numerical evaluation of the performance and flow stability of different types of open volumetric absorbers under non-homogeneous irradiation. *Solar Energy 60(3–4),* pp. 135-150. 1997. . DOI: http://dx.doi.org/10.1016/S0038-092X(97)00007-8.

[7] M. Becker, T. Fend, B. Hoffschmidt, R. Pitz-Paal, O. Reutter, V. Stamatov, M. Steven and D. Trimis. Theoretical and numerical investigation of flow stability in porous materials applied as volumetric solar receivers. *Solar Energy 80(10),* pp. 1241-1248. 2006. . DOI: http://dx.doi.org/10.1016/j.solener.2005.11.006.

[8] Z. Wu, C. Caliot, G. Flamant and Z. Wang. Coupled radiation and flow modeling in ceramic foam volumetric solar air receivers. *Solar Energy 85(9),* pp. 2374-2385. 2011. . DOI: http://dx.doi.org/10.1016/j.solener.2011.06.030.

[9] I. Hischier, D. Hess, W. Lipiński, M. Modest and A. Steinfeld. Heat transfer analysis of a novel pressurized air receiver for concentrated solar power via combined cycles. *Journal of Thermal Science and Engineering Applications 1(4),* pp. 041002. 2009.

[10] P. Dhiman, N. S. Thakur and S. R. Chauhan. Thermal and thermohydraulic performance of counter and parallel flow packed bed solar air heaters. *Renewable Energy 46(0),* pp. 259-268. 2012. . DOI: http://dx.doi.org.proxy1.lib.uwo.ca/10.1016/j.renene.2012.03.032.

[11] S. Singh and P. Dhiman. Thermal and thermohydraulic performance evaluation of a novel type double pass packed bed solar air heater under external recycle using an analytical and \RSM\ (response surface methodology) combined approach. *Energy 72(0),* pp. 344. 2014. Available: http://www.sciencedirect.com/science/article/pii/S0360544214006100. DOI: http://dx.doi.org/10.1016/j.energy.2014.05.044".

[12] S. Whitaker. The forchheimer equation: A theoretical development. *Transp Porous Med 25(1),* pp. 27-61. 1996. Available: http://resolver.scholarsportal.info/resolve/01693913/v25i0001/27_tfeatd. DOI: 10.1007/BF00141261.

[13] N. C. Gallego and J. W. Klett. Carbon foams for thermal management. *Carbon 41(7),* pp. 1461-1466. 2003. Available: http://resolver.scholarsportal.info/resolve/00086223/v41i0007/1461_cfftm. DOI: 10.1016/S0008-6223(03)00091-5.

[14] Y. Nakashima and Y. Watanabe. Estimate of transport properties of porous media by microfocus X-ray computed tomography and random walk simulation. *Water Resour. Res. 38(12),* pp. 8-1--8-12. 2002. Available: http://dx.doi.org/10.1029/2001WR000937. DOI: 10.1029/2001WR000937.

[15] B. Maruyama, J. E. Spowart, D. J. Hooper, H. M. Mullens, A. M. Druma, C. Druma and M. K. Alam. A new technique for obtaining three-dimensional structures in pitch-based carbon foams. *Scr. Mater. 54(9),* pp. 1709-1713. 2006. . DOI: http://dx.doi.org/10.1016/j.scriptamat.2005.12.060.

[16] M. S. Anghelescu. Thermal and mechanical analysis of carbon foam. *ProQuest Dissertations and Theses* 2009. Available: http://search.proquest.com/docview/304963894?accountid=15115.

[17] S. Haussener, P. Coray, W. Lipinski, P. Wyss and A. Steinfeld. Tomography-based heat and mass transfer characterization of reticulate porous ceramics for high-temperature processing. *J. Heat Transfer 132(2),* pp. 023305. 2010. Available: http://dx.doi.org/10.1115/1.4000226. DOI: 10.1115/1.4000226.

[18] S. Haussener, I. Jerjen, A. Steinfeld and P. Wyss. Tomography-based determination of effective transport properties for reacting porous media. *Journal of Heat Transfer 134(1),* pp. 012601-012601. 2011. . DOI: 10.1115/1.4004842.

[19] S. Haussener, W. Lipinski, P. Wyss and A. Steinfeld. Tomography-based analysis of radiative transfer in reacting packed beds undergoing a solid-gas thermochemical transformation. *J. Heat Transfer 132(6),* pp. 061201. 2010. Available: http://dx.doi.org/10.1115/1.4000749. DOI: 10.1115/1.4000749.

[20] E. Zermatten, S. Haussener, M. Schneebeli and A. Steinfeld. Tomography-based determination of permeability and Dupuit–Forchheimer coefficient of characteristic snow samples. *J. Glaciol. 57(205),* pp. 811-816. 2011-10-01T00:00:00. Available: http://www.ingentaconnect.com/content/igsoc/jog/2011/00000057/00000205/art00004. DOI: doi:10.3189/002214311798043799".

[21] Q. Yu, B. E. Thompson and A. G. Straatman. A unit cube-based model for heat transfer and fluid flow in porous carbon foam. *Journal of Heat Transfer 128(4),* pp. 352-360. 2006.

[22] K. Boomsma and D. Poulikakos. On the effective thermal conductivity of a three-dimensionally structured fluid-saturated metal foam. *Int. J. Heat Mass Transfer 44(4)*, pp. 827-836. 2001. . DOI: http://dx.doi.org/10.1016/S0017-9310(00)00123-X.

[23] Z. Dai, K. Nawaz, Y. G. Park, J. Bock and A. M. Jacobi. Correcting and extending the Boomsma–Poulikakos effective thermal conductivity model for three-dimensional, fluid-saturated metal foams. *Int. Commun. Heat Mass Transfer 37(6)*, pp. 575-580. 2010. . DOI: http://dx.doi.org/10.1016/j.icheatmasstransfer.2010.01.015.

[24] P. Kumar, J. Hugo, F. Topin and J. Vicente. Influence of pore and strut shape on open cell metal foam bulk properties. *AIP Conference Proceedings 1453(1)*, pp. 243-248. 2012. Available: http://search.ebscohost.com/login.aspx?direct=true&db=a9h&AN=75230839&site=ehost-live. DOI: 10.1063/1.4711183.

[25] S. Sihn and A. K. Roy. Modeling and prediction of bulk properties of open-cell carbon foam. *J. Mech. Phys. Solids 52(1)*, pp. 167-191. 2004. . DOI: http://dx.doi.org/10.1016/S0022-5096(03)00072-3.

[26] K. C. Leong and H. Y. Li. Theoretical study of the effective thermal conductivity of graphite foam based on a unit cell model. *Int. J. Heat Mass Transfer 54(25–26)*, pp. 5491-5496. 2011. . DOI: http://dx.doi.org/10.1016/j.ijheatmasstransfer.2011.07.042.

[27] M. Kırca, A. Gül, E. Ekinci, F. Yardım and A. Mugan. Computational modeling of micro-cellular carbon foams. *Finite Elements Anal. Des. 44(1–2)*, pp. 45-52. 2007. . DOI: http://dx.doi.org/10.1016/j.finel.2007.08.008.

[28] M. Wang and N. Pan. Modeling and prediction of the effective thermal conductivity of random open-cell porous foams. *Int. J. Heat Mass Transfer 51(5–6)*, pp. 1325-1331. 2008. . DOI: http://dx.doi.org/10.1016/j.ijheatmasstransfer.2007.11.031.

[29] C. C. Chueh, A. Bertei, J. G. Pharoah and C. Nicolella. Effective conductivity in random porous media with convex and non-convex porosity. *Int. J. Heat Mass Transfer 71(0)*, pp. 183-188. 2014. Available:

http://www.sciencedirect.com/science/article/pii/S0017931013010855. DOI: http://dx.doi.org/10.1016/j.ijheatmasstransfer.2013.12.041.

[30] W. M. VISSCHER and M. BOLSTERLI. Random packing of equal and unequal spheres in two and three dimensions. *Nature 239(5374)*, pp. 504-507. 1972. Available: http://dx.doi.org/10.1038/239504a0.

[31] L. Betchen, A. G. Straatman and B. E. Thompson. A nonequilibrium finite-volume model for conjugate fluid/porous/solid domains. *Numerical Heat Transfer, Part A: Applications 49(6)*, pp. 543-565. 2006. Available: http://resolver.scholarsportal.info/resolve/10407782/v49i0006/543_anfmfcfd. DOI: 10.1080/10407780500430967.

[32] F. P. Incropera. *Fundamentals of Heat and Mass Transfer* 2011.

[33] R. Siegel and J. R. Howell. Thermal radiation heat transfer. *NASA STI/Recon Technical Report A 93*pp. 17522. 1992.

[34] M. F. Modest. *Radiative Heat Transfer* 2013.

[35] H. C. Hottel and E. S. Cohen. Radiant heat exchange in a gas-filled enclosure: Allowance for nonuniformity of gas temperature. *AICHE J. 4(1)*, pp. 3-14. 1958. Available: http://dx.doi.org/10.1002/aic.690040103. DOI: 10.1002/aic.690040103.

[36] M. E. Larsen. The exchange factor method: AN alternative zonal formulation for analysis of radiating enclosures containing participating media. 1983.

[37] W. W. Yuen. The multiple absorption coefficient zonal method (MACZM), an efficient computational approach for the analysis of radiative heat transfer in multidimensional inhomogeneous nongray media. *Numer Heat Transfer Part B Fundam 49(2)*, pp. 89-103. 2006.

[38] J. Jeans. The equations of radiative transfer of energy. *Monthly Notices of the Royal Astronomical Society 78(1)*, pp. 28-36. 1917.

[39] S. Chandrasekhar. *Radiative Transfer* 1960.

[40] M. Sakami, A. Charette and V. Le Dez. Application of the discrete ordinates method to combined conductive and radiative heat transfer in a two-dimensional complex geometry. *Journal of Quantitative Spectroscopy and Radiative Transfer 56(4),* pp. 517-533. 1996. . DOI: http://dx.doi.org/10.1016/0022-4073(96)00082-9.

[41] R. Koch, W. Krebs, S. Wittig and R. Viskanta. Discrete ordinates quadrature schemes for multidimensional radiative transfer. *Journal of Quantitative Spectroscopy and Radiative Transfer 53(4),* pp. 353-372. 1995. . DOI: http://dx.doi.org/10.1016/0022-4073(95)90012-8.

[42] R. Koch and R. Becker. Evaluation of quadrature schemes for the discrete ordinates method. *Journal of Quantitative Spectroscopy and Radiative Transfer 84(4),* pp. 423-435. 2004. . DOI: http://dx.doi.org/10.1016/S0022-4073(03)00260-7.

[43] I. Malico and J. C. F. Pereira. Numerical study on the influence of radiative properties in porous media combustion. *Journal of Heat Transfer 123(5),* pp. 951-957. 2001. . DOI: 10.1115/1.1389059.

[44] G. D. Raithby. DISCUSSION OF THE FINITE-VOLUME METHOD FOR RADIATION, AND ITS APPLICATION USING 3D UNSTRUCTURED MESHES. *Numer Heat Transfer Part B Fundam 35(4),* pp. 389-405. 1999. Available: http://resolver.scholarsportal.info/resolve/10407790/v35i0004/389_dotfmfiau3um. DOI: 10.1080/104077999275802.

[45] G. Raithby and E. Chui. A finite-volume method for predicting a radiant heat transfer in enclosures with participating media. *Journal of Heat Transfer 112(2),* pp. 415-423. 1990.

[46] S. Patankar. *Numerical Heat Transfer and Fluid Flow* 1980.

[47] K. Slimi, L. Zili-Ghedira, S. B. Nasrallah and A. A. Mohamad. A transient study of coupled natural convection and radiation in a porous vertical channel using the finite-volume method. *Numerical Heat Transfer: Part A -- Applications 45(5),* pp. 451-478.

2004. Available: http://search.ebscohost.com/login.aspx?direct=true&db=a9h&AN=12751155&site=ehost-live. DOI: 10.1080/10407780490269003.

[48] G. Kamel, B. M. Naceur, M. Rachid and S. Rachid. Formulation and testing of the FTn finite volume method for radiation in 3-D complex inhomogeneous participating media. *Journal of Quantitative Spectroscopy and Radiative Transfer 98(3)*, pp. 425-445. 2006. . DOI: http://dx.doi.org/10.1016/j.jqsrt.2005.07.001.

[49] P. J. Coelho, J. M. GonÇalves, M. G. Carvalho and D. N. Trivic. Modelling of radiative heat transfer in enclosures with obstacles. *Int. J. Heat Mass Transfer 41(4–5)*, pp. 745-756. 1998. . DOI: http://dx.doi.org/10.1016/S0017-9310(97)00158-0.

[50] J. Howell. The monte carlo method in radiative heat transfer. *Journal of Heat Transfer 120(3),* pp. 547-560. 1998.

[51] J. R. Howell and M. Perlmutter. Monte carlo solution of thermal transfer through radiant media between gray walls. *Journal of Heat Transfer 86(1),* pp. 116-122. 1964. . DOI: 10.1115/1.3687044.

[52] S. Mey, C. Caliot, G. Flamant, A. Kribus and Y. Gray. Optimization of high temperature SiC volumetric solar absorber. *Energy Procedia 49*pp. 478-487. 2014.

[53] C. Y. Zhao, T. J. Lu and H. P. Hodson. Thermal radiation in ultralight metal foams with open cells. *Int. J. Heat Mass Transfer 47(14â€“16),* pp. 2927. 2004. Available: http://www.sciencedirect.com/science/article/pii/S0017931004000912. DOI: http://dx.doi.org/10.1016/j.ijheatmasstransfer.2004.03.006".

[54] S. Whitaker. Diffusion and dispersion in porous media. *AICHE J. 13(3),* pp. 420-427. 1967. Available: http://dx.doi.org/10.1002/aic.690130308. DOI: 10.1002/aic.690130308.

[55] J. C. Slattery. Flow of viscoelastic fluids through porous media. *AICHE J. 13(6),* pp. 1066-1071. 1967. Available: http://dx.doi.org/10.1002/aic.690130606. DOI: 10.1002/aic.690130606.

[56] F. E. Teruel and Rizwan-uddin. Characterization of a porous medium employing numerical tools: Permeability and pressure-drop from darcy to turbulence. *Int. J. Heat Mass Transfer 52(25â€“26),* pp. 5878. 2009. Available: http://www.sciencedirect.com/science/article/pii/S0017931009004505. DOI: http://dx.doi.org/10.1016/j.ijheatmasstransfer.2009.07.017".

[57] S. Whitaker. Simultaneous heat, mass, and momentum transfer in porous media: A theory of drying. *Advances in Heat Transfer 13*pp. 119-203. 1977.

[58] M. Quintard and S. Whitaker. *Theoretical Analysis of Transport in Porous Media* 2000.

[59] M. Quintard, M. Kaviany and S. Whitaker. Two-medium treatment of heat transfer in porous media: Numerical results for effective properties. *Adv. Water Resour. 20(2–3),* pp. 77-94. 1997. . DOI: http://dx.doi.org/10.1016/S0309-1708(96)00024-3.

[60] B. Zeghondy, E. Iacona and J. Taine. Determination of the anisotropic radiative properties of a porous material by radiative distribution function identification (RDFI). *Int. J. Heat Mass Transfer 49(17–18),* pp. 2810-2819. 2006. . DOI: http://dx.doi.org.proxy1.lib.uwo.ca/10.1016/j.ijheatmasstransfer.2006.02.034.

[61] W. Lipiński, J. Petrasch and S. Haussener. Application of the spatial averaging theorem to radiative heat transfer in two-phase media. *Journal of Quantitative Spectroscopy and Radiative Transfer 111(1),* pp. 253-258. 2010. Available: http://resolver.scholarsportal.info/resolve/00224073/v111i0001/253_aotsatrhtitm. DOI: 10.1016/j.jqsrt.2009.08.001.

[62] W. Lipiński, D. Keene, S. Haussener and J. Petrasch. Continuum radiative heat transfer modeling in media consisting of optically distinct components in the limit of geometrical optics. *Journal of Quantitative Spectroscopy and Radiative Transfer 111(16),* pp. 2474-2480. 2010. Available: http://resolver.scholarsportal.info/resolve/00224073/v111i0016/2474_crhtmiitlogo. DOI: 10.1016/j.jqsrt.2010.06.022.

[63] H. Brinkman. A calculation of the viscous force exerted by a flowing fluid on a dense swarm of particles. *Applied Scientific Research 1(1),* pp. 27-34. 1949.

[64] K. Vafai and C. Tien. Boundary and inertia effects on flow and heat transfer in porous media. *Int. J. Heat Mass Transfer 24(2),* pp. 195-203. 1981.

[65] J. W. Klett, A. D. McMillan, N. C. Gallego and C. A. Walls. The role of structure on the thermal properties of graphitic foams. *J. Mater. Sci. 39(11),* pp. 3659-3676. 2004. Available: http://resolver.scholarsportal.info/resolve/00222461/v39i0011/3659_trosottpogf. DOI: 10.1023/B:JMSC.0000030719.80262.f8.

[66] J. Klett, R. Hardy, E. Romine, C. Walls and T. Burchell. High-thermal-conductivity, mesophase-pitch-derived carbon foams: Effect of precursor on structure and properties. *Carbon 38(7),* pp. 953-973. 2000. . DOI: http://dx.doi.org/10.1016/S0008-6223(99)00190-6.

# Chapter 2

# 2 A New Approach to Digital Generation of Porous Media

This work describes a novel approach for obtaining digital samples of porous media based on a statistical knowledge of the microstructure of interest. The present formulation introduces a contact law based on bubble physics that is capable of handling interferences among spherical primitives of different diameter placed in a representative elemental volume, while the volume is compressed to yield a target porosity. The result is a statistically accurate mathematical model of a permeable, spherical-void-phase porous material that has the added feature of being spatially periodic in all principal directions. To validate the approach, digital samples of spherical-void-phase carbon foam were generated and discretized for use in hydraulic and thermal Computational Fluid Dynamics simulations. Relevant transport properties were computed from the simulation results, and compared to similar data found in the literature.

## 2.1 Introduction

Porous materials play an important role in many applications including heat pipes, heat sinks, automotive cooling devices and solar collectors. Any porous microstructure may be characterized by the statistical geometric properties: mean pore diameter, ligament length, surface area per unit volume, void shape, and geometric order, each of which *might* be correlated with changes in bulk material properties. The microstructural properties also affect exchanges that occur between fluid and solid phases in the case of flow through a permeable porous material, or in the case of external exposure to incident radiation. This has inspired many researchers to study the effects of pore structure variation on bulk material properties by developing representative, or idealized, geometric models. Such models permit analysis of properties and exchanges at the pore level, which can then be used to develop accurate mathematical models at the porous-continuum or volume-averaged level, which is what is used in most engineering analyses to deal with porous materials. In this paper, our interest is to develop a geometric model for a spherical void phase foam (carbon foam) that can be used to study exchanges that occur in a highly concentrated solar collector. Our interest in graphitic foam is that it is

highly permeable, highly conductive and it has a high surface area to volume ratio. While pore-level geometric models do exist for spherical void phase materials, no current model is suitable to yield the material properties and exchanges, while preserving the random nature of the structure, which is required for consideration of radiation effects.

Currently, there are three main approaches to obtain bulk material properties, given the porous material of interest. First, experiments can be conducted to empirically determine the desired properties. While this method is quite useful for determining properties that can be used in engineering calculations, it can difficult for researchers to understand the influence of the microstructure on the determined properties. Moreover, because experiments can only be performed on physical samples, the range of microstructures that can be studied is limited by current production capabilities.

The second method is to conduct Computer Tomography (CT) scans of a representative sample of the microstructure, thereby obtaining a digital representation of the structure. The raw data from the scan is post-processed to obtain a Computer-Aided Design (CAD) model. This model can then be used in computer simulations to determine the desired transport properties. Researchers including Haussener et al. [1], Maruyama et al. [2], and Anghelescu [3] have used this approach with some success. Unlike the experimental approach, this method allows researchers to visualize transport quantities and gradients throughout the pore level domain. However, the cost and accessibility of CT scanning equipment as well as the limitation of porous media production capabilities leaves more to be desired.

The final method is to generate a large number of small primitive objects (primitives) within a finite domain, where the dimensions of the primitives are decided based on statistical data describing the microstructure of interest. The interference of these primitives gives rise to the interesting features present in the porous domain. A finite volume filled with interfering primitives is thought to be an accurate representation of the desired microstructure. These digital domains can then be used in small-scale simulations to predict effective material properties. This method is unique in the fact that it does not require any physical representation of the domain, but only a statistical knowledge of the

micro-structural features. Because this method deals with idealized representations of porous media, it is important to judge the relevance of all microstructural features to the bulk property of interest. Identifying which microstructural features whose variation does *not* influence a bulk property may allow a much simpler geometric model to be used. A first attempt by Yu et al. [4] constitutes the use of a simple primitive: the Boolean subtraction of a sphere from a cube (where the centroids of the sphere and cube are coincident). This primitive is stacked along all major axis to obtain a uniform structure of interconnected pores. This so-called unit-cube model is easy to generate and analyze digitally, however it does not capture the effect of bubble size variation, and it exhibits uncharacteristic properties due to the axis alignment of the bubbles. When used for studying trends in convective/conductive heat transfer and fluid flow, the unit cube model is sufficient, as predictions of permeability, inertial drag coefficients, and Nusselt number correlations were shown to be reasonable when the flow direction was oriented 45° from all principle planes [4, 5]. Kumar et al. [6] performed Computational Fluid Dynamics (CFD) analyses involving the periodic tetrakaidecahedron structure (Kelvin cell) relevant to open-cell foams. The CFD results were compared with experimental results obtained using a uniform microstructure, which yielded excellent agreement. Leong & Li [7] determined the effective thermal conductivity of a unit cell which may be described as the Boolean subtraction of eight spheres from a cubic shell, where the spheres are centered on the vertices of the cube. James et al. [8] presented a novel approach for the generation of spherical-void phase (SVP) porous media wherein bubble diameters and interferences are chosen based on known probability distribution functions. That said, the method presented in [8] has some drawbacks, including the unrealistic assumption that the interference between two bubbles in contact is independent of their radii, and the random deletion of bubbles to obtain the desired porosity. In another work by Kırca et al. [9], carbon foam was modeled by selecting random points within a cubic domain as the sphere centers, and calculating the radii of the bubbles based on the desired porosity and the average bubble diameter. The method also suffered from the fact that bubble interferences were not determined. Wang & Pan [10] have proposed a random-generation growth method, wherein representations of open-cell foams are generated by randomly placing points in a 3D domain and stochastically linking neighbouring nodes. Finally, in

a recent publication by Chueh et. al [11], SVP was modeled by packing spheres into a periodic domain using the drop-and-roll method introduced by Visscher and Bolsterli [12]. This method relies on the assumption that bubble interferences can be prescribed using a constant contact angle, and periodicity is only enforced in two directions.

The primary motivation for developing the present method is to obtain digital samples of SVP carbon foam suitable for prediction of radiation transport properties. The ordered nature of the unit-cube model make it a poor candidate for ray-tracing methods, such as that presented by Tancrez & Taine [13], so more accurate representations of SVP porous media are sought. In this work, the approach taken is similar to previous efforts, however in the Representative Elemental Volumes (REVs) produced using the current method, the interferences between features are governed by physically-based force-displacement relationship, and the REVs have the distinct advantage of being fully spatially periodic. The resulting models are then shown to produce the correct trends for pressure drop and convective heat transfer, thereby satisfying the necessary condition that fluid-solid interactions within the REV are properly predicted. Combined with the advantages of including variable pore size and preserving the random nature of the structure, the present modeling approach is considered most viable for studies on incident radiation.

## 2.2 Formulation

In the current approach, a 3D porous structure is generated from aggregate statistical data. For example, an isotropic SVP porous medium may have a statistical data set including an average bubble diameter and the standard deviation of the bubble diameters.

Once these data are determined, the method can be executed with the following steps:

1) Select an Initial Volume (IV) shape and size. The IV should be large enough to completely envelop all of the geometric primitives without any of the primitives coming into contact with each other.

2) Generate primitives. Choose the shape and dimensions of each primitive using a probabilistic model that reflects the statistical data. Then attempt to randomly locate each primitive within the IV, optionally choosing an orientation based on statistical

data. If a primitive interferes with an already placed primitive, randomly select new locations and orientations until it does not interfere with other primitives. If a primitive cannot be placed after a large number of attempts, this may indicate that the IV is too small, in which case the algorithm should be restarted with a larger IV. The stopping criterion is at the discretion of the user. A simple approach is to stop after a pre-determined number of primitives have been placed.

3) Using a Discrete Element Method (DEM) code, incrementally compress the IV over a sequence of time-steps. During each time-step, the domain boundaries are moved closer together. If the boundaries are chosen to be rigid walls, the primitives in contact with the boundaries will be forced inward, and come into contact with other primitives. Reaction forces (or separating forces) between primitives in contact are calculated using an appropriate force-displacement relationship, also known as a contact law. Eventually the primitives will reach a jammed state, where every primitive is locked in place. After the jammed state has been reached, further compression steps require ever-increasing forces to be applied to the walls, while the penetrations between primitives in contact are also increased. The stopping criterion is at the discretion of the user. A simple criterion would be to stop when the desired porosity is reached.

   While rigid walls may be easy to implement, but the resulting domains will not be periodic; a desirable trait for subsequent prediction of volume averaged properties. To obtain periodic domains, the rigid walls must be replaced with periodic boundary conditions. Periodic boundary conditions can be implemented by ‘wrapping’ the coordinates of all the primitives inside the domain, a concept illustrated in Figure 1.1.

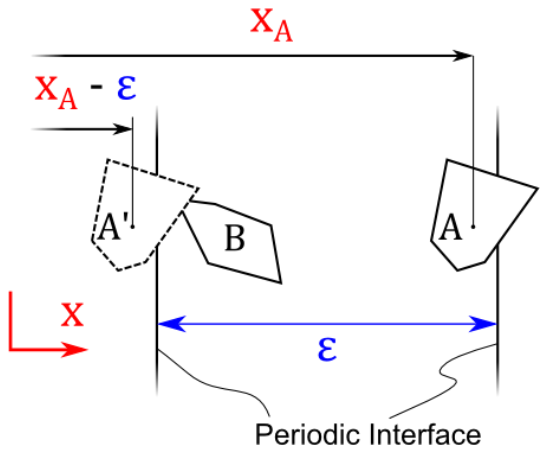


Figure 2.1 Periodic interface implementation showing two original primitives, $A$ and $B$, as well as one wrapped primitive, $A'$. The distance between the two periodic faces is $\varepsilon$.

In Figure 2.1, Primitive $A$ is wrapped across a flat periodic interface in the x-direction to form primitive $A'$. $A'$ acts as a proxy for $A$; the collision between $A'$ and $B$ is treated as a collision between $A$ and $B$. In contrast to a rigid wall the periodic boundary does not apply a direct force to the primitives in contact. If the domain is compressed by some distance $\Delta\varepsilon$, the co-ordinate of $A'$ will increase by the same amount. This in turn will increase the penetration of the contact between $A'$ and $B$. As a consequence, the separation force between $A$ and $B$ will also increase.

4) Extract the dimensions, locations, and (optionally) orientations of the primitives, and use the data to generate the CAD model.

## 2.3 Contact Law

Because the current method makes use of the DEM, the interaction between primitives (e.g. particles, fibers, bubbles) in contact is dependent on a known contact law. A contact law may be defined based on the materials of the two primitives in contact as well as their geometries. In preparation for the generation of SVP porous media samples, a contact law governing the interaction of bubbles will be derived.

Carbon foam may be manufactured by bubbling molten tar pitch [14]; during the packing phase initially sparse bubbles expand, and are forced into contact with one another as the domain is saturated. When the domain is packed, the pitch is cooled and the bubbles are

frozen in place. It is of interest to model the packing phase in a DEM simulation, so a contact law governing the interaction of bubbles will be derived.

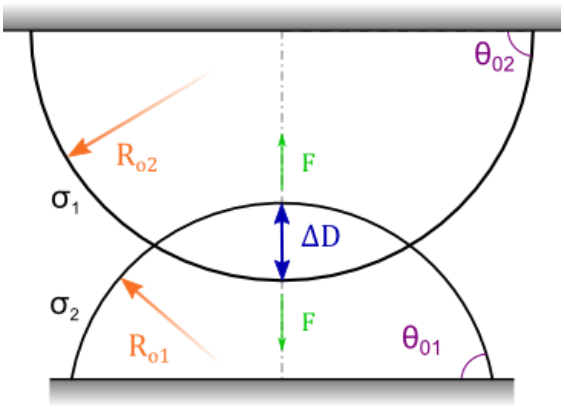


Figure 2.2 Axis-symmetric opposing bubbles affixed to parallel surfaces. The overlapping region is called the interaction zone.

The setup in Figure 2.2 has been analyzed by Chan et al. [15] who derived the general force-displacement relationship:

$$\Delta D \cong \frac{F}{4\pi\sigma_1}\left\{\ln\left(\frac{F\bar{R}_o}{8\pi\bar{\sigma}R_{o1}^2}\right)+2B(\theta_{o1})\right\}+\frac{F}{4\pi\sigma_2}\left\{\ln\left(\frac{F\bar{R}_o}{8\pi\bar{\sigma}R_{o2}^2}\right)+2B(\theta_{o2})\right\}-\frac{F}{2\pi\bar{\sigma}} \tag{3.1}$$

$$\frac{1}{\bar{R}_o}\equiv\frac{1}{2}\left(\frac{1}{R_{o1}}+\frac{1}{R_{o2}}\right) \tag{3.2}$$

$$\frac{1}{\bar{\sigma}}=\frac{1}{2}\left(\frac{1}{\sigma_1}+\frac{1}{\sigma_2}\right) \tag{3.3}$$

where the parameters in equations (3.1) - (3.3) are defined in Table 2.1.

Table 2.1 Descriptions of terms in Eq. (3.1)

| | |
|---|---|
| $\Delta D$ | Interference (penetration) between interacting bubbles |
| $F$ | Normal force acting along the line of contact between the two bubbles |
| $\sigma_1, \sigma_2$ | Surface tension of the fluid surrounding each bubble |
| $R_{o1}, R_{o2}$ | Undeformed radius of each bubble |
| $\theta_{o1}, \theta_{o2}$ | Contact angle of each undeformed bubble |

Two separate forms of the function $B(\theta)$ were proposed: in the first case the contact angle $\theta$ was assumed to remain constant as the bubbles are depressed. In the second case, the contact line of each bubble with the wall is assumed fixed, while $\theta$ is allowed to vary during the deformation. Only the first case is relevant to the present application, where $B(\theta)$ has the form:

$$B(\theta) = 1 + \frac{1}{2}\ln\left(\frac{1+\cos\theta}{1-\cos\theta}\right) - \left(\frac{1}{2+\cos\theta}\right) \tag{3.4}$$

In order to apply Eq. (3.1) to bubbles in SVP porous media, a crucial observation must be made: deformation of a bubble having a constant wall contact angle of $90^o$ is identical to the case where a spherical bubble suspended in a liquid is opposed on either side by bubbles of equal radii. In other words, if a constant contact angle of $90^o$ is assumed for either bubble in Figure 2.2, the solid wall behaves as a symmetry plane. Building on this realization, it can be concluded that Eq. (3.1) also applies to the bubbles in Figure 2.3.

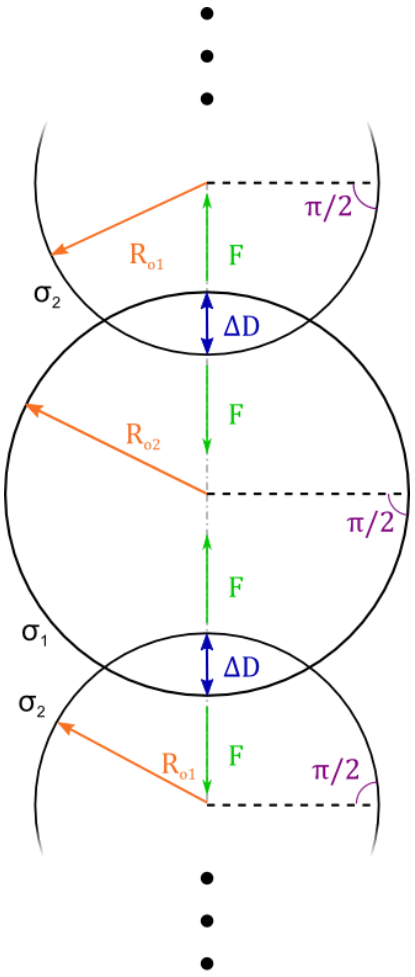


Figure 2.3 An infinite linear chain of interacting spherical bubbles with alternating radii.

The bubbles in Figure 2.3 bear some resemblance to interacting bubbles in SVP porous media; however, bubbles in porous media often come into contact with three or more bubbles with differing radii. In such cases the loading is no longer confined to a single axis, violating the axis-symmetry assumption made by Chan et. al. [10]. In lieu of an arduous derivation of a more general force-displacement relationship, Eq. (3.1) is thought to be an adequate contact law for usage in a DEM framework, subject to assumptions: (a) interacting bubbles retain their spherical shape outside the interaction zone, (b) their initial radii remain unchanged during any interactions, and (c) all fully-immersed bubbles interact as if they were affixed to a wall with $\theta_o = 90^o$. Inserting assumption (c) into Eq. (3.4) yields $B(\theta_{o1}) = \frac{1}{2}$. Using this information, Eq. (3.1) can be simplified:

$$\Delta D \cong \frac{F}{4\pi}\left[\frac{1}{\sigma_1}\ln\left(\frac{F\bar{R}_0}{8\pi\bar{\sigma}R_{o1}^2}\right)+\frac{1}{\sigma_2}\ln\left(\frac{F\bar{R}_0}{8\pi\bar{\sigma}R_{o2}^2}\right)\right] \tag{3.5}$$

Often, the molten pitch can be considered homogenous, and the surface tension acting around every bubble can be considered equal. Mathematically, this means $\sigma = \sigma_1 = \sigma_2$. Substituting this expression into Eq. (3.5) results in:

$$\Delta D \cong \frac{F}{2\pi\sigma}\log\left(\frac{F}{8\pi\sigma R_{AVG}}\right) \tag{3.6}$$

$$R_{AVG} = \frac{R_{o1}+R_{o2}}{2} \tag{3.7}$$

As indicated by [16], Eq. (3.1) (and by extension Eq. (3.6)) is valid only when (a) viscous forces are small in comparison to surface tension forces and (b) the inequality

$$\frac{F}{2\sigma\pi R_{AVG}} \ll 1 \tag{3.8}$$

is satisfied. Inequality (3.8) arises from the assumption that the radius of the contact area is small compared to the radius of the bubble. The left hand side of inequality (3.8) will hereby be referred to as the force ratio. Constraint (a) is satisfied for SVP porous media as the relative motion of bubbles is small during the solidification process. Constraint (b) must be verified on a case-by-case basis.

## 2.4 Validation

To validate the method and the contact law from section 2.3, 24 distinct carbon foam REVs were generated using the current method. Geometric statistical data provided by Oak Ridge National Laboratories [14] were used. A CFD analysis was then performed on one REV using ANSYS-CFX$^{TM}$ software [17], and the results were post-processed to obtain predictions of the permeability, Forchheimer coefficient, and the Nusselt number correlation of the porous material.

### 2.4.1 Digital Sample Generation

The steps to generate digital REVs were completed using an open-source DEM framework called *Yet Another Development Engine* (YADE) [18]. YADE is frequently used to study solid particle packing problems with deformable particles, making it well-

suited for the present application.

In SVP porous media, the primitives are assumed to be spherical bubbles whose interaction is governed by the contact law, Eq. (3.6). YADE employs a penalty method when solving contacts (calculating a reaction force based on the contact interference at each time-step), so it is necessary to solve Eq. (3.6) for the contact force. To accomplish this, the Newton-Raphson method was used to evaluate the force iteratively. Convergence was achieved when the change in force between successive iterations was less than 0.1%.

The number of bubbles in an REV, $N$, was varied from 100 to 400 by increments of 100. Three REVs were generated for each value of $N$, so that 12 REVs were generated in total.

For each simulation, the steps outlined in section 2.2 were followed:

1) The IV was chosen to be a cube, occupying five times the total volume of $N$ bubbles: $V_{IV} = 5NV_{AVG} = 5N\left(\frac{4}{3}\pi R_{AVG}^3\right)$

2) $N$ bubbles were generated. Diameters were selected from a normal distribution having a mean pore diameter of 400 μm and a standard deviation of 120 μm [14].

3) YADE was used to compress the IV. Periodic boundary conditions were enforced throughout the simulation. A surface tension coefficient of 0.035 N/m [19] was assumed for molten tar-pitch. During this step every contact was checked at regular intervals during compression to test if $F/\left(2\pi\sigma_o R_{AVG}\right) < 0.1$. Because this threshold was never exceeded, it was assumed that (b) was satisfied. The simulation was halted when the porosity of the cube reached 80%.

4) Upon completion of the simulation, the sphere locations and sizes were exported to a text file. The text file was then read by a Visual Basic macro, which recreated the geometry in the 3D CAD software package, Solidworks™ [20]. An image of the CAD geometry of one REV can be seen in Figure 2.4.

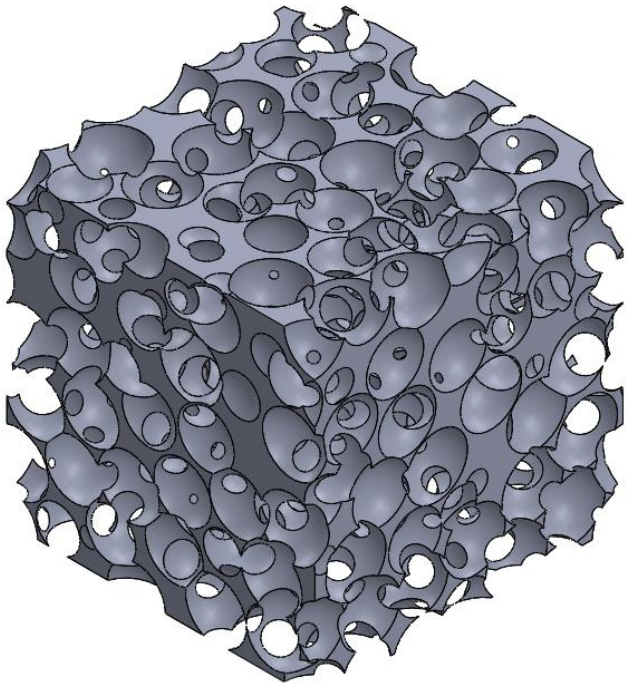

Figure 2.4 CAD isometric view of a REV of graphite foam sample

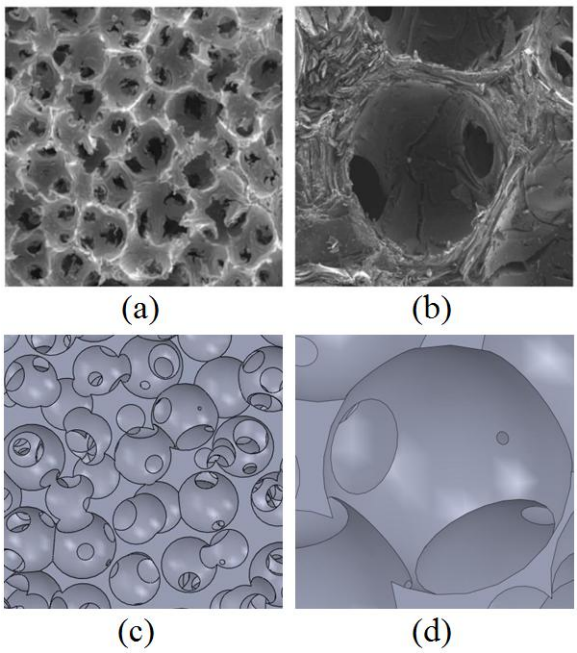


Figure 2.5 Electron micrograph images of a graphite foam specimen (a) and (b) [21] in comparison to a CAD model of geometry generated using the current method (c) and (d)

As Figure 2.5 shows, geometries produced using the current method bear a strong resemblance to their physical counterparts, capturing the random nature of the pores.

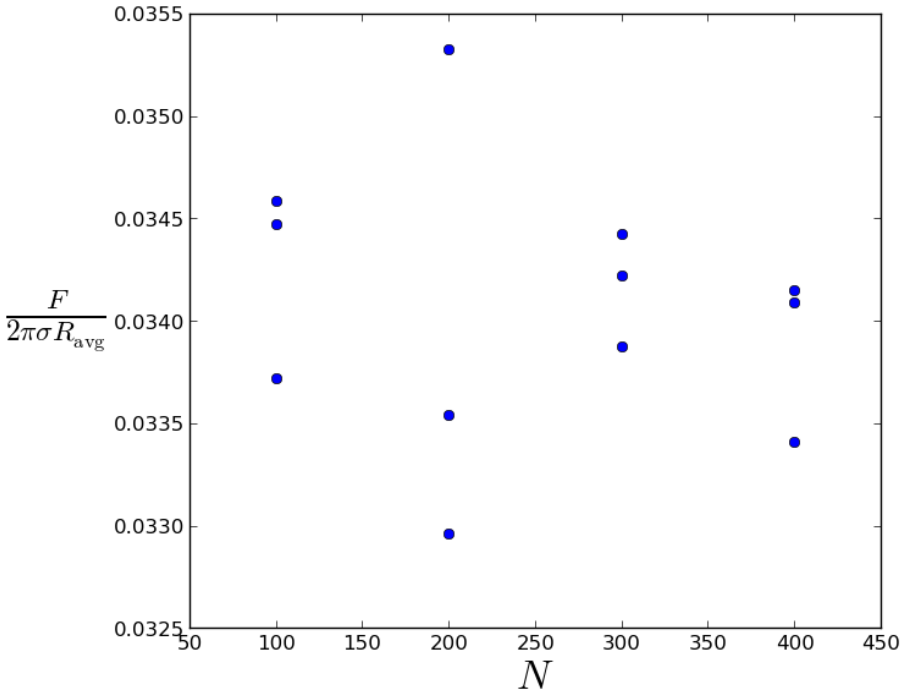


Figure 2.6 Average Force Ratio vs. Number of Primitives.

For each simulation, the average force ratio was evaluated upon completion and the results can be seen in Figure 2.6. These values were considered to be small enough to satisfy inequality (3.8).

### 2.4.2 Setup

Recall that the objective of this work was to generate porous media samples with the intent of extracting desired volume-averaged transport properties. While the DEM simulations produce geometries that visually resemble their physical counterparts, they have not yet been shown to have similar transport properties. To this end, a set of CFD simulations have been conducted using a 100-sphere, 80% porosity REV from the previous section to determine the permeability, Forchheimer coefficient and convection heat transfer coefficients.

#### 2.4.2.1 Problem Setup

Using ANSYS® CFX™ [17], inlet and opening boundary conditions were applied to opposite faces the REV, and a mass flow rate was imposed at the inlet boundary. Translationally periodic interfaces have been set up for the remaining two pairs of faces.

The hydraulic and energy equations were solved simultaneously; buoyant forces were neglected. A constant wall temperature of 393 K was prescribed, and the bulk inlet temperature was 293 K. Energy increase due to viscous dissipation was also neglected.

Because the geometry was assumed statistically isotropic, three sets of simulations were run using the same REV (enforcing the desired mass flow rate across the x, y, and z faces, consecutively) to obtain extra data for comparison.

#### 2.4.2.2 Computational Setup

To prepare the simulations, the geometry was first imported into ANSYS Workbench, where the model was meshed using the ANSYS® Meshing™ [22] tool.

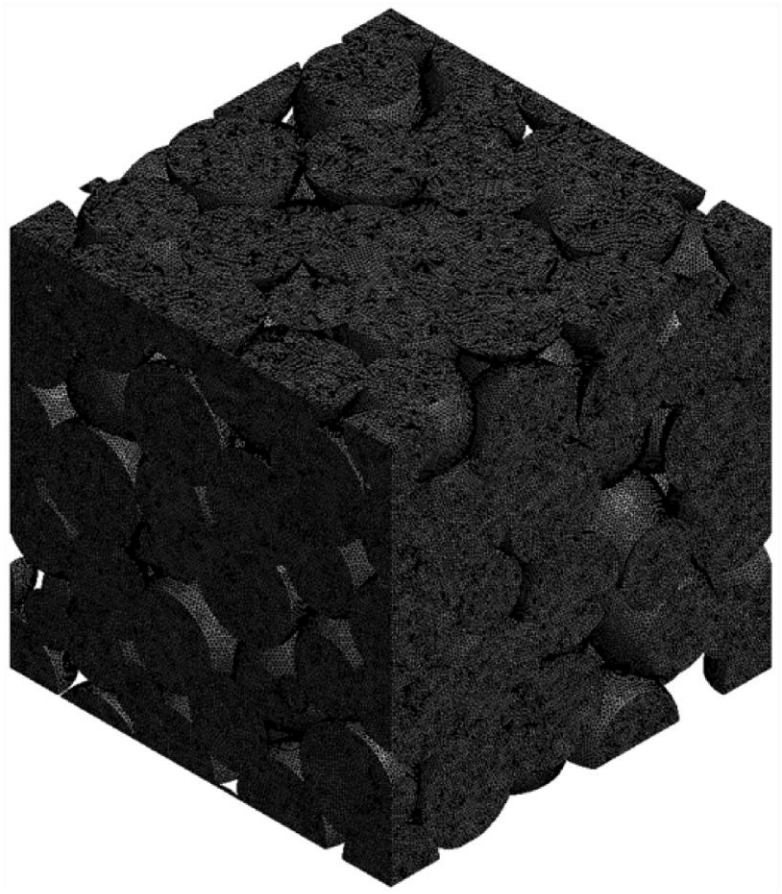

(a)

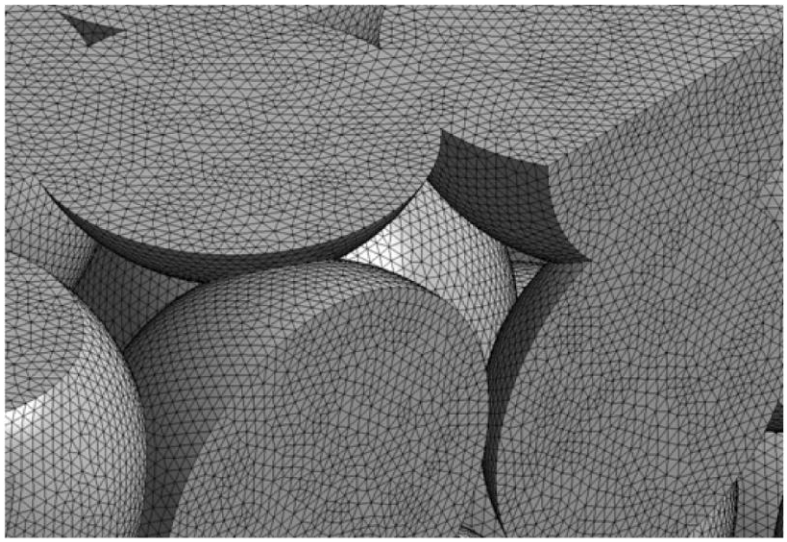

(b)

Figure **2.7** shows the resulting mesh composed of 2,932,590 nodes and 16,435,045 elements.

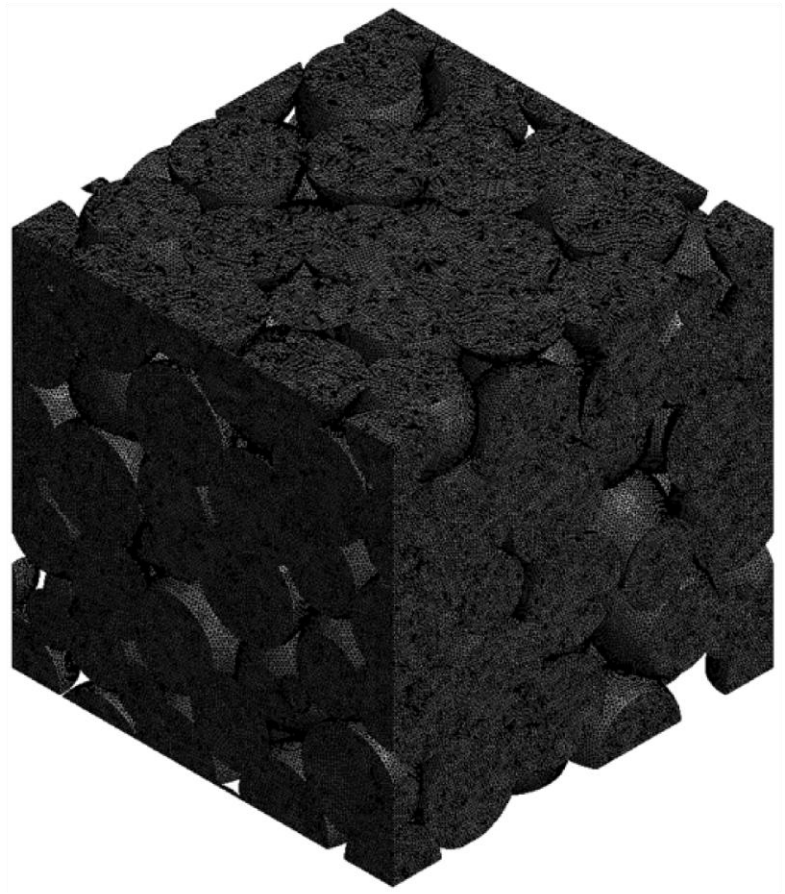

(a)

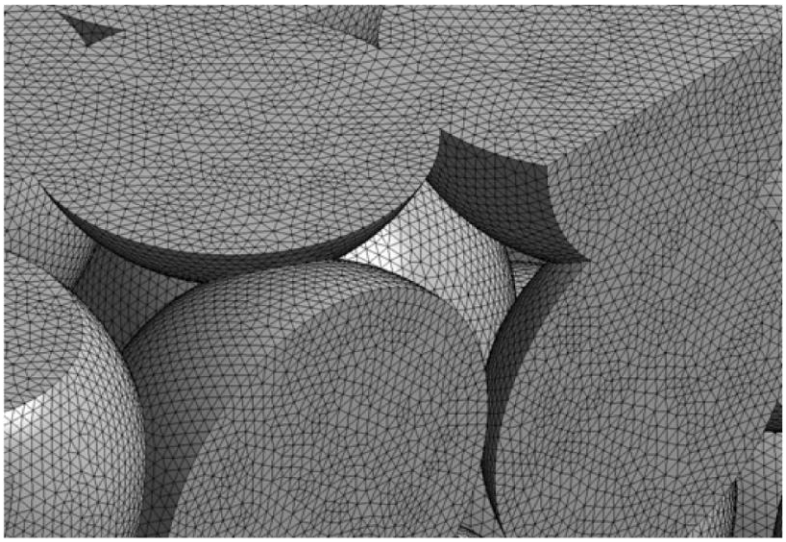

(b)

Figure 2.7 ANSYS generated mesh showing (a) broad-view and (b) close-up

The working fluid is generic and was prescribed constant properties of ρ= 1000 kg/m$^3$, μ= 0.001 N s/m$^2$, k= 0.6 W/m K, and $c_p$= 4184 J/(kg K). The results were computed on a PC with an Intel i7 processor, utilizing 4 cores. Each simulation required approximately 20 minutes to converge the root mean square residuals within $1\times10^{-4}$.

#### 2.4.2.3 Grid Independence

To demonstrate grid independence, the domain was discretized with a finer grid density to yield 6,174,702 nodes, and the $\mathrm{Re}=80$ case was re-run. The overall pressure drop was observed to be grid independent within 4.55%, while the average wall heat flux was observed to be grid independent within 5.38%.

### 2.4.3 Results

#### 2.4.3.1 Momentum Results

To observe the pressure drop within the Darcy regime and the stationary flow regime, the Reynolds numbers considered are $\mathrm{Re}_d \in \{0.1, 0.5, 1, 10, 20, 30, 40, 50, 60, 70, 80\}$.

The Darcy-Forchheimer Law may be stated as [23]:

$$\frac{\Delta P}{L} = \frac{\mu}{K}U + \frac{c_f}{\sqrt{K}}\rho U^2 \tag{3.9}$$

where $K$ is the permeability and $c_f$ is the Forchheimer coefficient. The curve fit function available in the python module, numpy.polyfit [24] was used to fit the results to Eq. (3.9). Figure 2.8 shows the simulation data and the fitted curves compared with results obtained by other researchers.

The Reynold's number based on pore diameter is

$$\mathrm{Re}_d = \frac{\rho U d}{\mu} \tag{3.10}$$

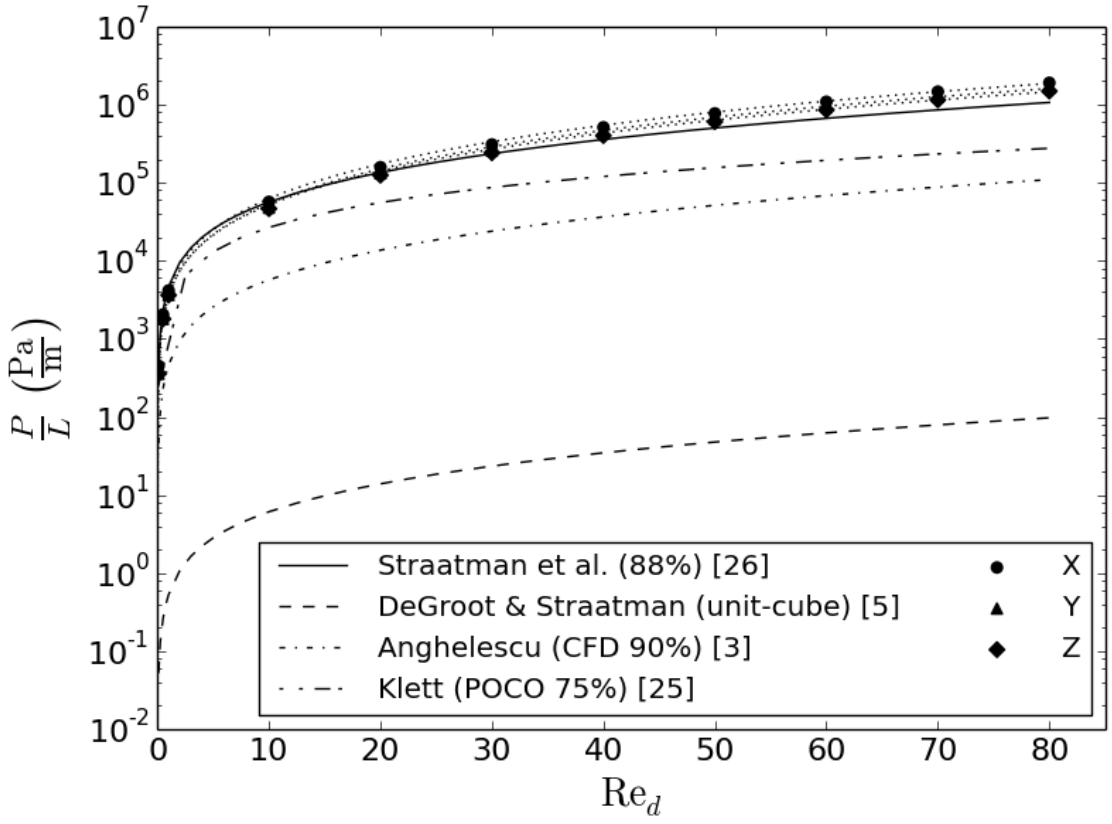


Figure 2.8 Pressure Drop vs. Reynolds' Number. Markers are computed points; lines are Darcy-Forchheimer correlation

The x, y, and z series show good agreement with each other. This indicates that the subject REV is roughly (statistically) isotropic, and contains enough primitives to be a good representation of the desired microstructure. If significant differences between the curves were observed, it would indicate that too few microstructural features were present to achieve statistically significant results, and more primitives and/or more REVs would have needed to be modeled to increase the statistical significance of the predicted property.

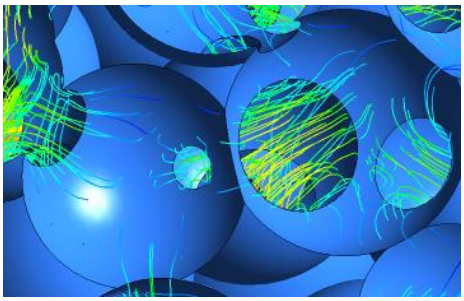

Figure 2.9 Close-up of streamline plot inside the current geometry. The global flow direction is into the page. Warmer colors indicate higher velocity.

The present model is first compared to the unit-cube model analyzed by DeGroot & Straatman [5]. Because both approaches use idealized geometry, contrasting the two highlights only the effects of using a randomized geometry over uniform one. One such geometric difference is the variation in pore window size and pore window alignment.

Consider, for example, the neighboring pores in Figure 2.9. The left pore has 3 visible windows; two are poorly aligned, and the third is very small. This is in contrast to the right pore, which has 2 sizable windows, both with fair alignment with the global flow direction. The streamline coloring indicates that the flow much prefers the right pore to the left. In contrast to the velocity variations in the present analysis, each pore in the unit cube model has 3 exit windows, all misaligned from the global flow direction by the same amount. Therefore, it is not surprising that the velocity variation predicted by the unit cube model is less pronounced than that of the current model. Furthermore, it is well known that beyond Darcy flow, fluid drag, and, by extension, pressure drop varies non-linearly with velocity. Thus, the regions with higher flow speeds in the current model experience a much greater drag, resulting in a greater overall pressure drop than that predicted using the unit-cube model.

Both the trend and the magnitudes predicted by the current model align well with the correlations predicted by other researchers. Klett [25] ran experiments on POCO$^{TM}$ foam of 75% porosity, while Anghelescu [3] reported CFD results based on scanned samples of 90% porosity graphite foam. Physical SVP porous media is known to have non-spherical pores, jagged pore windows and blocked regions, all of which will disrupt the flow. Such features will undoubtedly have an impact on the flow field, thereby decreasing the

observed permeability. Because none of these features are present in the current model, it is not surprising that predicted pressure drops are still lower than measured values. The extracted permeability and Forchheimer coefficients are given in  where they are compared with the values obtained by DeGroot & Straatman [5], and Straatman et al. [23].

Table 2.2 Permeability and Forchheimer Coefficients

| Model | Permeability ($m^2$) $K$ | Forchheimer coefficient $c_f$ |
|---|---|---|
| POCO™ [a] [23] | $6.13\times10^{-10}$ | 0.4457 |
| Unit-cube [b] [5] | $5.25\times10^{-06}$ | 0.00395 |
| Current Model [c] | $1.620\times10^{-10}$ | 0.6322 |

[a] Porosity of 82%; [b] Values were re-fitted to equation (3.9); [c] Values were averaged between three flow directions

### 2.4.3.2 Energy Results

The interfacial Nusselt number in each simulation was computed using the heuristic closure proposed by Quintard [27]:

$$\mathrm{Nu}_{fs} = \frac{A_{fs} h_{fs} d^2}{k_f} = \frac{\int_{A_{fs}} \mathbf{n}_f \cdot k_f \nabla T_f dA}{\left( \langle T_s \rangle^s - \langle T_f \rangle^f \right)} \frac{d^2}{k_f}, \tag{3.11}$$

where the integral term is the heat transfer into the domain, $A_{fs}$ is the interfacial surface area of the REV, $k_f$ is the thermal conductivity of the fluid, and $\langle T_s \rangle^s$ and $\langle T_f \rangle^f$ are the intrinsic volume averaged temperatures of the solid and fluid phases, respectively. A surface-area-to-volume ratio of 8665 $m^{-1}$ was determined using Solidworks™. The data was then fit using the numpy.polyfit function to a second degree polynomial:

$$\mathrm{Nu}_{fs} = a_2 \mathrm{Re}_d^2 + a_1 \mathrm{Re}_d + a_0. \tag{3.12}$$

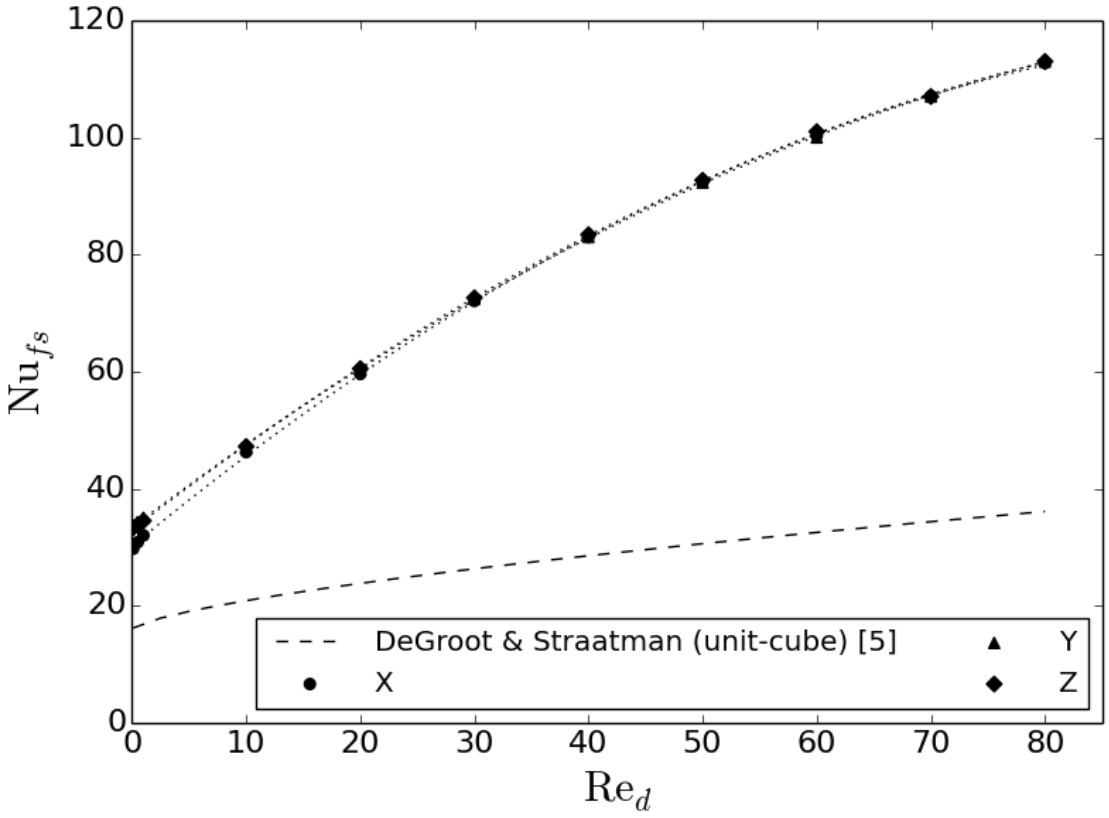


Figure 2.10 Nusselt number vs. Reynold's number. Markers are computed points; lines are curve fits to Eq. (3.12)

Figure 2.10 shows the present simulation data and relevant curve fits in comparison with the unit-cube results in [5]. The average coefficients $a_0 = 32.2$, $a_1 = 1.53$, and $a_2 = -0.0066$ may be inserted into equation (2.61) to give a reasonable fit with the data. Comparisons have not been made with experimental data because the interfacial Nusselt number cannot be directly compared with the average Nusselt numbers found from design scale problems such as those in [25, 26]. The interfacial heat transfer is much larger than that predicted by DeGroot & Straatman [5] using the unit-cube geometric model. A more accurate representation of the pore-level mixing is the main reason for the Nusselt number differences. Using the unit-cube geometric model, the pore-level flow is structured and spatially periodic. The flow field predicted using the current geometric model is well-mixed resulting in much higher convective heat transfer.

## 2.5 Property Identification

While the analysis of section 2.4 adequately validated the model, hydraulic and thermal properties have only been identified for $d = 400\ \mu\text{m}$, and $\varepsilon = 0.80$. In preparation for subsequent work, we will identify the hydraulic and thermal properties of SVP carbon foam for a range of pore diameters and porosities.

To observe the effects of varying the mean pore diameter and porosity, four additional REVs have been generated, each containing 100 spheres. First, three REVs with a mean pore diameter of $d = 600\ \mu\text{m}$ and porosities $\varepsilon \in \{0.75, 0.8, 0.85\}$ were created. A second set of REVs were generated with porosity $\varepsilon = 0.80$ and mean pore diameters $d = \{400\ \mu\text{m}, 600\ \mu\text{m}, 800\ \mu\text{m}\}$ (the same 600 μm, 80% porosity sample was used in both sets, and the data from the $400\ \mu\text{m}$ sample was reused from section 2.4.3). The ratio of standard deviation to pore diameter was fixed at $\frac{\sigma_d}{d} = 0.3$ in each sample.

An Unstructured computational grid was generated from the negative volume of each REV using the ANSYS Meshing tool, where the grid density for each mesh is approximately the same as the validation case. Hydraulic and thermal simulations have again been carried out using ANSYS CFX, for $\text{Re} \in \{10, 40, 60, 80\}$. The results have been extracted, post-processed, and fitted to correlations (3.9) and (3.11). The inferred coefficients are plotted in Figure 2.11 and Figure 2.12.

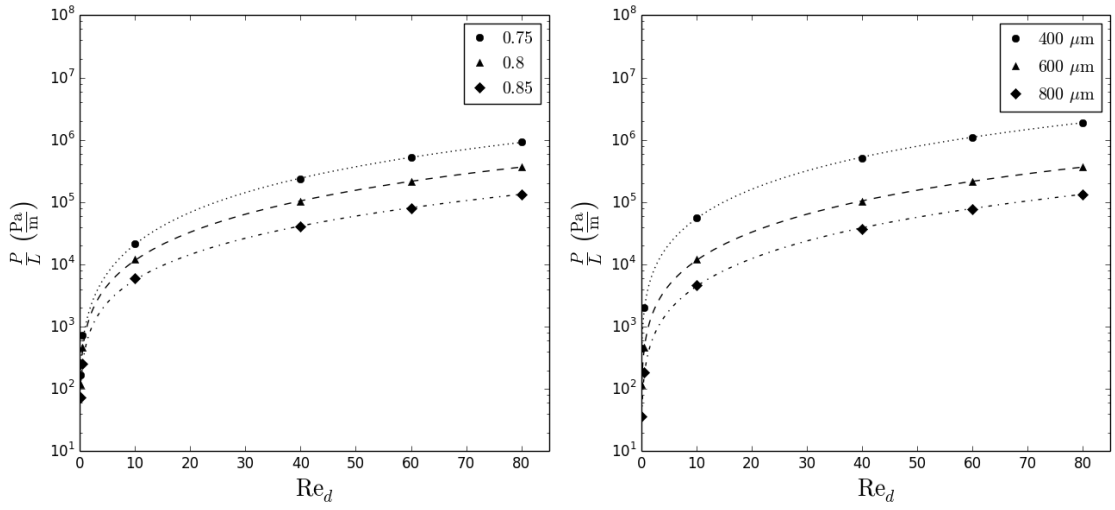


Figure 2.11 Pressure Drop vs. Reynolds number; markers are simulation data, lines are curve fits

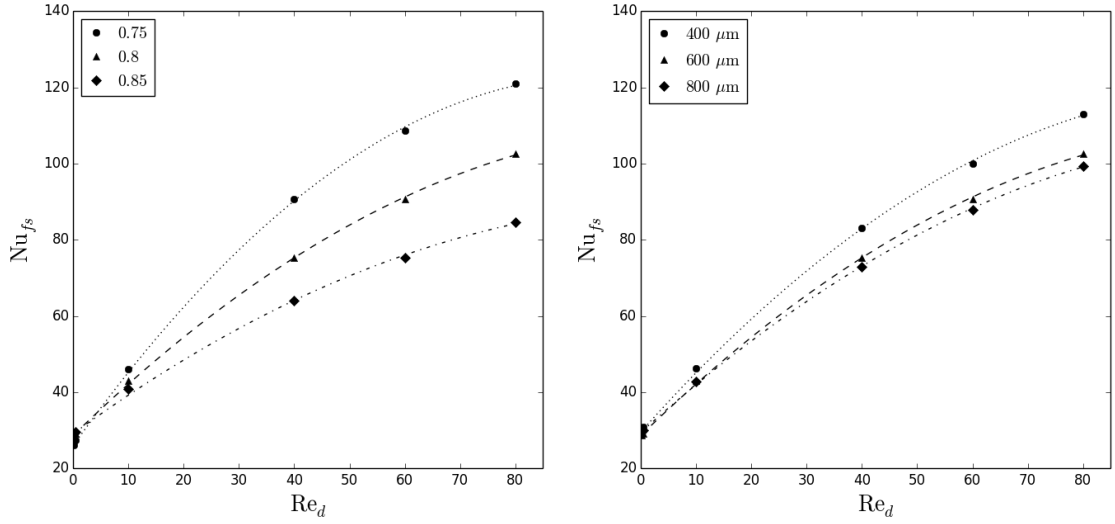


Figure 2.12 Interfacial Nusselt number vs. Reynolds number; markers are simulation data, lines are curve fits

These will be used in future volume averaged simulations.

## 2.6 Summary

In this work, a novel method for generating stochastic, spatially periodic digital samples of porous media was outlined. The method requires access to DEM, CAD, and CFD

software, but does not require any special equipment beyond a capable personal computer. To demonstrate the effectiveness of this approach, 24 digital samples of SVP porous media were generated using only aggregate statistical data collected from physical samples. The resulting digital samples were used in CFD simulations to predict permeability and Forchheimer coefficients as well as the constants for the Nusselt number correlation (Eq. (3.12)), and the data were compared to correlations obtained by other researchers. The hydraulic behavior is in very good agreement in terms of the trend with increasing Reynolds number, and is closer in magnitude than all previous modeling attempts. The remaining deviations in pressure drop between the present digital REV and actual foam samples is thought to be due to non-spherical pores, jagged pore windows, and to blocked regions, none of which are accounted for in the digital REV. The thermal behavior follows the correct trend with increasing Reynolds number, but over-predicts the magnitude of the heat transfer compared to experiments. Once again, this is felt to be due mainly to blockage that is present in real foam sample, but not accounted for in the digital REV. Nonetheless, the present formulation produces an accurate mathematical representation of a spherical void phase foam that contains all of features necessary to study all modes of heat exchange at the pore level. Combined with the fact that the current approach also incorporates variable pore size and random pore positioning, the current approach is considered most viable for studying problems involving incident radiation.

## 2.7 Acknowledgements

The authors gratefully acknowledge the financial support from the Natural Sciences and Engineering Research Council of Canada (NSERC). The authors would also like to thank Dr. Jan Stransky, who coded the bubble contact law in YADE, and Dr. Bruno Chareyre and Dr. Anton Gladky for their advice and assistance in working with YADE. Finally, the authors would like to acknowledge the help Alex Kalopsis, who carried out the ANSYS CFX simulations.

## 2.8 References

[1] S. Haussener, P. Coray, W. Lipinski, P. Wyss and A. Steinfeld. Tomography-based heat and mass transfer characterization of reticulate porous ceramics for high-temperature processing. *J. Heat Transfer 132(2)*, pp. 023305. 2010. Available: http://dx.doi.org/10.1115/1.4000226. DOI: 10.1115/1.4000226.

[2] B. Maruyama, J. E. Spowart, D. J. Hooper, H. M. Mullens, A. M. Druma, C. Druma and M. K. Alam. A new technique for obtaining three-dimensional structures in pitch-based carbon foams. *Scr. Mater. 54(9)*, pp. 1709-1713. 2006. . DOI: http://dx.doi.org/10.1016/j.scriptamat.2005.12.060.

[3] M. S. Anghelescu. Thermal and mechanical analysis of carbon foam. *ProQuest Dissertations and Theses* 2009. Available: http://search.proquest.com/docview/304963894?accountid=15115.

[4] Q. Yu, B. E. Thompson and A. G. Straatman. A unit cube-based model for heat transfer and fluid flow in porous carbon foam. *Journal of Heat Transfer 128(4)*, pp. 352-360. 2006.

[5] C. T. DeGroot and A. G. Straatman. Numerical results for the effective flow and thermal properties of idealized graphite foam. *Journal of Heat Transfer 134(4)*, pp. 042603-042603. 2012. . DOI: 10.1115/1.4005207.

[6] P. Kumar, J. Hugo, F. Topin and J. Vicente. Influence of pore and strut shape on open cell metal foam bulk properties. *AIP Conference Proceedings 1453(1)*, pp. 243-248. 2012. Available: http://search.ebscohost.com/login.aspx?direct=true&db=a9h&AN=75230839&site=ehost-live. DOI: 10.1063/1.4711183.

[7] K. C. Leong and H. Y. Li. Theoretical study of the effective thermal conductivity of graphite foam based on a unit cell model. *Int. J. Heat Mass Transfer 54(25–26)*, pp. 5491-5496. 2011. . DOI: http://dx.doi.org/10.1016/j.ijheatmasstransfer.2011.07.042.

[8] L. James, S. Austin, C. A. Moore, D. Stephens, K. K. Walsh and G. Dale Wesson. Modeling the principle physical parameters of graphite carbon foam. *Carbon 48(9),* pp. 2418-2424. 2010. Available: http://resolver.scholarsportal.info/resolve/00086223/v48i0009/2418_mtpppogcf. DOI: 10.1016/j.carbon.2010.02.043.

[9] M. Kırca, A. Gül, E. Ekinci, F. Yardım and A. Mugan. Computational modeling of micro-cellular carbon foams. *Finite Elements Anal. Des. 44(1–2),* pp. 45-52. 2007. . DOI: http://dx.doi.org/10.1016/j.finel.2007.08.008.

[10] M. Wang and N. Pan. Modeling and prediction of the effective thermal conductivity of random open-cell porous foams. *Int. J. Heat Mass Transfer 51(5–6),* pp. 1325-1331. 2008. . DOI: http://dx.doi.org/10.1016/j.ijheatmasstransfer.2007.11.031.

[11] C. C. Chueh, A. Bertei, J. G. Pharoah and C. Nicolella. Effective conductivity in random porous media with convex and non-convex porosity. *Int. J. Heat Mass Transfer 71(0),* pp. 183-188. 2014. Available: http://www.sciencedirect.com/science/article/pii/S0017931013010855. DOI: http://dx.doi.org/10.1016/j.ijheatmasstransfer.2013.12.041.

[12] W. M. VISSCHER and M. BOLSTERLI. Random packing of equal and unequal spheres in two and three dimensions. *Nature 239(5374),* pp. 504-507. 1972. Available: http://dx.doi.org/10.1038/239504a0.

[13] M. Tancrez and J. Taine. Direct identification of absorption and scattering coefficients and phase function of a porous medium by a monte carlo technique. *Int. J. Heat Mass Transfer 47(2),* pp. 373-383. 2004. Available: http://resolver.scholarsportal.info/resolve/00179310/v47i0002/373_dioaasmbamct. DOI: 10.1016/S0017-9310(03)00146-7.

[14] J. W. Klett, A. D. McMillan, N. C. Gallego and C. A. Walls. The role of structure on the thermal properties of graphitic foams. *J. Mater. Sci. 39(11),* pp. 3659-3676. 2004. Available:

http://resolver.scholarsportal.info/resolve/00222461/v39i0011/3659_trosottpogf. DOI: 10.1023/B:JMSC.0000030719.80262.f8.

[15] D. Y. Chan, E. Klaseboer and R. Manica. Film drainage and coalescence between deformable drops and bubbles. *Soft Matter 7(6),* pp. 2235-2264. 2011.

[16] D. Y. C. Chan, E. Klaseboer and R. Manica. Theory of non-equilibrium force measurements involving deformable drops and bubbles. *Adv. Colloid Interface Sci. 165(2),* pp. 70-90. 2011. . DOI: 10.1016/j.cis.2010.12.001.

[17] ANSYS, "ANSYS v13.0; CFX v5," .

[18] V. Smilauer and B. Chareyre. "Yade dem formulation," in *Yade Documentation* (1st ed.), V. Smilauer, Ed. 2010, .

[19] D. P. Anderson, P. G. Wapner and D. B. Curliss. Physical property characteristics of pitch materials. Presented at MRS Proceedings. 1992, .

[20] Dassault Systemes, "Solidworks Educational Version 2012-2013," .

[21] J. W. Klett. *Process for Making Carbon Foam* 2000.

[22] ANSYS, "Workbench Meshing Tool," vol. 15.0, .

[23] S. Whitaker. The forchheimer equation: A theoretical development. *Transp Porous Med 25(1),* pp. 27-61. 1996. Available: http://resolver.scholarsportal.info/resolve/01693913/v25i0001/27_tfeatd. DOI: 10.1007/BF00141261.

[24] E. Jones, T. Oliphant and P. Peterson. SciPy: Open source scientific tools for python. *Http://Www.Scipy.Org/* 2001.

[25] J. Klett, A. McMillan and D. Stinton. Modeling geometric effects on heat transfer with graphite foam. Presented at 26th Annual Conference on Ceramic, Metal, and Carbon Composites, Materials, and Structures, Cocoa Beach, Florida. 2002, .

[26] A. G. Straatman, N. C. Gallego, Q. Yu, L. Betchen and B. E. Thompson. Forced convection heat transfer and hydraulic losses in graphitic foam. *Journal of Heat Transfer 129(9),* pp. 1237-1245. 2006. . DOI: 10.1115/1.2739621.

[27] M. Quintard. Modelling local non-equilibrium heat transfer in porous media. *Heat Transfer 1*pp. 279-286. 1998.

# Chapter 3

# 3 Radiative Property Characterization of Spherical Void Phase Porous Media

The present work uses a popular discrete-scale Monte-Carlo method to determine the extinction coefficient of spherical-void-phase carbon foam having mean pore diameters $d \in \{400\ \mu\text{m}, 600\ \mu\text{m}, 800\ \mu\text{m}\}$, with porosities $\varepsilon \in \{0.70,\ 0.75, 0.80, 0.85\}$. The representative elementary volumes were constructed using a known digital generation method, and the surface-area-to-volume ratios were identified directly from the digital models. The extinction coefficients were identified using the aforementioned method and a correlation is fitted to the data. It was found that the extinction coefficient is very large, suggesting that, for mean pore diameters and porosities in the given ranges, carbon foam may nearly always be treated as a black body.

## 3.1 Introduction

Many engineering applications involve radiation transport within porous materials, including porous media burners [1-3], and solar collectors [4, 5]. If the volume-averaged radiative properties (absorbtion and scattering coefficients) of the porous structure are known, the Radiation Transfer Equation (RTE) may be applied to obtain the radiation field within the domain. Appropriate source and sink terms may be added to the RTE and the energy equation to enable the two-way coupling required to solve a wide variety of engineering problems.

A common method for determining radiation properties in heterogeneous media is the Monte Carlo (MC) ray-tracing technique originally presented by Tancrez and Taine [6]. The method requires that a large number of ray-bundles be launched from non-opaque phases within a representative microstructure. The ray-bundles are allowed to interact naturally at phase boundaries as they propagate through the media. The histories of the ray-bundles are fitted to appropriate statistical distribution functions, and the best fit coefficients are identified as the pertinent effective properties. Researchers have successfully implemented this method to obtain radiative properties idealized geometries

[6-8], as well as real microstructures [8-10] (where the digital approximation of the physical sample is obtained through X-ray tomography).

In chapter 2, a method for obtaining digital samples of porous media from aggregate statistical data was described, and digital samples of graphitic foam were produced to validate and demonstrate the method. The present work employs the same method to generate digital samples of graphitic foam, and a discrete-scale MC ray-tracing technique was applied to those samples to determine the range of extinction coefficients.

## 3.2 The Volume Averaged Radiative Transport Equation

The general, quasi-steady, Radiative Transport Equation (RTE) is given by [11, 12]:

$$\begin{aligned}\hat{\mathbf{s}}\cdot\nabla_{\mathbf{r}} I(\mathbf{r},\hat{\mathbf{s}}) &= -\left[\kappa+\sigma_s\right] I(\mathbf{r},\hat{\mathbf{s}}) + \kappa I_b(\mathbf{r}) \\ &+ \frac{\sigma_s}{4\pi}\int_{4\pi} I(\mathbf{r},\hat{\mathbf{s}}_{\text{in}})\Phi(\hat{\mathbf{s}}_{\text{in}},\hat{\mathbf{s}})\,\mathrm{d}\Omega_{\text{in}},\end{aligned} \tag{4.1}$$

where $\kappa_\lambda$ is the absorption coefficient and $\sigma_{s,\lambda}$ is the scattering coefficient, and wavelength subscripts have been dropped for brevity. It is often convenient to express their sum as a single quantity, known as the extinction coefficient:

$$\beta = \kappa + \sigma_s. \tag{4.2}$$

The extinction coefficient therefore captures the combined effects of absorption and out-scattering, or the radiation deflected away from the current direction, $\hat{\mathbf{s}}$.

The volume averaging theorems developed by Whitaker [13] have been widely used in the averaging of more common transport equations, such as mass, momentum, and energy. The extrinsic, intrinsic, and spatial averaging theorems are given as follows for a medium consisting of phases $m$ and $n$:

$$\langle \phi_m \rangle \equiv \frac{1}{V}\int_{V_m} \phi_m dV, \tag{4.3}$$

$$\left\langle \phi_m \right\rangle^m \equiv \frac{1}{V_m}\int_{V_m} \phi_m dV. \tag{4.4}$$

$$\underbrace{\left\langle \nabla \phi_m \right\rangle}_{\substack{\text{Superficial average}\\ \text{of gradient of quantity}\\ \text{within phase } m}} = \underbrace{\nabla\left\langle \phi_m \right\rangle}_{\substack{\text{Gradient of superficial}\\ \text{average of quantity}\\ \text{within phase } m}} + \underbrace{\frac{1}{V}\int_{A_{mn}} \hat{\mathbf{n}}_{mn}\phi_m dA}_{\substack{\text{Volume average of } \phi\\ \text{crossing the interface from}\\ n \text{ to } m}}. \tag{4.5}$$

The intrinsic and extrinsic definitions may be related through the phase volume fraction:

$$\left\langle \phi_m \right\rangle = \varepsilon \left\langle \phi_m \right\rangle^m. \tag{4.6}$$

To economically model radiation transport within a porous medium comprised of one transparent phase and one opaque phase, Lipinski et al. [14] have applied theorems (4.3) - (4.6) to the discrete phase RTE (4.1) to synthesize the volume averaged RTE in *differential* form:

$$\begin{aligned} \hat{\mathbf{s}}\cdot\nabla_{\mathbf{x}}\left\langle I_f(\mathbf{x},\hat{\mathbf{s}})\right\rangle^f &= -\beta_{\text{int}}\left\langle I_f(\mathbf{x},\hat{\mathbf{s}})\right\rangle^f + \kappa_{\text{int}}\left\langle I_{b,s}(\mathbf{x})\right\rangle^f \\ &+ \frac{\sigma_{s,\text{int}}}{4\pi}\int_{4\pi}\left\langle I_f(\mathbf{x},\hat{\mathbf{s}}_{\text{in}})\right\rangle^f \Phi_{\text{int}}(\hat{\mathbf{s}}_{\text{in}},\hat{\mathbf{s}})\,\mathrm{d}\Omega_{\text{in}}, \end{aligned} \tag{4.7}$$

where $\beta_{\text{int}} = \kappa_{\text{int}} + \sigma_{s,\text{int}}$ is the effective extinction coefficient. The form of the equation has remained the same, while the continuous transport properties have been replaced by their volume averaged counterparts. In deriving Eq. (4.7), effective absorption and scattering coefficients have been defined. These definitions are found in Ref. [14] and they have be used to identify the radiative properties using discrete MC simulations (See Petrasch et al. [15]). We have instead opted to use the heuristic method of Tancrez and Taine [6], and assumed the identified properties are applicable to Eq. (4.7)

## 3.3 Radiation Property Identification

As mentioned above, the MC ray-tracing technique has been successfully used to determine the radiation properties of a variety of porous media. The reasoning behind the method introduced by Tancrez and Taine [6] will be reviewed here, followed by a brief description of the present implementation, and discussion of the results.

### 3.3.1 Bouger's Law and the Cumulative Distribution Function

The derivation begins with the definition of the extinction coefficient. Consider the incident radiation, impinging normally on an infinitesimally thick slab of semi-transparent material as in Figure 3.1.

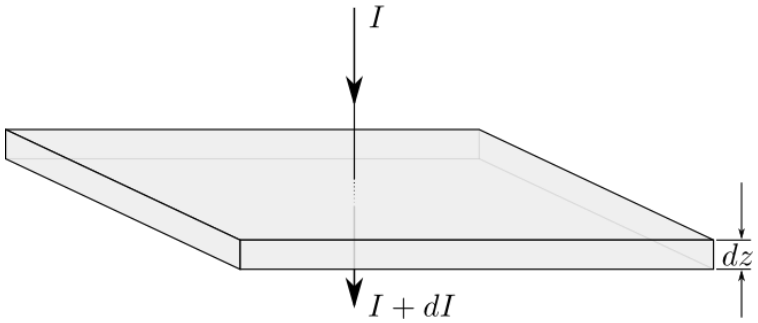


Figure 3.1 Intensity incident normally on an attenuating slab of thickness $dz$

It has been experimentally observed that radiation is within such a slab is attenuated in accordance with the proportionality

$$dI \propto -Idz. \tag{4.8}$$

An equation may be formed by introducing a constant of proportionality:

$$dI = -\beta Idz, \tag{4.9}$$

where $\beta$ is the extinction coefficient has appeared.

Eq. (4.9) is an ordinary differential equation, solvable using the well-known separation of variables technique:

$$I = I_o e^{-\beta z}. \tag{4.10}$$

Eq. (4.10) is Bouguer's law, which is sufficient to describe the attenuation of radiation in many semi-transparent media. It is widely accepted that intensity in a particular direction is proportional to the number of photons travelling in that direction, therefore, Eq. (4.10) can be rewritten as

$$N = N_o e^{-\beta z}. \tag{4.11}$$

where $N_o$ is the number of photons entering the medium, and $N$ is the number of photons leaving the slab. Eq. (4.11) can also be expressed in terms of the number of photons attenuated at thickness $z$, $N_z'$:

$$\frac{N_z'}{N} = 1 - e^{-\beta z}. \tag{4.12}$$

Finally, the fraction of absorbed photons at distance $z$ is identified as the cumulative distribution of photon travel distances, or ray lengths:

$$G(z) = 1 - e^{-\beta z}. \tag{4.13}$$

Eq. (4.13) is accurate for many homogenous, semi-transparent media, and it is desirable to treat heterogeneous media in a similar manner. In a two-phase medium, such as carbon foam, $G(z)$ can be empirically determined by casting a large number of rays from the transparent phase and analyzing each of their histories. $G(z)$ may be inserted into Eq. (4.13) to evaluate $\beta$.

### 3.3.2 Implementation of the MC Ray-tracing Method

Two key assumptions can be made to simplify the ray-casting procedure. If the geometry is considered homogenous at the macroscopic scale, the distribution of ray lengths will

not vary with the position of the origin plane, so ray origins may be selected from all points within the domain. Moreover, if the geometry is isotropic, a similar argument leads to the conclusion that ray directions may also be randomly selected.

In the present study, the carbon foam under consideration has two distinct phases: the solid carbon matrix, and the intervening fluid. The solid matrix assumed to be black, while the fluids of interest, air, is considered to be transparent.

Rays are launched from random locations within the fluid phase in random directions. When a collision is detected at the periodic boundary of the microstructure, the ray length is stored, and the ray re-launched in the same direction from the corresponding location on the opposite face. Upon collision with the solid matrix, the ray is terminated, and its cumulative length is calculated and written to file. More details are provided in the computer code which accompanies this publication. Upon completion, a computer program was used to bin the ray lengths and fit the data to Eq. (4.13).

### 3.3.3 Sample Generation

Before executing the discrete-scale MC technique to determine the desired properties, digital samples of the porous medium of interest must be obtained. In the present work, these are generated using the method of chapter 2, which is briefly summarized here.

Some two-phase media are best described as packings of particles, where the particles comprise the discrete phase. The opposite phase is usually a continuous substance in which the packing is immersed. To analyze such media using the aforementioned method, the analyst must choose a set of particle geometries to be packed into a periodic domain. The particles should be placed at random locations within an initial volume without interference. When all the particles have been inserted, the periodic walls of the domain are slowly compressed. During compression, contact between particles is resolved using a pre-determined force-displacement relationship, or contact law. The simulation is finished when a target criterion is reached (e.g. desired porosity has been achieved).

For the case of carbon foam, the natural particle geometry is the sphere, which represents a bubble inside the domain. It is further assumed that the bubble diameters may be sampled from a normal distribution, whose mean and standard deviation are representative of the bubbles in the foam of interest. The bubble-bubble contact law of chapter 2 has been used:

$$\Delta D \cong \frac{F}{2\pi\sigma_t}\log\left(\frac{F}{8\pi\sigma_t R_{AVG}}\right), \tag{4.14}$$

where a suitable surface tension, $\sigma_t = 0.035$ N/m (see Ref. [16]), has been assumed. An image of the Solidworks$^{TM}$ [17] model can be seen in Figure 3.2.

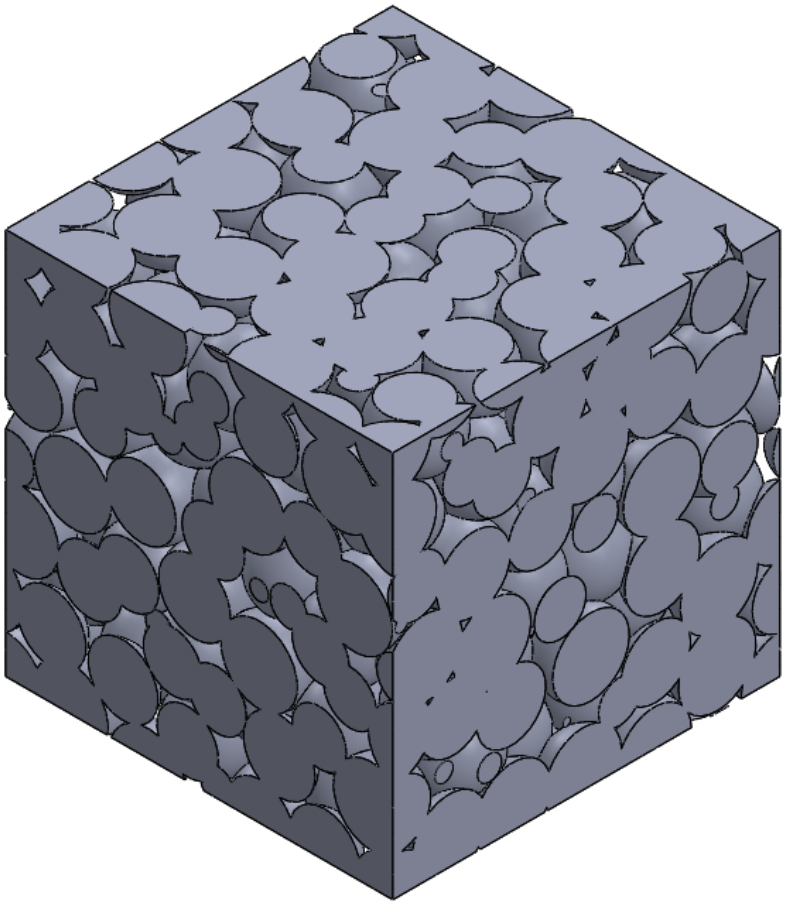

Figure 3.2 Negative volume of a digitally generated carbon foam sample;

$N_s = 300,\ d = 400\ \mu\text{m},\ \sigma_d = 120\ \mu\text{m},\ \varepsilon = 0.80$

One of the aims of the present work is to determine the effects of varying porosity and mean bubble diameter on the overall extinction coefficient. Before generating these REVs, a suitable REV size must be determined.

### 3.3.4 REV Sizing

When collecting data from small material samples, it is important to verify that the samples are indeed representative of the material of interest. Groups of small samples are expected to exhibit large variance in effective properties because they do not contain a statistically relevant number of microstructural features. Conversely, very large samples require more computational resources to generate and analyze. Any sample containing enough microstructural features to accurately predict the properties of interest is called a Representative Elementary Volume (REV). In the present work, it was of interest to determine a suitable REV size for extinction coefficient identification. To this end, a set of 24 cubic digital carbon foam samples were generated; bubble diameters were sampled from a normal distribution with a mean, $d = 400\ \mu\text{m}$, and standard deviation $\sigma_d = 120\ \mu\text{m}$. The final porosity of each sample was $\varepsilon = 0.80$. In the discrete MC analysis, the histories of least $5\times10^4$ rays were tracked. The results can be seen in Figure 3.3.

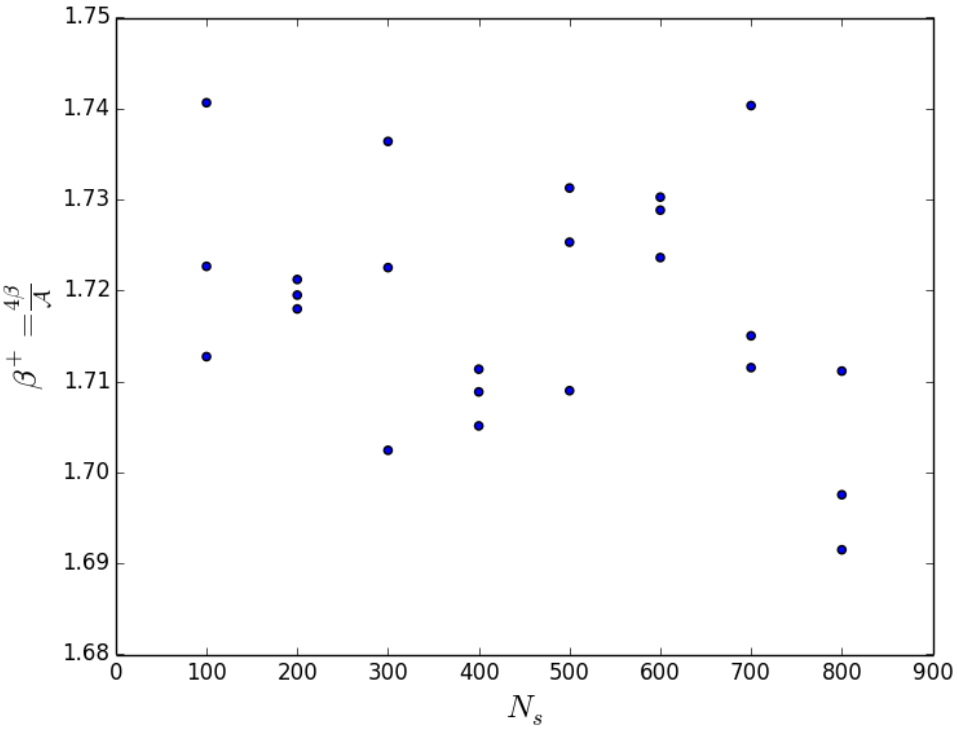


Figure 3.3 Extinction Coefficient vs. Number of Primitives. $\beta^+$ is the non-dimensional extinction coefficient.

In Figure 3.3 the data has no discernible trends, and are scattered about the mean value, $\beta^+ = 1.72$. Because all the data lie within $\pm 2\%$ of the mean, the number of rays cast was deemed sufficient for the present application, and all sample sizes appear to have a sufficient number of features to accurately predict the desired property. This analysis has given the authors confidence to assume that samples containing $N_s = 300$ bubbles will serve as adequate REVs for predicting radiative properties of carbon foam for similar porosities and average bubble diameters.

### 3.3.5 Property Identification

It is of interest to see the effects of pore diameter and porosity variation on the performance of a carbon foam solar collector. To do this, the relevant radiative properties must be inferred from the results of pore-level analyses of the REVs of interest. This section describes the property identification process.

To begin, three sets of REVs were generated with average bubble diameters, $d \in \{400\ \mu\text{m}, 600\ \mu\text{m}, 800\ \mu\text{m}\}$, and standard deviations, $\sigma_d \in \{120\ \mu\text{m}, 180\ \mu\text{m}, 240\ \mu\text{m}\}$, respectively. Each set contains 4 subsets whose porosities are $\varepsilon \in \{0.70,\ 0.75, 0.80, 0.85\}$. Each of these subsets contains 5 statistically similar REVs. Thus, the total number of REVs generated is $3 \times 4 \times 5 = 60$.

Discrete MC analyses were conducted using all REVs to predict effective extinction coefficients. At least $5 \times 10^4$ rays were launched from random locations and random directions from fluid phase of each REV. The results can be seen in Figure 3.4.

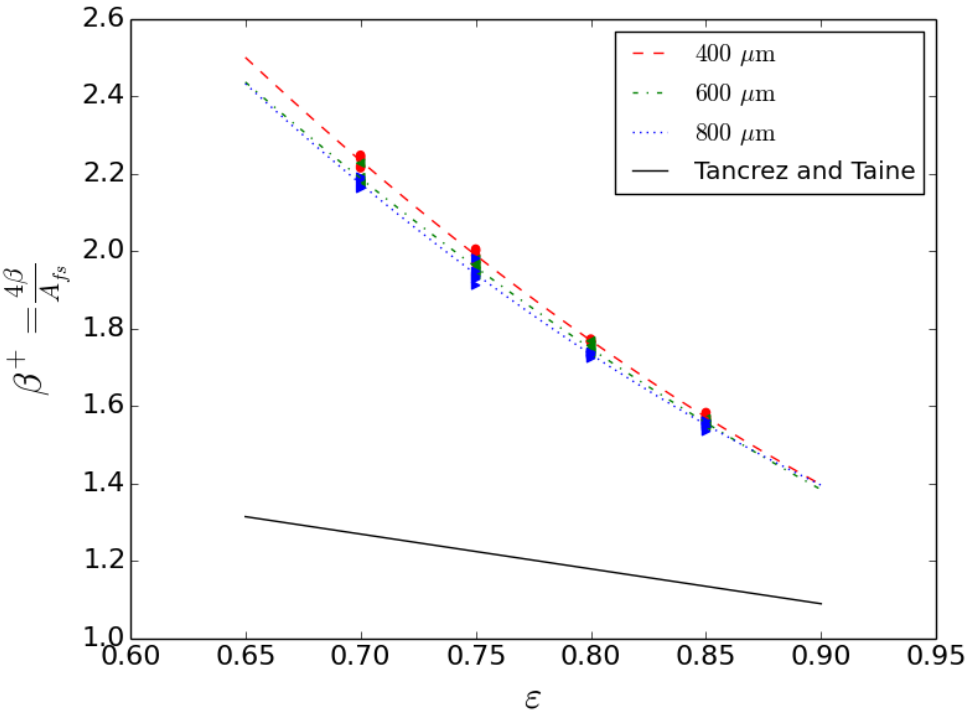


Figure 3.4 Non-dimensional extinction coefficient vs. porosity

Figure 3.4 shows the expected downward trend with increasing porosity. Note the extinction coefficient has been scaled using the internal surface area per unit volume, $A_{fs}$, for comparison with Ref. [6]. Simply stated, a larger void fraction will allow rays to travel further before attenuation, resulting in a smaller extinction coefficient. The data

also shows a weak, positive correlation with average pore diameter. The data has been fit to a second order polynomial of the form

$$\beta^{+} = a_2\varepsilon^2 + a_1\varepsilon + a_0, \tag{4.15}$$

where the coefficients pertaining to each average diameter are given in Table 3.1.

Table 3.1 Summary of the polynomial coefficients applicable to Eq. (4.15)

| $d$ (μm) | $a_0$ | $a_1$ | $a_2$ |
|---|---|---|---|
| 400 | 8.07 | -11.6 | 4.62 |
| 600 | 7.39 | -10.1 | 3.79 |
| 800 | 8.12 | -12.1 | 5.11 |

Tancrez and Taine [6] have also employed this method to identify the non-dimensional extinction coefficient for the case of dispersed radius overlapping transparent fluid spheres where $\varepsilon \in [0,1]$, and proposed correlation $\beta^{+} \approx 1 + 0.90(1-\varepsilon)$, which has been plotted in Figure 3.4. The geometric structures used in that study are similar to the present geometries, with one distinction: the sphere centers in [6] were randomly placed inside the domain, whereas the spheres in chapter 2 were packed together.

## 3.4 Conclusion

In the present work we have generated digital, statistically random REVs representing SVP carbon foams with differing mean pore diameters and porosities, and applied a statistical MC method to identify their effective extinction coefficients. It was found that the non-dimensional extinction coefficients were shown to have a strong, negative correlation with porosity, and a weak, positive correlation with mean pore diameter. The results have been satisfactorily fitted to a second order polynomial, which may be used to evaluate extinction coefficients in lieu of experimental data.

## 3.5 Acknowledgements

The authors would like to thank Alex Kalopsis, for his assistance in setting up and running the ANSYS CFX simulations.

## 3.6 References

[1] J. R. Howell, M. J. Hall and J. L. Ellzey. Combustion of hydrocarbon fuels within porous inert media. *Progress in Energy and Combustion Science 22(2),* pp. 121. 1996. Available: http://www.sciencedirect.com/science/article/pii/0360128596000019. DOI: http://dx.doi.org/10.1016/0360-1285(96)00001-9".

[2] A. J. Barra, G. Diepvens, J. L. Ellzey and M. R. Henneke. Numerical study of the effects of material properties on flame stabilization in a porous burner. *Combust. Flame 134(4),* pp. 369. 2003. Available: http://www.sciencedirect.com/science/article/pii/S0010218003001251. DOI: http://dx.doi.org/10.1016/S0010-2180(03)00125-1".

[3] A. J. Barra and J. L. Ellzey. Heat recirculation and heat transfer in porous burners. *Combust. Flame 137(1â€“2),* pp. 230. 2004. Available: http://www.sciencedirect.com/science/article/pii/S0010218004000537. DOI: http://dx.doi.org/10.1016/j.combustflame.2004.02.007".

[4] S. Singh and P. Dhiman. Thermal and thermohydraulic performance evaluation of a novel type double pass packed bed solar air heater under external recycle using an analytical and \RSM\ (response surface methodology) combined approach. *Energy 72(0),* pp. 344. 2014. Available: http://www.sciencedirect.com/science/article/pii/S0360544214006100. DOI: http://dx.doi.org/10.1016/j.energy.2014.05.044".

[5] P. Dhiman, N. S. Thakur and S. R. Chauhan. Thermal and thermohydraulic performance of counter and parallel flow packed bed solar air heaters. *Renewable Energy 46(0),* pp. 259-268. 2012. . DOI: http://dx.doi.org.proxy1.lib.uwo.ca/10.1016/j.renene.2012.03.032.

[6] M. Tancrez and J. Taine. Direct identification of absorption and scattering coefficients and phase function of a porous medium by a monte carlo technique. *Int. J. Heat Mass Transfer 47(2)*, pp. 373-383. 2004. Available: http://resolver.scholarsportal.info/resolve/00179310/v47i0002/373_dioaasmbamct. DOI: 10.1016/S0017-9310(03)00146-7.

[7] R. Coquard and D. Baillis. Radiative properties of dense fibrous medium containing fibers in the geometric limit. *Journal of Heat Transfer 128(10)*, pp. 1022-1030. 2006. . DOI: 10.1115/1.2345426.

[8] S. Haussener, P. Coray, W. Lipinski, P. Wyss and A. Steinfeld. Tomography-based heat and mass transfer characterization of reticulate porous ceramics for high-temperature processing. *J. Heat Transfer 132(2)*, pp. 023305. 2010. Available: http://dx.doi.org/10.1115/1.4000226. DOI: 10.1115/1.4000226.

[9] B. Zeghondy, E. Iacona and J. Taine. Determination of the anisotropic radiative properties of a porous material by radiative distribution function identification (RDFI). *Int. J. Heat Mass Transfer 49(17–18)*, pp. 2810-2819. 2006. . DOI: http://dx.doi.org.proxy1.lib.uwo.ca/10.1016/j.ijheatmasstransfer.2006.02.034.

[10] B. Zeghondy, E. Iacona and J. Taine. Experimental and RDFI calculated radiative properties of a mullite foam. *Int. J. Heat Mass Transfer 49(19–20)*, pp. 3702-3707. 2006. . DOI: http://dx.doi.org.proxy1.lib.uwo.ca/10.1016/j.ijheatmasstransfer.2006.02.036.

[11] R. Siegel and J. R. Howell. Thermal radiation heat transfer. *NASA STI/Recon Technical Report A 93*pp. 17522. 1992.

[12] M. F. Modest. *Radiative Heat Transfer* 2013.

[13] S. Whitaker. *The Method of Volume Averaging* 1999*13*.

[14] W. Lipiński, J. Petrasch and S. Haussener. Application of the spatial averaging theorem to radiative heat transfer in two-phase media. *Journal of Quantitative Spectroscopy and Radiative Transfer 111(1)*, pp. 253-258. 2010. Available:

http://resolver.scholarsportal.info/resolve/00224073/v111i0001/253_aotsatrhtitm. DOI: 10.1016/j.jqsrt.2009.08.001.

[15] J. Petrasch J., S. Haussener and W. Lipiński. Discrete vs. continuum-scale simulation of radiative transfer in semitransparent two-phase media. *Journal of Quantitative Spectroscopy and Radiative Transfer 112(9),* pp. 1450-1459. 2011. Available: http://resolver.scholarsportal.info/resolve/00224073/v112i0009/1450_dvcsortistm. DOI: 10.1016/j.jqsrt.2011.01.025.

[16] D. P. Anderson, P. G. Wapner and D. B. Curliss. Physical property characteristics of pitch materials. Presented at MRS Proceedings. 1992, .

[17] Dassault Systemes, "Solidworks Educational Version 2012-2013," .

[18] L. Betchen, A. G. Straatman and B. E. Thompson. A nonequilibrium finite-volume model for conjugate fluid/porous/solid domains. *Numerical Heat Transfer, Part A: Applications 49(6),* pp. 543-565. 2006. Available: http://resolver.scholarsportal.info/resolve/10407782/v49i0006/543_anfmfcfd. DOI: 10.1080/10407780500430967.

[19] R. Viskanta and R. J. Grosh. Effect of surface emissivity on heat transfer by simultaneous conduction and radiation. *Int. J. Heat Mass Transfer 5(8),* pp. 729-734. 1962.

[20] S. Mohsen Karimian and A. G. Straatman. A thermal periodic boundary condition for heating and cooling processes. *Int J Heat Fluid Flow 28(2),* pp. 329-339. 2007.

# Chapter 4

# 4 Conclusions and Future Work

The original objective of this thesis was to explore the viability of spherical-void-phase (SVP) carbon foam for use as a volumetric absorber. However, in conducting the requisite background research, it was found that there is little available data regarding the radiative properties of SVP carbon foam. Thus, the research effort was refocused on prediction of radiative properties. This could have been achieved through a series of experiments, however this author's particular skill set lent itself to computational work rather than experimental work. The method described by Tancrez and Taine [1] was found to be quite suitable, however a digital sample of the microstructure of interest is required for implementation. Several researchers have proposed idealized and random pore level models which have been useful in the study of hydraulic and thermal properties of SVP porous media, however each one of these models was analyzed and deemed unsatisfactory for radiative property determination; idealized models exhibited an uncharacteristic anisotropy in all directions, while the random generation methods available suffered from ad hoc pore interactions and a general lack of realism in their generation. Consequently, the effort was again refocused on devising a practical method for generating adequate digital samples of SVP porous media.

All in all, this thesis Although the motivation for the present work has been to assess the radiative properties of carbon foams, this author believes the more valuable outcome is the ability to quickly generate digital samples of SVP porous media which can be used to predict the bulk properties for any

## 4.1 Conclusions and Research Contributions

Chapter 2 documents the method developed for digital sample generation of SVP porous media. It has been achieved through use of Discrete Element Modeling (DEM), where the interaction between pores has been controlled through use of bubble-bubble contact law, and periodicity in all three principle directions has also been achieved. The resulting Computer-Aided-Design (CAD) files are, to the author's knowledge, the most accurate

digitally generated samples of carbon foam; they are visually similar to SEM images of real carbon foams, and they have been demonstrated to predict hydraulic and thermal properties with much more accuracy than the idealized unit-cube model. Upon validating the approach, the method was used to generate samples of carbon foam over a range of mean pore diameters and porosities, which were then used to determine hydraulic and thermal properties using Computational Fluid Dynamics (CFD) software. This illustrates a significant advantage of the fictitious digital models over physical samples: the dimensions of microstructural geometric features can be incrementally varied over desired ranges to explore *possible* effective properties, where financial costs and production capabilities can severely limit the number of microstructural variations which can be studied. Moreover, analyzing fictitious samples may inspire manufacturers to produce specific microstructures which predict desirable effective properties.

Chapter 3 describes the subsequent prediction of the extinction coefficient of SVP porous media for a range of mean pore diameters and porosities, which for the assumed case of negligible scattering, is equal to the absorption coefficient of the foam. The predicted non-dimensional extinction coefficient is significantly higher than the predictions from Tancrez & Taine [1], likely because the samples in that work contained randomly located spheres, where the samples in the present work were packed together. It was further concluded that, within the given ranges of mean pore diameter and porosities, the boundaries of SVP carbon foam samples may be treated as a black surfaces; i.e. nearly all incident radiation is assumed to be absorbed at the surface.

## 4.2 Future Work

In many fields of research, there appears to be an endless list of models to refine, assumptions to be validated or lifted, and new ideas to explore. The study of porous materials is no exception. This section contains an (incomplete) list for the areas of digital generation of porous materials and the prediction of their properties. The items are ordered from highest to lowest priority in accordance with their perceived value to the academic community.

The outstanding tasks in the field of digital generation of porous materials are:

- *Characterization of effective properties.* The closure models proposed by Whitaker and colleagues [5-7], and Quintard and colleagues [8, 9], have been successfully applied to study idealized geometries [10-14] to determine effective material properties. With the existing code infrastructure in place, generating a variety of random, digital domains can be done with relative ease. Note that while the work in this thesis has been focused on the negative volume of SVP porous media, only minor adjustments are needed to produce the solid matrix structure in CAD, which can be analyzed to determine effective thermal conductivities using various techniques described in the literature [2-4]. The models generated can also theoretically be used to characterize even more bulk transport quantities, such as mass transport, turbulent, and magnetic properties. If a researcher wishes to study other sphere based models, such as packed beds, only the contact law needs to be re-defined to suit the problem. If a little more effort is invested, the existing codes can be modified to characterize the interaction between other types of primitives, such as non-spherical particles, or fibres, or combinations thereof.
- *Development of Software tools to aid in digital domain generation*. However, in this thesis it has been shown, at least for the case of SVP carbon foam, that the accuracy of the predicted properties of the random model greatly exceeds that of its idealized counterpart, the unit-cube model. As was discovered during this research, the practical implementation of this method is not straight forward; it requires the orchestration software packages which do not readily interface. An estimated 6000 lines of computer code have been written between three programming languages to yield a semi-automated system spanning two operating systems and three software packages. Needless to say this is not ideal for researchers who want to avoid a lengthy setup process. This awkward implementation is seen as the primary barrier to researchers wishing to predict properties using digital generation techniques. The development of robust, general programming scripts to interface between these software packages will likely reduce the setup time, making random domain generation of porous samples more viable.

- *Modelling non-spherical bubbles.* At its heart, the present SVP generation technique is a crude model of the formation process occurring during the synthesis of real carbon foams. In order to obtain better representations of any porous medium, the analyst should look to the physical processes at play during its formation, and understand where those are misrepresented in the current models. In the case of SVP porous media, we have presently assumed the bubbles maintain their spherical shape. This is not generally true for high contact forces. In order to obtain more accurate digital models of SVP porous media, bubble deformation must be modeled. This will likely require a move from away from DEM, and towards CFD simulations to model bubble interaction dynamically as they are compressed with their neighbours.
- *Modelling pore window blockage.* When comparing images of the generated samples to photographs of real carbon foam, one of the observed differences is the shards protruding through the windows (review [fig.]). In the manufacturing process, when the carbon foam 'sets', the films between neighbouring bubbles remain, and the result is a closed-cell medium. These windows are opened by applying a large pressure across the foam causing the solid films to shatter. The shards are remnants of this process. These shards are thought to significantly increase the flow resistance through the foam, so it is desirable to quantify that resistance. This could be done through introduction of a two dimensional filter at the pore level, or using a random generation technique on the generated samples to attach shards around the circumference of pore windows.
- *Solar collector design.* While it has been established that the foam can safely be treated as a black body for the given range of mean pore diameters and porosities, it remains to be seen if the hydraulic and thermal properties will render it useful material for solar collectors. This will be investigated using a series of simulations using a conjugate porous/fluid/solid CFD code in conjunction with the properties determined in chapters 2 and 3.

## 4.3 References

[1] M. Tancrez and J. Taine. Direct identification of absorption and scattering coefficients and phase function of a porous medium by a monte carlo technique. *Int. J. Heat Mass Transfer 47(2),* pp. 373-383. 2004. Available: http://resolver.scholarsportal.info/resolve/00179310/v47i0002/373_dioaasmbamct. DOI: 10.1016/S0017-9310(03)00146-7.

[2] C. C. Chueh, A. Bertei, J. G. Pharoah and C. Nicolella. Effective conductivity in random porous media with convex and non-convex porosity. *Int. J. Heat Mass Transfer 71(0),* pp. 183-188. 2014. Available: http://www.sciencedirect.com/science/article/pii/S0017931013010855. DOI: http://dx.doi.org/10.1016/j.ijheatmasstransfer.2013.12.041.

[3] M. A. A. Mendes, S. Ray and D. Trimis. A simple and efficient method for the evaluation of effective thermal conductivity of open-cell foam-like structures. *Int. J. Heat Mass Transfer 66(0),* pp. 412-422. 2013. . DOI: http://dx.doi.org/10.1016/j.ijheatmasstransfer.2013.07.032.

[4] M. Wang and N. Pan. Modeling and prediction of the effective thermal conductivity of random open-cell porous foams. *Int. J. Heat Mass Transfer 51(5–6),* pp. 1325-1331. 2008. . DOI: http://dx.doi.org/10.1016/j.ijheatmasstransfer.2007.11.031.

[5] S. Whitaker. Improved constraints for the principle of local thermal equilibrium. *Ind Eng Chem Res 30(5),* pp. 983-997. 1991. Available: http://pubs.acs.org/doi/abs/10.1021/ie00053a022. DOI: 10.1021/ie00053a022.

[6] S. Whitaker. Simultaneous heat, mass, and momentum transfer in porous media: A theory of drying. *Advances in Heat Transfer 13*pp. 119-203. 1977.

[7] S. Whitaker. The forchheimer equation: A theoretical development. *Transp Porous Med 25(1),* pp. 27-61. 1996. Available: http://resolver.scholarsportal.info/resolve/01693913/v25i0001/27_tfeatd. DOI: 10.1007/BF00141261.

[8] M. Quintard, M. Kaviany and S. Whitaker. Two-medium treatment of heat transfer in porous media: Numerical results for effective properties. *Adv. Water Resour. 20(2–3),* pp. 77-94. 1997. . DOI: http://dx.doi.org/10.1016/S0309-1708(96)00024-3.

[9] M. Quintard. Modelling local non-equilibrium heat transfer in porous media. *Heat Transfer 1*pp. 279-286. 1998.

[10] Q. Yu, B. E. Thompson and A. G. Straatman. A unit cube-based model for heat transfer and fluid flow in porous carbon foam. *Journal of Heat Transfer 128(4),* pp. 352-360. 2006.

[11] P. Kumar, J. Hugo, F. Topin and J. Vicente. Influence of pore and strut shape on open cell metal foam bulk properties. *AIP Conference Proceedings 1453(1),* pp. 243-248. 2012. Available: http://search.ebscohost.com/login.aspx?direct=true&db=a9h&AN=75230839&site=ehost-live. DOI: 10.1063/1.4711183.

[12] P. Kumar, F. Topin and J. Vicente. Determination of effective thermal conductivity from geometrical properties: Application to open cell foams. *International Journal of Thermal Sciences 81(0),* pp. 13-28. 2014. . DOI: http://dx.doi.org.proxy1.lib.uwo.ca/10.1016/j.ijthermalsci.2014.02.005.

[13] K. Boomsma and D. Poulikakos. On the effective thermal conductivity of a three-dimensionally structured fluid-saturated metal foam. *Int. J. Heat Mass Transfer 44(4),* pp. 827-836. 2001. . DOI: http://dx.doi.org/10.1016/S0017-9310(00)00123-X.

[14] Z. Dai, K. Nawaz, Y. G. Park, J. Bock and A. M. Jacobi. Correcting and extending the Boomsma–Poulikakos effective thermal conductivity model for three-dimensional, fluid-saturated metal foams. *Int. Commun. Heat Mass Transfer 37(6),* pp. 575-580. 2010. . DOI: http://dx.doi.org/10.1016/j.icheatmasstransfer.2010.01.015.

Curriculum Vitae

| | |
|---|---|
| **Name:** | Nolan Dyck |
| **Post-secondary Education and Degrees:** | University of Waterloo<br>Waterloo, Ontario, Canada<br>2007-2012 B.A.Sc.<br><br>The University of Western Ontario<br>London, Ontario, Canada<br>2012-2014 M.E.Sc. |
| **Related Work Experience** | Teaching Assistant<br>The University of Western Ontario<br>2012-2014 |